Mechanism and dynamics of fatty acid photodecarboxylase

Damien Sorigué, Kyprianos Hadjidemetriou, S. Blangy, G. Gotthard, A. Bonvalet, Nicolas Coquelle, P. Samire, Alexey Aleksandrov, L. Antonucci, A. Benachir, et al.

Print page summary

Mechanism and dynamics of fatty acid photodecarboxylase

Authors: D. Sorigué, K. Hadjidemetriou, S. Blangy, G. Gotthard, A. Bonvalet, N. Coquelle, P. Samire, A. Aleksandrov, L. Antonucci, A. Benachir, S. Boutet, M. Byrdin, M. Cammarata, S. Carbajo, S. Cuiné, R. B. Doak, L. Foucar, A. Gorel, M. Grünbein, E. Hartmann, R. Hienerwadel, M. Hilpert, M. Kloos, T. J. Lane, B. Légeret, P. Legrand, Y. Li-Beisson, S. L. Y. Moulin, D. Nurizzo, G. Peltier, G. Schirò, R. L. Shoeman, M. Sliwa, X. Solinas, B. Zhuang**,** T. R.M. Barends, J.-P. Colletier, M. Joffre, A. Royant, C. Berthomieu*, M. Weik*, T. Domratcheva*, K. Brettel, M. H. Vos*, I. Schlichting*, P. Arnoux*, P. Müller*, F. Beisson*

Introduction: Photoenzymes are rare biocatalysts driven by absorption of a photon at each catalytic cycle; they inspire development of artificial photoenzymes with valuable activities. Fatty acid photodecarboxylase (FAP) is a natural photoenzyme that has potential applications in the bio-based production of hydrocarbons, yet its mechanism is far from fully understood.

Rationale: To elucidate the mechanism of FAP, we studied the wild type enzyme from *Chlorella variabilis* (*Cv*FAP) and variants with altered active site residues using a wealth of techniques, including static and time-resolved crystallography and spectroscopy as well as biochemical and computational approaches.

Results: A 1.8 Å-resolution *Cv*FAP x-ray crystal structure revealed a dense hydrogen bonding network positioning the fatty acid carboxyl group in the vicinity of the flavin adenine dinucleotide (FAD) cofactor. Structures solved from free electron laser and low-dose synchrotron x-ray crystal data further highlighted an unusual bent shape of the oxidized flavin chromophore and show that

the bending angle (14°) does not change upon photon absorption (step 1) and throughout the photocycle. Calculations show that bending substantially affects the energy levels of the flavin. Structural and spectroscopic analysis of wild-type (WT) and mutant proteins targeting two conserved active site residues, R451 and C432, demonstrated that both residues are crucial for proper positioning of the substrate and water molecules, and oxidation of the fatty acid carboxylate by ^{1}FAD* (~300 ps in WT FAP) to form $FAD^{\bullet-}$ (step 2). Time-resolved infrared spectroscopy demonstrated that decarboxylation occurs quasi-instantaneously upon this forward electron transfer, consistent with barrierless bond cleavage predicted by quantum chemistry calculations and with snapshots obtained by time-resolved crystallography. Transient absorption spectroscopy in H_2O and D_2O buffers indicated that back electron transfer from $FAD^{\bullet-}$ is coupled to and limited by transfer of an exchangeable proton or hydrogen atom (step 3). Unexpectedly, concomitant with $FAD^{\bullet-}$ reoxidation (to a red-shifted form FAD_{RS}) in 100 ns, the majority of the CO_2 product is converted, most likely into bicarbonate (as inferred from FTIR spectra of the cryo-trapped FAD_{RS} intermediate). Calculations indicate that this catalytic transformation involves an active-site water molecule. Cryo-Fourier transform infrared spectroscopy studies suggested that bicarbonate formation (step 4) is preceded by deprotonation of an arginine residue (step 3). At room temperature, the remaining CO_2 leaves the protein in 1.5 μs (step 4'). The observation of residual electron density close to C432 in electron density maps derived from time-resolved and cryo-crystallography data suggests that this residue may play a role in stabilizing CO_2 and/or bicarbonate. Three routes for alkane formation were identified by quantum chemistry calculations; the one shown in the figure is favored by the ensemble of experimental data.

Conclusion: We provide a detailed and comprehensive characterization of light-driven hydrocarbon formation by fatty acid photodecarboxylase, which uses a remarkably complex

mechanism including unique catalytic steps. We anticipate that our results will help expand the green chemistry toolkit.

Figure Caption:

Elucidation of the FAP photocycle by combining spectroscopic, biochemical, crystallographic and computational studies.

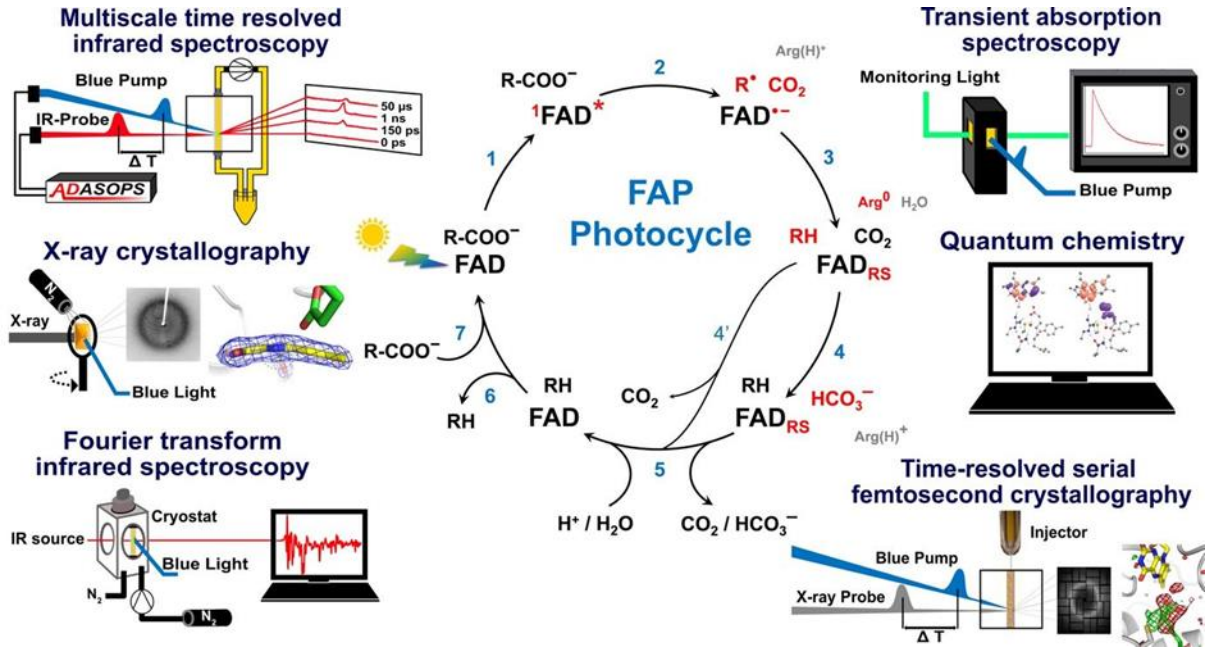

The list of author affiliations is available in the full article online. *Corresponding author. Email: frederic.beisson@cea.fr (F.B.); pavel.muller@i2bc.paris-saclay.fr (P.M.); pascal.arnoux@cea.fr (P.A.); Ilme.Schlichting@mpimf-heidelberg.mpg.de (I.S.); marten.vos@polytechnique.edu (M.H.V.); Tatjana.Domratcheva@mpimf-heidelberg.mpg.de (T.D.); martin.weik@ibs.fr (M.W.); catherine.berthomieu@cea.fr (C.B.);

Mechanism and dynamics of fatty acid photodecarboxylase

Authors: D. Sorigué[1], K. Hadjidemetriou[2], S. Blangy[1], G. Gotthard[3], A. Bonvalet[4], N. Coquelle[5], P. Samire[1,6], A. Aleksandrov[4], L. Antonucci[4], A. Benachir[4], S. Boutet[7], M. Byrdin[2], M. Cammarata[8], S. Carbajo[7], S. Cuiné[1], R. B. Doak[9], L. Foucar[9], A. Gorel[9], M. Grünbein[9], E. Hartmann[9], R. Hienerwadel[1], M. Hilpert[9], M. Kloos[9], T. J. Lane[7], B. Légeret[1], P. Legrand[10], Y. Li-Beisson[1], S. L. Y. Moulin[1], D. Nurizzo[3], G. Peltier[1], G. Schirò[2], R. L. Shoeman[9], M. Sliwa[11], X. Solinas[4], B. Zhuang[4,6], T. R. M. Barends[9], J.-P. Colletier[2], M. Joffre[4], A. Royant[2,3], C. Berthomieu[1,*], M. Weik[2,*], T. Domratcheva[9,12,*], K. Brettel[6], M. H. Vos[4,*], I. Schlichting[9,*], P. Arnoux[1,*], P. Müller[6,*], F. Beisson[1,*]

Affiliations:

[1]Aix-Marseille University, CEA, CNRS, Institute of Biosciences and Biotechnologies, BIAM Cadarache, 13108 Saint-Paul-lez-Durance, France.

[2]Univ. Grenoble Alpes, CEA, CNRS, Institut de Biologie Structurale, 38000 Grenoble, France.

[3]European Synchrotron Radiation Facility, 71 Avenue des Martyrs, CS 40220, 38043 Grenoble, France.

[4]LOB, CNRS, INSERM, Ecole Polytechnique, Institut Polytechnique de Paris, 91128, Palaiseau, France.

[5]Large-Scale Structures Group, Institut Laue Langevin, 71, avenue des Martyrs, 38042 Grenoble cedex 9, France.

[6]Université Paris-Saclay, CEA, CNRS, Institute for Integrative Biology of the Cell (I2BC), 91198 Gif-sur-Yvette, France.

[7]Linac Coherent Light Source (LCLS), SLAC National Accelerator Laboratory, 2575 Sand Hill Road, Menlo Park, CA 94025, USA.

[8]Department of Physics, UMR UR1-CNRS 6251, University of Rennes 1, F- Rennes, France: Marco Cammarata (Current address: ESRF)

[9]Max-Planck-Institut für medizinische Forschung, Jahnstrasse 29, 69120 Heidelberg, Germany.

[10]Synchrotron SOLEIL. L'Orme des Merisiers Saint-Aubin, BP 48, 91192 Gif-sur-Yvette, France.

[11]Univ. Lille, CNRS, UMR 8516, LASIR, Laboratoire de Spectrochimie Infrarouge et Raman, 59000 Lille, France.

[12]Department of Chemistry, Lomonosov Moscow State University, Moscow 119991, Russia.

*Correspondence to: frederic.beisson@cea.fr (F.B.), pavel.muller@i2bc.paris-saclay.fr (P.M.), pascal.arnoux@cea.fr (P.A.), Ilme.Schlichting@mpimf-heidelberg.mpg.de (I.S.), marten.vos@polytechnique.edu (M.H.V.), Tatjana.Domratcheva@mpimf-heidelberg.mpg.de (T.D.), martin.weik@ibs.fr (M.W.), catherine.berthomieu@cea.fr (C.B.)

Abstract: Fatty Acid Photodecarboxylase (FAP) is a photoenzyme with potential green chemistry applications. By combining static, time-resolved, and cryotrapping spectroscopy and crystallography as well as computation, we characterize *Chlorella variabilis* FAP reaction intermediates on time scales from sub-picoseconds to milliseconds. High-resolution crystal structures from synchrotron and free electron laser x-ray sources highlight an unusual bent shape of the oxidized flavin chromophore. We demonstrate that decarboxylation occurs directly upon reduction of the excited flavin by the fatty acid substrate. Along with flavin reoxidation by the alkyl radical intermediate, a major fraction of the cleaved CO_2 unexpectedly transforms in 100 ns, most likely into bicarbonate. This reaction is orders of magnitude faster than in solution. Two strictly conserved residues, R451 and C432, are essential for substrate stabilization and functional charge transfer.

One Sentence Summary: Snapshots of a photoenzyme reveal reaction intermediates during fatty acid decarboxylation.

The vast majority of enzymatic reactions in living cells are thermally activated, whereas reactions driven by light are much less common (*1*). Apart from photosynthetic reaction centers, three natural photoenzymes have been identified to date: DNA photolyases, which are involved in the repair of UV-damaged DNA (*2*), light-dependent protochlorophyllide oxidoreductase (LPOR) required for the maturation of chlorophyll (*3*) and the recently discovered fatty acid photodecarboxylase (FAP, EC 4.1.1.106), which converts fatty acids to hydrocarbons and CO_2 (*4*).

Photoenzymes require a photon for each turnover of a substrate molecule and offer the possibility to trigger and monitor catalytic steps and associated structural changes on very short time scales that are generally not accessible for thermally-activated enzymes (*5*). Thus, over the past 20 years, the photochemical mechanism has been studied in detail for DNA photolyases (*6*–*8*) and has started to be identified for LPOR (*9*–*13*). Due to its readily available substrate, FAP may become a model of choice to understand catalytic steps that occur in enzymology.

Light-driven enzymes are also interesting for practical applications. Increasing our understanding and the repertoire of photoenzymatic mechanisms may help in the design of catalysts performing new reactions (*14*, *15*) or in the development of new light-controlled proteins for optogenetics (*16*). FAP has potential biotechnological applications in green chemistry because hydrocarbons are important as cosmetics emollients, chemical synthons, solvents and fuels (*17*–*19*). FAP complements routes previously identified for bio-based synthesis of hydrocarbons (*20*) by providing a one-step light-driven pathway from fatty acids. Rational design approaches have recently allowed to improve the efficiency of FAP on high-value functionalized carboxylic acids (*21*) and on short-chain fatty acids in order to produce liquefied petroleum gas (*20*). Understanding the reaction mechanism of FAP in detail is thus of utmost importance, both from a fundamental-research and an application point of view.

FAP is an algae-specific enzyme from the glucose–methanol–choline (GMC) oxidoreductase family harboring a flavin adenine dinucleotide (FAD) cofactor. It allows the decarboxylation of C16-C18 free (non-esterified) fatty acids to the corresponding *n*-alka(e)nes (*4*). These hydrocarbon products are mostly located in chloroplast thylakoids but their exact role is still unknown (*22*, *23*). The initial spectroscopic characterization of FAP, based on monitoring the electronic state of the flavin following excitation by a laser flash, has led to a first model of the FAP photocycle (*4*). The cycle starts with the quenching of the singlet excited state by forward electron transfer (fET) from bound fatty acid R-CO_2^- in ~300 ps (with a quantum yield >80%), forming a flavin anion radical $FAD^{\bullet-}$ and a fatty acid radical R-$CO_2^{\bullet}$. The latter decarboxylates, yielding an alkyl radical $R^{\bullet}$ and CO_2. $FAD^{\bullet-}$ is re-oxidized in ~100 ns by back electron transfer (bET) which ultimately provides the electron for the reduction of $R^{\bullet}$ to the alkane RH. $FAD^{\bullet-}$ reoxidation results in a transiently red-shifted flavin state FAD_{RS} that reverts to the initial state in 4 ms.

Despite this insight, several open questions remained, such as: which structural features of the FAP active site promote substrate stabilization and favor the fET? Is decarboxylation instantaneous upon this fET step or is it slowed by an activation barrier? Does conversion of $R^{\bullet}$ to the alkane RH occur by bET from $FAD^{\bullet-}$ coupled to a proton transfer (PT/PCET) or by hydrogen atom transfer (HAT) from a nearby amino acid (*4*, *24*)? What is the origin of the proton or the hydrogen atom? Here, we report a high-resolution structure of FAP and characterize key steps along the FAP photocycle using a wealth of static and time-resolved crystallographic and spectroscopic techniques, as well as computational approaches. Our detailed characterization of FAP reveals unforeseen mechanistic complexity.

High resolution structure of *Cv*FAP

Crystals of FAP from *Chlorella variabilis* NC64A (*Cv*FAP), diffracting x-rays to high resolution and without the twinning fault reported earlier (*4*), were obtained upon removal of the N-terminal helix involved in crystal packing (residues 61 to 76) in native *Cv*FAP. The resulting structure, solved at 1.8 Å resolution (table S1) now provides a detailed view of the active site architecture (**Fig. 1A-D** and fig. S1). Although no substrate was added during protein purification and crystallization, two C18 fatty acids co-purified with FAP were clearly identified, one in the active site, the other on the surface of the protein. The latter is stabilized by hydrophobic interactions with nonpolar side chains (L427, Y419, I126, I416 and L420) as well as the aliphatic parts of R132 and R122. In the active site, the carboxyl group of the fatty acid is stabilized by hydrogen bonds with water molecules (Wat1 and Wat2) and the side chains of R451 and N575 (**Fig. 1D**). The fatty acid substrate is also stabilized on the dimethylbenzene side of FAD, in contrast to other GMC oxidoreductase enzymes that have their substrate stabilized near the N5 atom of FAD (fig. S2).

Conformation of oxidized FAD in *Cv*FAP

In the high-resolution dark-state structure of FAP obtained from synchrotron data '100 K dark', the isoalloxazine ring of the FAD cofactor was found to be bent, with the dihedral angle C4-N5-N10-C9 (butterfly bending angle) deviating by 17.4° from planarity (**Fig. 1E,** fig S2A)**.** Such bending is usually interpreted as caused by X-ray photoreduction converting supposedly planar oxidized flavin to the bent reduced form (*8*, *25*, *26*). For FAP however, *in crystallo* UV-Vis absorption microspectrophotometry (fig. S3), low dose crystallography, (fig. S4A and table S1)**,** Raman microspectrophotometry (fig. S4B,C) and molecular dynamics simulations (fig. S5A,B)

using a recent flavin force field (*27*) indicated that the FAD cofactor is bent in its oxidized form (supplementary text S1). To obtain a definite answer concerning the conformation of the oxidized FAD in FAP, we performed room temperature serial femtosecond crystallography (SFX) at an X-ray free-electron laser (XFEL; see below for details), which allows collecting essentially radiation damage-free diffraction data (*28*, *29*). Importantly, this SFX dark-state structure of FAP ('SFX dark'), solved at 2.0 Å resolution (table S2) features a FAD with a similar bending angle (14.3°) as observed in the synchrotron '100 K dark' and the 'RT dark low-dose' structures (**Fig. 1E** and figs. S4, S6, S7), supporting the notion that in FAP, the FAD cofactor is in a bent conformation in the oxidized state. To our knowledge, a butterfly bent conformation of the oxidized flavin has not been firmly established for any other flavoprotein. In fact, bent conformations were either not discussed or attributed to X-ray-induced flavin reduction. Future radiation-damage-free structures of oxidized flavoproteins should reveal whether the bending is a feature specific to FAP.

New insights into *Cv*FAP photocycle by time-resolved spectroscopy

Our previous single-shot fluorescence and transient absorption experiments in the presence of substrate, with 100 ps and 10 ns temporal resolution, respectively, showed a decay of the singlet excited flavin (^{1}FAD*) in ~300 ps and formation of FAD$^{\bullet-}$ within 10 ns (*4)*. Here we extend the fluorescence and visible absorption experiments to the ultrafast time scale with 100 fs-resolution pump-probe spectroscopy (**Fig. 2A,B** and fig. S8A) showing that no faster ^{1}FAD* decay phases occur, (only a ~2 ps thermal relaxation phase was observed in the fluorescence as in other flavoproteins (*30*)) and that, as predicted (*4)*, FAD$^{\bullet-}$ is formed concomitant with ^{1}FAD* decay (Fig S8B).

We investigated whether the carboxylate of the fatty acid is cleaved off concomitantly with electron transfer from the fatty acid to ^{1}FAD* (~300 ps), after this oxidation, or accompanying the bET from flavin (~100 ns). Light-induced FTIR difference spectroscopy performed at 298 K showed a CO_2 band at 2342 cm^{-1} (**Fig. 2C**) corresponding to CO_2 in solution (*31*). The kinetics of CO_2 formation in FAP were monitored by picosecond to microsecond time-resolved infrared spectroscopy (TR-IR) in a frequency range centered around 2350 cm^{-1} and Arbitrary Detuning ASynchronous OPtical Sampling (ADASOPS) (*32*, *33*). This experiment showed the appearance of a CO_2 absorption band centered at 2337.5 cm^{-1} with a time constant of ~270 ps (**Fig. 2C-E** and fig. S9). We conclude that decarboxylation is rate-limited by electron transfer from substrate to ^{1}FAD* occurring in ~300 ps. The initial CO_2 band frequency is ~5 cm^{-1} down-shifted with respect to that of $^{12}CO_2$ in aqueous solution, a finding we assign to the protein environment. Subsequently, the CO_2 signal diminishes ~4-fold with a time constant of 100 ns, without changing much in shape, followed by an upshift towards 2342 cm^{-1}, a process fitted with a time constant of ~1.5 µs. The latter process likely reflects migration of CO_2 towards the solvent. Importantly, the data indicate that the 100 ns process implies transformation of ~75% of the initially formed CO_2 within the protein into another molecule, possibly bicarbonate, concomitant with flavin reoxidation to the red-shifted form FAD_{RS} (see section on red-shift intermediate). This process was not foreseen in our previously proposed reaction scheme (*4*). Whereas our present data covering six orders of magnitude in time can reasonably well be described with these three exponential processes and a constant phase (**Fig. 2E**), it is possible that an additional phase of CO_2 release into the solvent occurs on a timescale exceeding 50 µs, the temporal window of our present experiments.

In order to determine whether any of the reaction steps are coupled to or directly reflect a proton transfer (PT) or a hydrogen atom transfer (HAT), we compared the kinetics of all steps

observable by continuous-probe time-resolved fluorescence or transient absorption spectroscopy in H_2O and D_2O buffers. The biphasic fluorescence signal showing the decay of ^{1}FAD* (due to quenching by ET from the substrate (300 ps phase; >80%) and to the intersystem-crossing to a non-reactive triplet state (~6.5 ns phase; <20%)) was not visibly affected by the isotope exchange (**Fig. 3A**), as expected for reactions that are not significantly coupled to movements of exchangeable hydrogen species (*e.g.*, back-ET from Q_A^- to $P680^+$ in photosystem II (*34*)). In contrast, the kinetics of $FAD^{\bullet-}$ reoxidation to FAD_{RS} observed by transient absorption spectroscopy at three characteristic wavelengths slowed down by a factor of ~2: from ~100 ns in H_2O to ~200 ns in D_2O (**Fig. 3B**), suggesting that this bET step is coupled to and limited by transfer of an exchangeable proton or hydrogen atom. Change of buffer pH in the interval between 7.5 and 9.1 had no effect on the kinetics of this step (fig. S10A), indicating that the proton or hydrogen atom donor involved in the reaction has a pK_a value above 9.1. The significantly lower kinetic isotope effect (*KIE*) of 1.2 reported by Heyes *et al.* (*24*) might be due to insufficient time-resolution of their experiment (see supplementary text S4).

The last step observable by transient absorption spectroscopy is the disappearance of the transient red shift of reoxidized FAD occurring in a few milliseconds. This process was previously (*4*) assigned to reprotonation of X^-, the conjugate base of XH, an unidentified proton donor to the alkyl radical. Kinetics of this process also slowed down when H_2O in the buffer was replaced by D_2O: from ~3 ms to ~10 ms (**Fig. 3C**). Consistent with this observation and the recent report of a pH increase (in an unbuffered solution) associated with this step (*24*), this process apparently reflects a proton transfer from bulk solvent. Again, change of buffer pH in the interval between 7.5 and 9.1 had no effect on the kinetics of this step (fig. S10B) and neither did the consumption of the native substrate (fig. S10C). Time-resolved spectroscopic findings are summarized in fig. S11.

Photodecarboxylation and characterization of the red-shifted intermediate at cryogenic temperatures

Our time-resolved spectroscopic results predict that a fraction of the CO_2 product is present in the active site in the red-shifted photoproduct intermediate. For a detailed characterization by static methods, we tried to stabilize this intermediate by cryotrapping. UV-visible absorption spectra of *Cv*FAP crystals and solutions exposed to increasing amounts of blue light at 100 K indeed revealed the gradual conversion into a red-shifted form similar to that previously observed at room temperature (Ref. (*4*) and fig. S12). These conditions were used to further characterize the red-shifted intermediate using light-induced FTIR difference spectroscopy. In order to identify IR modes of the substrate and products of the reaction, we replaced the native substrate by 1-^{12}C or 1-^{13}C palmitate. The identification of characteristic ^{13}C-sensitive IR bands of carboxylate in the FTIR difference spectra at 1541 cm^{-1} and 1391 cm^{-1} shows that the substrate initially was in the deprotonated form (**Fig. 4A** *i* and *ii*; details supporting all IR bands assignments mentioned below are given in supplementary text S2). A peak at 2340 cm^{-1} (**Fig. 4A** panel *v*) was assigned to formation of CO_2 from 1-^{12}Cpalmitate and at 2274 cm^{-1} from 1-^{13}C-palmitate. When comparing FTIR spectra recorded with FAP samples containing 1-^{12}C- and 1-^{13}C-palmitate, small bands were also observed at 1356 - 1335 cm^{-1} and 1312 cm^{-1} (**Fig. 4A** *iii*), which is indicative of the formation of trace amounts of ^{12}C and ^{13}C bicarbonate respectively. We repeated the FTIR experiments at 150 K. At this temperature, the CO_2 band was small (**Fig. 4A** panel *v*), while large positive bands at 1646 (1614) and 1352 (1318) cm^{-1} were detected that can be unambiguously assigned to IR modes of ^{12}C- (^{13}C-) bicarbonate (**Fig. 4A** *iv*). The FTIR data thus demonstrate the build-up of bicarbonate at 150 K and indicate that its formation at 100 K is limited by an energy barrier.

The structure derived from a *Cv*FAP crystal exposed to 470 nm light at 100 K ('100 K light') featured FAP trapped in a FAD_{RS} state, as shown by *in crystallo* microspectrophotometry (fig. S12). The difference electron density map between '100 K light' and '100 K dark' displays strong and significant peaks only around the substrate and FAD cofactor. These peaks can be fitted with a CO_2 molecule in addition to the alkyl chain stabilized in the active site (**Fig. 4B, C** and fig. S13A-C). The positive difference electron density along the aliphatic tail of the substrate (from C13 to C15) and the 8° rotation of the side chain of Y466 indicates a correlated motion in line with the strong electronic coupling observed by quantum chemistry between the substrate and Y466. In order to reflect the optimum pH of FAP in solution (pH 8.5; Ref. *(4)*) and to overcome thermal activation barriers, a FAP crystal was soaked at pH 8.5 and illuminated at 150 K ('150 K light'). Interestingly, after modeling alkane and a CO_2 molecule, the residual $F_o - F_c$ electron density map showed a positive density with a triangular shape close to C432, which we tentatively attribute to bicarbonate with 30% occupancy (**Fig. 4D** and fig. S14).

Time-resolved serial femtosecond crystallography of *Cv*FAP

We investigated the structural changes occurring in FAP after photoexcitation at room temperature by a time-resolved SFX (TR-SFX) experiment (*35*) using a pump-probe scheme. Time-resolved fluorescence spectroscopy on FAP microcrystals established that the kinetics of fET are the same as in solution (supplementary text S5, fig. S15). For TR-SFX at the Linac Coherent Light Source (LCLS), FAP microcrystals were photoexcited by picosecond 400 nm pump pulses and probed by femtosecond XFEL pulses after pump-probe delays of 20 ps, 900 ps, 300 ns, and 2 μs to cover time scales on which FAD reduction and $FAD^{\bullet-}$ reoxidation occur. The 'SFX dark' state structure

mentioned above, was determined from the data in the absence of a pump laser pulse. Structural changes after photoexcitation were visualized as positive and negative peaks in difference Fourier electron density maps calculated between the *light* and *dark* data sets ($F_{obs}^{light\_\Delta t} - F_{obs}^{dark}$; **Fig. 5A**) at 2.2 Å resolution. The most prominent difference electron density peaks at all four time points are at the active site, with the highest negative peak (–5.5 to –10.1 σ, depending on the time point) at the position of the carboxyl group of the substrate, showing that light-induced decarboxylation occurred (**Fig. 5A**). At 900 ps, decarboxylation has occurred to a considerable extent, in line with the 270 ps time constant determined by multi-scale time-resolved IR spectroscopy (**Fig. 2C-E**). At 300 ns and 2 μs, a strong negative peak is observed at Wat1 (–5.8, and –6.2 σ, respectively, **Fig. 5A**), but not on Wat2. We note the absence of positive difference electron density peaks associated with the photodissociated CO_2 in the vicinity of the substrate carboxyl group. A possible reason could be the small initial displacement of cleaved CO_2 relative to its position in the fatty acid, in line with the structure determined based on an illuminated cryo-cooled crystal '100 K light' (see fig. S13C for comparison). It is conceivable that the positive difference densities close to C432 in the 300 ns and 2 μs data sets (**Fig. 5A**) correspond to the feature(s) observed in the data obtained from cryo-cooled crystals illuminated at 150 K (**Fig. 5B** and **Fig. 4D**), tentatively assigned to a bicarbonate (fig. S14). In the SFX data, attempts to fit unambiguously this positive difference density with a bicarbonate, a CO_2 molecule or a mixture thereof remained unsatisfactory. The absence of significant difference electron density peaks at the FAD at all four time points suggests that the isoalloxazine ring does not undergo significant light-induced conformational changes.

Quantum chemistry study of *Cv*FAP

We performed quantum-chemistry calculations for the decarboxylation reaction in the active site of FAP, considering electronic states relevant for flavin photoexcitation, electron transfer, decarboxylation and alkane formation as well as effects of flavin bending (supplementary text S6). To perform the reaction pathway calculations, a large active site model (consisting of 272 atoms; fig. S16) was prepared using the coordinates of the high-resolution crystal structure of the dark state **(Fig. 1D).** Surprisingly, computations indicated multiple routes to form an alkane in the FAP active site as summarized in **Fig. 6**.

Common to all routes, photoexcitation triggers charge transfer (CT) from the substrate to the flavin. Interactions with two water molecules stabilize the anionic carboxylate substrate (1) (**Fig. 6A**). Removing these water molecules from the active site or rearranging Wat1 to form a hydrogen bond with flavin substantially decreases the energy of the CT state, i.e. of flavin radical anion and fatty acid radical (table S6). After Wat1 rearrangement, the CT energy is 15 kcal/mol lower than the excited-flavin energy (table S6). Concomitantly, electronic coupling between the flavin and substrate increases almost three fold reaching 47 meV (table S7), favoring transfer of an electron from the carboxylate. The formed carboxylic radical undergoes a barrierless decarboxylation (fig. S17) affording the alkyl radical (3). The energy of the alkyl radical intermediate is 52 kcal/mol above the dark state (1), which corresponds to more than 80% of the photon energy (**Fig. 6B**). CO_2 dissociation increases the distance separation in the radical pair, and accordingly the electronic coupling between the alkyl and flavin radicals is only 7 meV (table S7).

From the alkyl radical (3), the alkane product (6/6a) can be formed via several reaction pathways (I-III in **Fig. 6**). The chemical changes characterizing pathways I-III are summarized in **Fig. 6C**. Hydrogen atom transfer (HAT) from a nearby residue has been discussed previously *(4, 24)*. Our results indicate strong interactions with the Y466 phenolic side chain (electronic coupling

142 meV; table S7) that may facilitate migration of the alkyl radical towards Y466 and C432. The HAT reaction from C432 (pathway I in **Fig. 6**) proceeds via an energy barrier (9 kcal/mol; fig. S18) and leads to a Cys-radical state (4) with a 15 kcal/mol lower energy than that of the alkyl radical intermediate (3). Re-oxidation of the flavin by C432 (5) further reduces the energy by 3 kcal/mol (**Fig. 6B**). The resulting thiolate anion is stabilized by a hydrogen bond with positively charged R451, however proton transfer from R451 to C432 in (5) along the hydrogen bond yielding (5a) does not further reduce the energy (table S5). Hence, it is likely that C432 re-protonation proceeds by a different mechanism (see below).

Alternatively to the HAT reaction involving C432, a proton can be transferred from Wat2 which stabilizes the alkyl radical (3). The shift of the negative charge from the flavin to the alkane by bET coupled to proton transfer from Wat2 leads to a transient formation of a hydroxyl anion which either interacts with CO_2 forming bicarbonate (6a) directly (pathway III in **Fig. 6**), or it deprotonates R451 (5b) (pathway II in **Fig. 6**). The presence of CO_2 and water molecules in the active site, in particular Wat1, allows R451 re-protonation concomitant with bicarbonate formation (6), even after the alkane is formed, with a small activation energy (4 kcal/mol; fig. S19). The bicarbonate product derived from Wat1 (6) is 10 kcal/mol lower than the bicarbonate originating from Wat2 (6a), rendering pathway II more energetically favorable than pathway III (**Fig. 6B**). Energy lowering via bicarbonate formation may also further stabilize product (5) of the HAT reaction (pathway I): in the first step the thiolate C432 obtains a proton from R451 and/or Wat1 and in the second step, bicarbonate is formed from CO_2 and OH^- derived from Wat1 (6).

In view of the experimentally observed red-shifted re-oxidized flavin intermediate, we have compared the flavin excitation energy of the species resulting from the bET reaction and that of the initial dark state (**Fig. 6B**, table S8). Our computations suggest that the red shift can be

explained by formation of various species in which the initial negative charge of the deprotonated carboxylate (1) is either neutralized by formation of CO_2 and deprotonated R451 (5) or shifted away from the flavin by formation of the anionic bicarbonate (6) and (6a) (fig. S20). Additionally, a red shifted spectrum is caused by hydrogen-bonding interactions of Wat1 with flavin in (5a).

Consistent with the X-ray structures, all active-site models contain the butterfly bending conformation of the flavin isoalloxazine ring. Flavin bending persisted during geometry optimization of the FAP active site models (**Fig. 6A**) in contrast to the essentially planar optimized geometry of the oxidized and semi-reduced forms obtained in computations of flavins (*36*). The significant bending angle in the optimized FAP active-site structures is consistent with the notion that interactions with the protein modulate flavin bending (*37*). As previously discussed, this bending biases the energy levels of the flavin, favoring flavin reduction (*36*) and decreasing the excitation energy (table S9) with possible functional implications. In particular, bending diminishes the vertical electron affinity even more than the excited-flavin energy (fig. S21), and by this, preferentially reduces the CT-state energy which should facilitate fET. Thus, flavin bending explains the strongly red-shifted (20 nm) ground-state FAD absorption spectrum of FAP in the dark state compared to free FAD or most flavoproteins allowing photo-excitation and facile fET up to as far as 530 nm. Importantly, this is well into the so-called 'green gap' (between 500 and 600 nm) in the absorption spectra of chlorophylls that dominate the absorption of algae, thus enhancing the net light-harvesting capacities of FAP.

Role of conserved amino acids in the FAP active site

The active site of *Cv*FAP contains three residues (Y466, C432 and R451) that are strictly conserved and specific to FAPs compared to other GMC oxidoreductases (fig. S23). Y466 and C432 were previously considered as hydrogen atom donor to the alkyl radical $R^{\bullet}$ (followed by bET from $FAD^{\bullet-}$ to the tyrosyl or cysteinyl radical) or, alternatively, proton donor in a proton-coupled back-ET from $FAD^{\bullet-}$ to $R^{\bullet}$ (*4*, *24*). Our quantum chemical calculations additionally suggest R451 as a potential proton donor. In order to identify the proton donor experimentally, we performed FTIR; in particular, we analyzed possible contributions from deprotonated forms of these three residues in the cryo-trapped red-shifted intermediate. Light-induced FTIR difference spectra of *Cv*FAP recorded at 100K show only a shift of a *ν*(S-H) IR mode of cysteine, and no changes in D_2O compared to H_2O that could be assigned to tyrosine vibrations, which does not support deprotonation of either of the two residues under conditions where the flavin red shift was observed (**Fig. 4A** panel *vi* and supplementary text S2). However, a strong negative band was observed at 1606 cm^{-1} in FTIR difference spectra recorded in D_2O (**Fig. 4A** *vii*). In ^{15}N-labeled FAP samples, this band downshifted to 1597 cm^{-1} (**Fig. 4A,** *viii*). Both observations support assignment of the band to the guanidium IR mode of an arginine side-chain. Absence of a positive counterpart of this band after illumination is indicative of arginine deprotonation in the FAD_{RS} state at 100 K (supplementary text S2).

To gain further insight into the role of Y466, C432 and R451, we prepared Y466F, C432S, R451A and R451K mutants, performed activity measurements and extensive structural and spectroscopic characterization (UV-Vis absorption spectra are shown in fig. S24). Mutation of Y466 to phenylalanine affected the catalytic activity only slightly **(Fig. 7A)**, in line with a previous report (*24*). The kinetics of both fET to FAD and bET from $FAD^{\bullet-}$ do not differ much from WT *Cv*FAP (fig. S25C). Furthermore, almost identical FTIR difference spectra were obtained with WT

*Cv*FAP and the Y466F mutant (fig. S26A). Altogether, these results suggest that Y466 is not directly participating in any PT/HAT or ET step in the FAP photocycle, and its role is only briefly discussed in the supplementary text S4.

Mutation of C432 to serine (a much poorer proton and hydrogen atom donor) strongly affected the catalytic activity **(Fig. 7A)**, as reported earlier by Heyes and coworkers, who considered it indicative of HAT from C432 to the alkyl radical $R^{\bullet}$ in the WT protein (*24*). In contrast to these authors, we detected a low but significant catalytic activity (~ 10 % of WT) for the C432S mutant. Since impairment of the catalytic activity by a point mutation may result from structural changes rather than suppression of a direct function of the replaced residue, we examined the C432S mutant protein in more detail. The dark state crystal structure of C432S is highly similar to WT except for a new water molecule Wat3, interacting with S432 (2.7 Å) and the O1 oxygen atom of the fatty acid carboxylate (2.5 Å), which is rotated by ~ 42° (**Fig. 7D**). The distance of the carboxylate O2 to the flavin N5 increases from 4.0 Å in WT to 5.0 Å.

The time-resolved fluorescence signal of C432S resembles that of WT after the consumption of native substrate(s), however, the fluorescence decay is slightly (~10 %) accelerated (**Fig. 7B**), indicating that the signal reflects mostly intrinsic ^{1}FAD* decay (mostly due to intersystem crossing (ISC) *(4)*), with only a small contribution of competing fET to ^{1}FAD*. The intrinsic fET rate is about ten times slower than ^{1}FAD* decay in this mutant (see supplementary text S3). Transient absorption signals on the sub-ms time scale were hence dominated by the triplet (fig. S25F) and the formation of FAD_{RS} could not be resolved. There was, however, a small (~15% of WT) long-lived absorption change at 515 nm (where the transient flavin red-shift is most prominent in the WT). About two thirds of it decayed in a few milliseconds, *i.e.*, with similar kinetics as FAD_{RS} in WT (see upper inset of fig. S25F or Fig. 3D in *(24)*). With these indirect

indications of FAD_{RS} formation in C432S, we attempted to accumulate this species at a cryogenic temperature. Illumination of the sample at 200 K yielded a spectrum with similar shape (but lower amplitude) as the FAD_{RS} spectrum obtained with WT FAP (**Fig. 7C).**

When R451 was mutated to alanine, the enzymatic activity was completely abolished (**Fig. 7A**), no fET was observed (fig. S25B); in fact the structure shows that the fatty acid is oriented very differently than in the WT (see Fig. S26D and supplementary text S3 and S4 for details).

When R451 was replaced by lysine (which is also positively charged), the catalytic activity amounted to ~45 % of WT (**Fig. 7A**). The fluorescence decay (**Fig. 7B**) was distinctly faster (~4.5 ns) than in WT without substrate (~6.5 ns), consistent with fET occurring for ~30 % of the excited flavins. Reoxidation of $FAD^{\bullet-}$ and formation of FAD_{RS} was clearly resolved and found to be markedly faster (~30 ns; fig. S25D) than in WT (~100 ns; **Fig. 3B**, fig. S10A; supplementary text S3 and S4). The acceleration of the (proton-coupled) bET would be consistent with lysine being a better proton donor than arginine (solution pK_a of Lys is 10.7 *vs.* 12.1 for Arg).

To better understand how R451 affects the active site architecture, we determined the crystal structure of the R451K mutant in its dark-state at 100 K (**Fig. 7D** and fig. S26C). The R451K mutant structure differs significantly from WT: while a new water molecule mimics the NH_2 group of R451 and thereby retains the interaction with the O2 oxygen atom of the fatty acid carboxylate (2.5 Å), the interaction between K451 and the fatty acid O1 oxygen atom induces a ~54° rotation of the carboxylate and an increase by 0.6 Å of the distance of the fatty acid O2 to the flavin N5 compared to WT. This creates space for a new water molecule Wat3, akin to the situation in C432S, located between the fatty acid O1 atom (2.4 Å) and K451 (2.8 Å). The close distance of Wat3 and C432 induces a flip of the amino acid stretch T430 to G435, pushing C432 out of the

active site and bringing in an additional water molecule. These large structural changes may explain the very different FTIR spectra obtained with the R451K mutant compared to WT (fig. S26B).

Reaction cycle of FAP

In line with the strict conservation of C432 and R451 in FAP sequences, even conservative substitutions of these residues result in drastic reductions in catalytic activity, in both cases by strongly reducing fET. Unexpectedly, the R451K and C432S mutants share significant structural modifications with respect to the WT: the presence of a new water molecule, Wat3 close to the fatty acid carboxylate, a rotation of the carboxylate by ~50°, a significant elongation of the distance of the fatty acid carboxylate to the flavin N5, as well as small changes in Wat1 location. Quantum chemistry calculations show that in the C432S mutant the CT energy increases by 0.2 eV and the electronic coupling reduces five-fold, which is consistent with a much slower observed fET (see supplementary text 6.7 and fig. S22).

These mutants provide important insights into the molecular constraints affording FAP activity: the active site of the WT enzyme is arranged such as to optimize the configuration of the fatty acid carboxylate for fET. Each carboxylate oxygen atom interacts with catalytically important groups (O1: Wat1, O2: R451 and Wat2) while avoiding an inactivating bidentate interaction with R451.

Three possible routes towards alkane formation in FAP were suggested by quantum chemistry (**Fig. 6C**). Our experimental findings allow assessing the suggested pathways. Pathway I, involving a HAT mechanism to reduce the alkyl radical, as also suggested previously (*4*,*24*), is

chemically plausible. However, a number of experimental findings argue against it. First, the C432S mutant retains significant enzymatic activity, suggesting that C432 is not essential for catalysis. Second, in the FAD_{RS} state only a shift of a thiol S-H vibration is observed by FTIR but no cysteine deprotonation. Third, despite the fact that C432 is rotated out of the active site in the R451K mutant, this variant is quite active. While it is possible that C432 rotates back into the active site upon changes in the water structure following CO_2 cleavage, this would not explain the three-fold faster bET in R451K. Taken together, reaction pathway I (**Fig. 6C**) seems unlikely, although we cannot rule out that the C432S mutant uses a different mechanism than the WT enzyme. The observation of residual electron density consistent with bicarbonate close to C432 suggests that C432 may stabilize reaction products such as CO_2 and/or bicarbonate away from the original position of the substrate carboxylate.

The other two pathways proceed via PCET (**Fig. 6C**). Pathway III implies a catalytic role of Wat2 in bicarbonate formation. This mechanism is unlikely, as no changes were observed for Wat2 in the electron density maps derived by TR-SFX. In contrast, 300 ns after photoexcitation a significant loss of electron density of Wat1 was observed, supporting Pathway II. With the cleaved CO_2 present in the active site, as evidenced by cryocrystallography and IR spectroscopy, Wat2 can serve as a proton donor. The transiently deprotonated R451 activates Wat1, resulting in bicarbonate formation in less than 100 ns. This transformation of CO_2 to bicarbonate is orders of magnitude faster than in solution (tens of seconds (*38*)) indicating a strong catalytic effect.

R451's role as transient proton donor was *a priori* unexpected since proton transfers from and to arginine residues are rare (*39*, *40*) due to their relatively high pK_a values. In FAP, the strong basicity of OH^- formed from Wat2 by proton-coupled ET to the alkyl radical may allow proton transfer from R451. In addition to this catalytic function, R451 is crucial for the FAP active site

architecture by precisely positioning and orienting the fatty acid head group with respect to FAD and stabilizing the carboxylate in the catalytically active deprotonated form.

Figure 8 and its legend summarize our comprehensive understanding of the strikingly complex cycle. By combining results obtained by a multitude of experimental techniques and computations, we provide a detailed mechanistic description of the evolution of the reactant (fatty acid) to the products (alka(e)ne and CO_2) and the role of the protein moiety, involving a proton coupled electron transfer mechanism. We demonstrate partly unexpected structural and dynamic properties of FAP, including features that have not been observed in other flavoproteins and other enzymatic reactions in general. Understanding these catalytic features is an important step in incorporating FAP into the green chemistry toolkit.

Materials and Methods Summary

The FAP used in all experiments corresponds to residues 76-654 of the full-length *Cv*FAP (or single mutants thereof obtained by site-directed mutagenesis). WT *Cv*FAP and *Cv*FAP mutants expressed in *E. coli* and purified were studied by X-ray crystallography (static and TR-SFX), spectroscopy in solution (FTIR, TR-IR on ps to μs timescales, time-resolved fluorescence spectroscopy on ps to ns timescales, transient absorption spectroscopy on ns to ms timescales, and ultrafast visible absorption and fluorescence spectroscopy) and spectroscopy on single crystals (UV-Vis and Raman). Activity assays were based on quantification of hydrocarbons formed (by gas chromatography coupled to mass spectrometry) or CO_2 released (by membrane inlet mass spectrometry). Computational studies involved molecular dynamics simulations and quantum chemistry calculations on *Cv*FAP and multiple alignments of GMC oxidoreductases protein sequences. Detailed Materials and Methods are available in Supplementary Materials.

References and Notes

1. L. O. Björn, “Photoactive proteins” in *Photobiology: The Science of Light and Life* (Springer-Verlag, New York, ed. 3, 2015), pp. 139-150.

2. A. Sancar, Mechanisms of DNA Repair by Photolyase and Excision Nuclease (Nobel Lecture). *Angew. Chem. Int. Ed.* **55**, 8502–8527 (2016).

3. M. Gabruk, B. Mysliwa-Kurdziel, Light-Dependent Protochlorophyllide Oxidoreductase: Phylogeny, Regulation, and Catalytic Properties. *Biochemistry* **54**, 5255–5262 (2015).

4. D. Sorigué *et al.*, An algal photoenzyme converts fatty acids to hydrocarbons. *Science* **357**, 903–907 (2017).

5. D. Zhong, Ultrafast catalytic processes in enzymes. *Curr. Opin. Chem. Biol*. **11**, 174–181 (2007).

6. M. J. Maul *et al.*, Crystal Structure and Mechanism of a DNA (6-4) Photolyase. *Angew. Chem. Int. Ed.* **47**, 10076–10080 (2008).

7. P. Müller *et al.*, Discovery and functional analysis of a 4th electron-transferring tryptophan conserved exclusively in animal cryptochromes and (6-4) photolyases. *Chem. Commun. (Camb.)* **51**, 15502–15505 (2015).

8. A. Mees *et al.*, Crystal structure of a photolyase bound to a CPD-like DNA lesion after in situ repair. *Science* **306**, 1789–1793 (2004).

9. D. J. Heyes *et al.*, Ultrafast enzymatic reaction dynamics in protochlorophyllide oxidoreductase. *Nat. Struct. Mol. Biol*. **10**, 491–492 (2003).

10. N. S. Scrutton, M. L. Groot, D. J. Heyes, Excited state dynamics and catalytic mechanism of the light-driven enzyme protochlorophyllide oxidoreductase. *Phys. Chem. Chem. Phys*. **14**,

8818–8824 (2012).

11. D. J. Heyes *et al.*, Excited-state charge separation in the photochemical mechanism of the light-driven enzyme protochlorophyllide oxidoreductase. *Angew. Chem. Int. Ed.* **54**, 1512–1515 (2015).

12. S. Zhang *et al.*, Structural basis for enzymatic photocatalysis in chlorophyll biosynthesis. *Nature* **574**, 722–725 (2019).

13. C.-S. Dong *et al.*, Crystal structures of cyanobacterial light-dependent protochlorophyllide oxidoreductase. *Proc. Natl. Acad. Sci. U.S.A.* **117**, 8455–8461 (2020).

14. M. A. Emmanuel, N. R. Greenberg, D. G. Oblinsky, T. K. Hyster, Accessing non-natural reactivity by irradiating nicotinamide-dependent enzymes with light. *Nature* **540**, 414–417 (2016).

15. N. S. Scrutton, Enzymes make light work of hydrocarbon production. *Science* **357**, 872–873 (2017).

16. T. Courtney, A. Deiters, Recent advances in the optical control of protein function through genetic code expansion. *Curr. Opin. Chem. Biol*. **46**, 99–107 (2018).

17. S. Moulin *et al.*, Continuous photoproduction of hydrocarbon drop-in fuel by microbial cell factories. *Sci. Rep*. **9** (2019).

18. W. Zhang *et al.*, Hydrocarbon Synthesis via Photoenzymatic Decarboxylation of Carboxylic Acids. *J. Am. Chem. Soc.* **141**, 3116–3120 (2019).

19. M. Amer *et al.*, Low carbon strategies for sustainable bio-alkane gas production and renewable energy. *Energy Environ. Sci.* (2020).

20. N. A. Herman, W. Zhang, Enzymes for fatty acid-based hydrocarbon biosynthesis. *Curr. Opin. Chem. Biol*. **35**, 22–28 (2016).

21. J. Xu *et al.*, Light-Driven Kinetic Resolution of α-Functionalized Carboxylic Acids Enabled by an Engineered Fatty Acid Photodecarboxylase. *Angew. Chem. Int. Ed*. **58**, 8474–8478 (2019).

22. D. Sorigué *et al.*, Microalgae Synthesize Hydrocarbons from Long-Chain Fatty Acids via a Light-Dependent Pathway. *Plant Physiol.* **171**, 2393–2405 (2016).

23. S. Moulin *et al.*, "Fatty acid photodecarboxylase is an ancient photoenzyme responsible for hydrocarbon formation in the thylakoid membranes of algae". https://www.biorxiv.org/content/10.1101/2020.06.23.166330v1

24. D. J. Heyes *et al.*, On the photochemical mechanism of light-driven fatty acid photodecarboxylase. *ACS Catal.* (2020).

25. T. Senda, M. Senda, S. Kimura, T. Ishida, Redox control of protein conformation in flavoproteins. *Antioxid. Redox Signal.* **11**, 1741–1766 (2009).

26. A. K. Røhr, H.-P. Hersleth, K. K. Andersson, Tracking flavin conformations in protein crystal structures with Raman spectroscopy and QM/MM calculations. *Angew. Chem. Int. Ed.* **49**, 2324–2327 (2010).

27. A. Aleksandrov, A Molecular Mechanics Model for Flavins. *J. Comput. Chem*. **40**, 2834–2842 (2019).

28. H. N. Chapman *et al.*, Femtosecond X-ray protein nanocrystallography. *Nature* **470**, 73–77 (2011).

29. K. Hirata *et al.*, Determination of damage-free crystal structure of an X-ray-sensitive protein using an XFEL. *Nat. Methods* **11**, 734–736 (2014).

30. S. P. Laptenok *et al.*, Ultrafast real-time visualization of active site flexibility of flavoenzyme thymidylate synthase ThyX. *Proc. Natl. Acad. Sci. U.S.A.* **110**, 8924–8929 (2013).

31. L. H. Jones, E. McLaren, Infrared Absorption Spectra of SO2 and CO2 in Aqueous Solution. *J. Chem. Phys.* **28**, 995–995 (1958).

32. L. Antonucci *et al.*, Arbitrary-detuning asynchronous optical sampling with amplified laser systems. *Opt. Express* **23**, 27931–27940 (2015).

33. X. Solinas, L. Antonucci, A. Bonvalet, M. Joffre, Multiscale control and rapid scanning of time delays ranging from picosecond to millisecond. *Opt Express*. **25**, 17811–17819 (2017).

34. B. A. Diner, D. A. Force, D. W. Randall, R. D. Britt, Hydrogen Bonding, Solvent Exchange, and Coupled Proton and Electron Transfer in the Oxidation and Reduction of Redox-Active Tyrosine YZ in Mn-Depleted Core Complexes of Photosystem II. *Biochemistry* **37**, 17931–17943 (1998).

35. J.-P. Colletier, G. Schirò, M. Weik, in *X-ray Free Electron Lasers: A Revolution in Structural Biology*, S. Boutet, P. Fromme, M. S. Hunter, Eds. (Springer International Publishing, Cham, 2018), pp. 331–356.

36. J. D. Walsh, A.-F. Miller, Flavin reduction potential tuning by substitution and bending. *J. Mol. Struct. THEOCHEM*. **623**, 185–195 (2003).

37. B. W. Lennon, C. H. Williams, M. L. Ludwig, Crystal structure of reduced thioredoxin reductase from Escherichia coli: Structural flexibility in the isoalloxazine ring of the flavin adenine dinucleotide cofactor. *Protein Sci*. **8**, 2366–2379 (1999).

38. N. McCann *et al.*, Kinetics and Mechanism of Carbamate Formation from CO2(aq), Carbonate Species, and Monoethanolamine in Aqueous Solution. *J. Phys. Chem. A*. **113**, 5022–5029 (2009).

39. Y. Xiao *et al.*, Role of Arginine-82 in Fast Proton Release during the Bacteriorhodopsin Photocycle: A Time-Resolved FT-IR Study of Purple Membranes Containing 15N-Labeled

Arginine. *Biochemistry* **43**, 12809–12818 (2004).

40. P. J. Silva *et al.*, A tale of two acids: when arginine is a more appropriate acid than H3O+. *J. Phys. Chem. B.* **114**, 8994–9001 (2010).

41. A. Burlacot, F. Burlacot, Y. Li-Beisson, G. Peltier, Membrane Inlet Mass Spectrometry: A Powerful Tool for Algal Research. *Front. Plant Sci.* **11** (2020).

42. M. Roth *et al.*, FIP: a highly automated beamline for multiwavelength anomalous diffraction experiments. *Acta Crystallogr. D Biol. Crystallogr.* **58**, 805–814 (2002).

43. D. de Sanctis *et al.*, ID29: a high-intensity highly automated ESRF beamline for macromolecular crystallography experiments exploiting anomalous scattering. *J Synchrotron Rad*. **19**, 455–461 (2012).

44. D. von Stetten *et al.*, In crystallo optical spectroscopy (icOS) as a complementary tool on the macromolecular crystallography beamlines of the ESRF. *Acta Crystallogr. D Biol. Crystallogr.* **71**, 15–26 (2015).

45. A. Vagin, A. Teplyakov, Molecular replacement with MOLREP. *Acta Crystallogr. D Biol. Crystallogr.* **66**, 22–25 (2010).

46. G. N. Murshudov, A. A. Vagin, E. J. Dodson, Refinement of macromolecular structures by the maximum-likelihood method. *Acta Cryst. D Biol. Cristallogr.* **53**, 240–55 (1997).

47. P. Emsley, K. Cowtan, Coot: model-building tools for molecular graphics. *Acta Crystallogr. D Biol Crystallogr.* **60**, 2126–32 (2004).

48. J. McGeehan *et al.*, Colouring cryo-cooled crystals: online microspectrophotometry. *J. Synchrotron Rad.* **16**, 163–172 (2009).

49. D. von Stetten *et al.*, Online Raman spectroscopy for structural biology on beamline ID29 of the ESRF. *J. Struct. Biol.* **200**, 124–127 (2017).

50. O. B. Zeldin, M. Gerstel, E. F. Garman, RADDOSE-3D: time- and space-resolved modelling of dose in macromolecular crystallography. *J. Appl. Cryst.* **46**, 1225–1230 (2013).

51. D. von Stetten *et al.*, ID30A-3 (MASSIF-3) – a beamline for macromolecular crystallography at the ESRF with a small intense beam. *J Synchrotron Rad*. **27**, 844–851 (2020).

52. J. Sanchez-Weatherby *et al.*, Improving diffraction by humidity control: a novel device compatible with X-ray beamlines. *Acta Crystallogr. D Biol. Crystallogr.* **65**, 1237–1246 (2009).

53. A. Espagne, M. Byrdin, A. P. M. Eker, K. Brettel, Very Fast Product Release and Catalytic Turnover of DNA Photolyase. *ChemBioChem*. **10**, 1777–1780 (2009).

54. M. Byrdin *et al.*, Use of ruthenium dyes for subnanosecond detector fidelity testing in real time transient absorption. *Rev. Sci. Instrum.* **80**, 043102 (2009).

55. P. Müller *et al.*, ATP Binding Turns Plant Cryptochrome Into an Efficient Natural Photoswitch. *Sci. Rep.* **4**, 5175 (2014).

56. L. Nag *et al.*, Identification of the TyrOH•+ Radical Cation in the Flavoenzyme TrmFO. *J. Am. Chem. Soc.* **139**, 11500–11505 (2017).

57. S. P. Laptenok, P. Nuernberger, A. Lukacs, M. H. Vos, Subpicosecond Kerr-gate spectrofluorometry. *Methods Mol. Biol.* **1076**, 321–336 (2014).

58. M. A. Marangoni *et al.*, Narrow-bandwidth picosecond pulses by spectral compression of femtosecond pulses in second-order nonlinear crystals. *Opt Express*. **15**, 8884–8891 (2007).

59. J. Bredenbeck, J. Helbing, P. Hamm, Continuous scanning from picoseconds to microseconds in time resolved linear and nonlinear spectroscopy. *Rev. Sci. Instrum.* **75**, 4462–4466 (2004).

60. L. Antonucci, X. Solinas, A. Bonvalet, M. Joffre, Asynchronous optical sampling with arbitrary detuning between laser repetition rates. *Opt Express*. **20**, 17928–17937 (2012).

61. K. F. Lee, P. Nuernberger, A. Bonvalet, M. Joffre, Removing cross-phase modulation from midinfrared chirped-pulse upconversion spectra. *Opt Express*. **17**, 18738–18744 (2009).

62. J. J. Snellenburg *et al.*, Glotaran: A Java-Based Graphical User Interface for the R Package TIMP. *J. Stat. Soft.* **49** (2012).

63. D. Flot *et al.*, The ID23-2 structural biology microfocus beamline at the ESRF. *J. Synchrotron Rad*. **17**, 107–118 (2010).

64. U. Zander *et al.*, MeshAndCollect: an automated multi-crystal data-collection workflow for synchrotron macromolecular crystallography beamlines. *Acta Crystallogr. D. Biol. Cristallogr.* **71**, 2328–2343 (2015).

65. L. Lomb *et al.*, An anti-settling sample delivery instrument for serial femtosecond crystallography. *J. Appl Crystallogr*. **45**, 674–678 (2012).

66. U. Weierstall, J. C. Spence, R. B. Doak, Injector for scattering measurements on fully solvated biospecies. *Rev. Sci. Instrum*. **83**, 035108 (2012).

67. M. Liang *et al.*, The Coherent X-ray Imaging instrument at the Linac Coherent Light Source. *J. Synchrotron Rad*. **22**, 514–519 (2015).

68. M. L. Grünbein *et al.*, Illumination guidelines for ultrafast pump–probe experiments by serial femtosecond crystallography. *Nat. Methods* (2020).

69. G. Blaj *et al.*, X-ray detectors at the Linac Coherent Light Source. *J. Synchrotron Rad*. **22**, 577–583 (2015).

70. L. Foucar *et al.*, CASS-CFEL-ASG software suite. *Comput. Phys. Commun*. **183**, 2207–2213 (2012).

71. N. Coquelle *et al.*, Raster-scanning serial protein crystallography using micro- and nano-focused synchrotron beams. *Acta Crystallog. D. Biol. Cristallgr.* **71**, 1184–1196 (2015).

72. T. White, Processing serial crystallography data with CrystFEL: a step-by-step guide. *Acta Crystallogr. Section D*. **75** (2019).

73. Y. Gevorkov *et al.*, XGANDALF – extended gradient descent algorithm for lattice finding. *Acta crystallogr. A. Found Adv.* **75**, 694-704 (2019).

74. K. Nass *et al.*, Protein structure determination by single-wavelength anomalous diffraction phasing of X-ray free-electron laser data. *IUCrJ*. **3**, 180–91 (2016).

75. A. J. McCoy *et al.*, Phaser crystallographic software. *J. Appl. Crystallogr*. **40**, 658–674 (2007).

76. W. L. DeLano, The PyMOL Molecular Graphics System. *San Carlos, CA, USA: DeLano Scientific* (2002).

77. T. Ursby, D. Bourgeois, Improved Estimation of Structure-Factor Difference Amplitudes from Poorly Accurate Data. *Acta Crystallogr. A.* **53**, 564–575 (1997).

78. A. T. Brünger *et al.*, Crystallography & NMR System: A New Software Suite for Macromolecular Structure Determination. *Acta Crystallogr. D*. **54**, 905–921 (1998).

79. C. Wickstrand, R. Dods, A. Royant, R. Neutze, Bacteriorhodopsin: Would the real structural intermediates please stand up? *Biochim. Biophys. Acta* **1850**, 536–553 (2015).

80. K. Nass *et al.*, Structural dynamics in proteins induced by and probed with X-ray free-electron laser pulses. *Nat. Commun*. **11**, 1814 (2020).

81. T. J. Dolinsky, J. E. Nielsen, J. A. McCammon, N. A. Baker, PDB2PQR: an automated pipeline for the setup of Poisson–Boltzmann electrostatics calculations. *Nucleic Acids Res*. **32**, W665–W667 (2004).

82. M. H. M. Olsson, C. R. Søndergaard, M. Rostkowski, J. H. Jensen, PROPKA3: Consistent Treatment of Internal and Surface Residues in Empirical pKa Predictions. *J. Chem.*

Theory Comput. **7**, 525–537 (2011).

83. T. Darden, in *Computational biochemistry and biophysics* (Oren M. Becker, Alexander D. MacKerell Jr., Benoit Roux, Masakatsu Watanabe., 2001).

84. N. Foloppe, A. D. M. Jr, All-atom empirical force field for nucleic acids: I. Parameter optimization based on small molecule and condensed phase macromolecular target data. *J. Comput. Chem.* **21**, 86–104 (2000).

85. A. D. MacKerell *et al.*, All-atom empirical potential for molecular modeling and dynamics studies of proteins. *J. Phys. Chem. B.* **102**, 3586–3616 (1998).

86. W. L. Jorgensen *et al.*, Comparison of simple potential functions for simulating liquid water. *J. Chem. Phys.* **79**, 926–935 (1983).

87. E. Neria, S. Fischer, M. Karplus, Simulation of activation free energies in molecular systems. *J. Chem. Phys.* **105**, 1902–1921 (1996).

88. J. C. Phillips *et al.*, Scalable molecular dynamics with NAMD. *J. Comput. Chem.* **26**, 1781–1802 (2005).

89. Firefly program version 8.0, (available at http://classic.chem.msu.su/gran/gamess/index.html).

90. M. W. Schmidt *et al.*, General atomic and molecular electronic structure system. *J. Comput. Chem.* **14**, 1347–1363 (1993).

91. A. D. Becke, Density-functional thermochemistry. III. The role of exact exchange. *J. Chem. Phys.* **98**, 5648–5652 (1993).

92. C. Lee, W. Yang, R. Parr, Development of the Colle-Salvetti correlation-energy formula into a functional of the electron density. *Phys. Rev., B Condens. Matter.* **37**, 785–789 (1988).

93. S. Grimme, J. Antony, S. Ehrlich, H. Krieg, A consistent and accurate ab initio

parametrization of density functional dispersion correction (DFT-D) for the 94 elements H-Pu. *J. Chem. Phys*. **132**, 154104 (2010).

94. D. E. Woon, T. H. D. Jr, Gaussian basis sets for use in correlated molecular calculations. V. Core-valence basis sets for boron through neon. *J. Chem. Phys*. **103**, 4572 (1998).

95. A. A. Granovsky, Extended multi-configuration quasi-degenerate perturbation theory: the new approach to multi-state multi-reference perturbation theory. *J. Chem. Phys*. **134**, 214113 (2011).

96. H. A. Witek, Y.-K. Choe, J. P. Finley, K. Hirao, Intruder state avoidance multireference Møller-Plesset perturbation theory. *J. Comput. Chem*. **23**, 957–965 (2002).

97. V. Veryazov, P. Å. Malmqvist, B. O. Roos, How to select active space for multiconfigurational quantum chemistry? *Int. J. Quantum Chem*. **111**, 3329–3338 (2011).

98. A. Udvarhelyi, M. Olivucci, T. Domratcheva, Role of the Molecular Environment in Flavoprotein Color and Redox Tuning: QM Cluster versus QM/MM Modeling. *J. Chem. Theory Comput*. **11**, 3878–3894 (2015).

99. A. R. Moughal Shahi, T. Domratcheva, Challenges in Computing Electron-Transfer Energies of DNA Repair Using Hybrid QM/MM Models. *J. Chem. Theory Comput*. **9**, 4644–4652 (2013).

100. I. A. Solov'yov, T. Domratcheva, A. R. Moughal Shahi, K. Schulten, Decrypting cryptochrome: revealing the molecular identity of the photoactivation reaction. *J. Am. Chem. Soc.* **134**, 18046–18052 (2012).

101. T. Domratcheva, Neutral histidine and photoinduced electron transfer in DNA photolyases. *J. Am. Chem. Soc.* **133**, 18172–18182 (2011).

102. G. Nass Kovacs *et al.*, Three-dimensional view of ultrafast dynamics in photoexcited

bacteriorhodopsin. *Nat. Commun*. **10**, 3177 (2019).

103. R. J. Cave, M. D. Newton, Generalization of the Mulliken-Hush treatment for the calculation of electron transfer matrix elements. *Chem. Phys. Lett*. **249**, 15–19 (1996).

104. R. C. Edgar, MUSCLE: multiple sequence alignment with high accuracy and high throughput. *Nucleic Acids Res.* **32**, 1792–1797 (2004).

105. M. Gouy, S. Guindon, O. Gascuel, SeaView version 4: A multiplatform graphical user interface for sequence alignment and phylogenetic tree building. *Mol. Biol. Evol.* **27**, 221–224 (2010).

106. V. SYu, N. N. Kalnin, Quantitative IR spectrophotometry of peptide compounds in water (H2O) solutions. I. Spectral parameters of amino acid residue absorption bands. *Biopolymers* **30**, 1243–1257 (1990).

107. M. Falk, A. G. Miller, Infrared spectrum of carbon dioxide in aqueous solution. *Vib. Spectrosc*. **4**, 105–108 (1992).

108. A. R. Davis, B. G. Oliver, A vibrational-spectroscopic study of the species present in the CO2−H2O system. *J. Solution Chem*. **1**, 329–339 (1972).

109. R. Hienerwadel, C. Berthomieu, Bicarbonate binding to the non-heme iron of photosystem II investigated by Fourier transform infrared difference spectroscopy and 13C-labeled bicarbonate. *Biochemistry* **34**, 16288–16297 (1995).

110. H. Susi, D. M. Byler, W. V. Gerasimowicz, Vibrational analysis of amino acids: cysteine, serine, β-chloroalanine. *J. Mol. Struct*. **102**, 63–79 (1983).

111. H. Kandori *et al.*, Cysteine S−H as a Hydrogen-Bonding Probe in Proteins. *J. Am. Chem. Soc.* **120**, 5828–5829 (1998).

112. G. Dollinger *et al.*, Fourier transform infrared difference spectroscopy of

bacteriorhodopsin and its photoproducts regenerated with deuterated tyrosine. *Biochemistry* **25**, 6524–6533 (1986).

113. Y. N. Chirgadze, O. V. Fedorov, N. P. Trushina, Estimation of amino acid residue side-chain absorption in the infrared spectra of protein solutions in heavy water. *Biopolymers* **14**, 679–694 (1975).

114. M. S. Braiman, D. M. Briercheck, K. M. Kriger, Modeling vibrational spectra of amino acid side chains in proteins: Effects of protonation state, counterion, and solvent on arginine C-N stretch frequencies. *J. Phys. Chem. B.* **103**, 4744–4750 (1999).

115. P. F. Heelis, The photophysical and photochemical properties of flavins (isoalloxazines). *Chem. Soc. Rev.* **11**, 15–39 (1982).

116. A. Mozzarelli, G. L. Rossi, Protein function in the crystal. *Annu. Rev. Biophys. Biomol. Struct*. **25**, 343–365 (1996).

117. J. Woodhouse *et al.*, Photoswitching mechanism of a fluorescent protein revealed by time-resolved crystallography and transient absorption spectroscopy. *Nat. Commun*. **11**, 741 (2020).

118. M. R. Jackson *et al.*, A preference for edgewise interactions between aromatic rings and carboxylate anions: the biological relevance of anion-quadrupole interactions. *J. Phys. Chem. B.* **111**, 8242–8249 (2007).

1119. V. Kane Dickson, L. Pedi, S. B. Long, Structure and insights into the function of a Ca(2+)-activated Cl(-) channel. *Nature* **516**, 213–218 (2014).

120. E. Park, E. B. Campbell, R. MacKinnon, Structure of a CLC chloride ion channel by cryo-electron microscopy. *Nature* **541**, 500–505 (2017).

121. P. A. Karplus, K. Diederichs, Linking Crystallographic Model and Data Quality. *Science*

336, 1030–1033 (2012).

Acknowledgements

We thank Joyce Woodhouse for help with microcrystallization, Lucas Uriarte for help with spectroscopy experiments on crystals and Gabriela Nass Kovacs for preparation of injection conditions, Miroslaw Tarnawski for FAP stability measurements, Filipe Maia for helpful discussions and uploading the SFX data to CXIDB.ORG and Michel Philibert and the GRAP platform for custom manufacturing of scientific equipment. The IBS acknowledges integration into the Interdisciplinary Research Institute of Grenoble (IRIG, CEA) and financial support by the CEA, the CNRS and the UGA. The authors thank the staff of beamline ID-23-2 from the ESRF, Grenoble, France. The present work has benefited from the platform of Biophysics of I2BC supported by French Infrastructure for Integrated Structural Biology (FRISBI) ANR-10-INBS-05 and from the platform Heliobiotec (BIAM). **Funding:** ANR *SNAPsHOTs* to F.B., M.W., P.M., K.B., M.H.V., P.A., R.H., and C.B.; ANR Photoalkane to G.P.; ANR SignalBioRNJ to Y.L.-B.; ANR BioXFEL to M.W.; ERC Consolidator Grant STepLADDER (724362) to T.R.M.B., Chinese Scholarship Council fellowship to B.Z. MENESR – Univ. Grenoble Alpes fellowship to K.H. **Author contributions:** F.B., M.W., P.A., P.M., I.S., K.B., M.H.V., C.B., T.D. designed and organized the project.

J.-P.C., M.J., T.R.M.B., A.R. supervised parts of the project. D.S., S. Blangy, P.S., S. Cuiné., B.L. S.M., Y.L.-B., G.P., E.H. and F.B. analyzed FAP sequences, generated mutants, expressed and purified the FAPs and performed activity assays. D.S., S. Blangy, E.H. and P.A. produced crystals for synchrotron experiments, P.A., G.G., A.R., D.N., P.L., I.S. and D.S. acquired synchrotron diffraction data, G.G., P.A. and A.R. performed *in crystallo* optical spectroscopies and P.A, I.S.,

G.G., P.L. and A.R. interpreted data. D.S., R.H. and C.B. built the setup for cryogenic light-induced FTIR difference spectroscopy, acquired and analyzed the data. A. Bonvalet, A. Benachir, D.S. optimized and performed multi-scale TR-IR experiments, L.A., X.S, A. Bonvalet, M.J. conceived and developed multi-scale TR-IR spectroscopy and adapted for FAP experiments, A. Bonvalet., L.A., M.J., M.H.V. analyzed TR-IR data. M.H.V. performed and analyzed femtosecond pump-probe absorption and fluorescence spectroscopy. B.Z., M.H.V. performed and analyzed picosecond-pump power dependence spectroscopy. A.A. performed molecular dynamics simulations. D.S., S. Blangy and K.H. produced microcrystals for SFX and K.H., J.-P.C. and M.W tested their diffraction quality at the ESRF. M.S., K.H. and D.S. carried out time-resolved emission and absorption spectroscopy on microcrystals. T.RMB, M.C., S. Boutet, J.-P.C., N.C., R.B.D., L.F., A.G., M.L.G., K.H., M.H., M.K., T.J.L., G.S., I.S., R.L.S., M.W. carried out SFX experiments. R.L.S., R.B.D., M.L.G., and M.K. performed sample injection. S.Carbajo, G.S. and M.C. carried out laser work at the LCLS. S. Boutet and T.J.L. prepared and performed SFX data collection. L.F., M.H., N.C., J.P.C. and T.R.M.B. performed online SFX data analysis. K.H., N.C., J.-P.C., A.G., T.R.M.B. carried out offline SFX data processing. K.H., J.-P.C., N.C., M.W., T.R.M.B., I.S. analysed SFX data. M.B., K.B. and P.M. built the setups for ps-ns time-resolved fluorescence and ns-ms transient absorption spectroscopy. D.S., P.S., B.Z., P.M. and K.B. performed the measurements. P.M. and K.B. analyzed the data. T.D. performed quantum chemistry calculations and provided mechanistic insight. F.B., P.M., K.B., M.H.V., I.S., P.A., T.D., M.W., C.B., D.S. wrote the paper. The paper was discussed with all authors. **Competing interests:** The authors declare no competing interests. **Data and materials availability**: All data are available in the manuscript, the supplementary materials, or at publicly accessible repositories. Atomic coordinates of protein structures have been deposited in the Protein Data Bank under accession no.

6YRU, 6YRV, 6YRX, 6YRZ, 6YS1, 6YS2, 6ZH7, 7AV4. SFX diffraction images of FAP microcrystals have been deposited in the Coherent X-ray Imaging Data Bank website (CXIDB) with accession ID 177 (http://cxidb.org/id-177.html).

Supplementary Materials:

Materials and Methods

Supplementary text S1-S6

Figures S1-S31

Tables S1-S11

References (41-122)

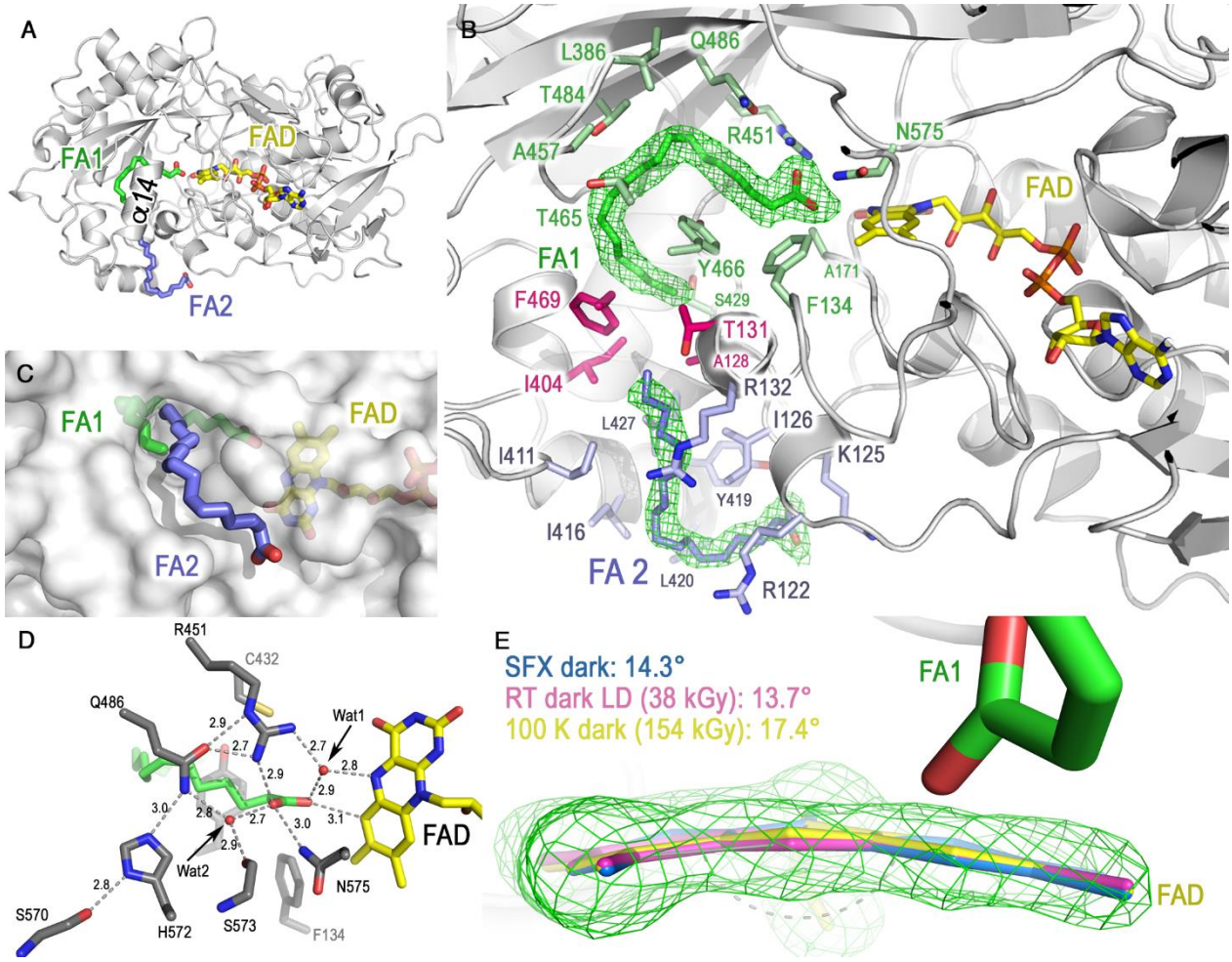
A
FA1
FAD
α14
FA2
B
L386
Q486
T484
A457
R451
N575
FAD
T465
FA1
Y466
A171
F469
S429
F134
T131
A128
I404
R132
L427
I126
I411
K125
Y419
I416
FA 2
L420
R122
C
FA1
FAD
FA2
D
R451
C432
Q486
Wat1
FAD
Wat2
N575
S570
H572
S573
F134
E
SFX dark: 14.3°
RT dark LD (38 kGy): 13.7°
100 K dark (154 kGy): 17.4°
FA1
FAD

Fig. 1. High resolution crystal structures of *Cv*FAP. (**A**) Structure of *Chlorella variabilis* FAP (*Cv*FAP) determined from synchrotron data at 100 K ('100 K dark'), including the FAD cofactor and two C18 fatty acid substrates (FA1 and FA2). (**B**) Binding of the two substrate molecules. The 'omit' electron density map (5.0 σ contour level) is shown as a green mesh, and amino acid side chains in a radius of 4 Å around the binding site are shown as sticks (green: active site, blue: secondary binding site, purple: between sites. (**C**) Position of the peripheral substrate (FA2); partly obstructing the channel leading to the active site tunnel. (**D**) Close-up view of the catalytic site, showing the water molecules Wat1 and Wat2 and the interactions with FAD (yellow sticks) and the substrate in the active site FA1 (green sticks). Distances are indicated in Ångstrom. The shortest distance between the substrate and the FAD cofactor (carboxylate O1-isoalloxazine C6) is 3.1 Å. The tail of the peripheral substrate points towards the entrance of a tunnel leading to the active site that is lined by A128, T131, I404 and F469. (**E**) Superposition of the FAD isoalloxazine rings from the SFX dark structure (blue; molecule A), and the synchrotron structures (pink: 'RT dark low-dose', yellow: '100 K dark'). The SFX $F_{obs} - F_{calc}$ omit map at 3 σ (green) is overlaid, and the FAD bending angles are indicated.

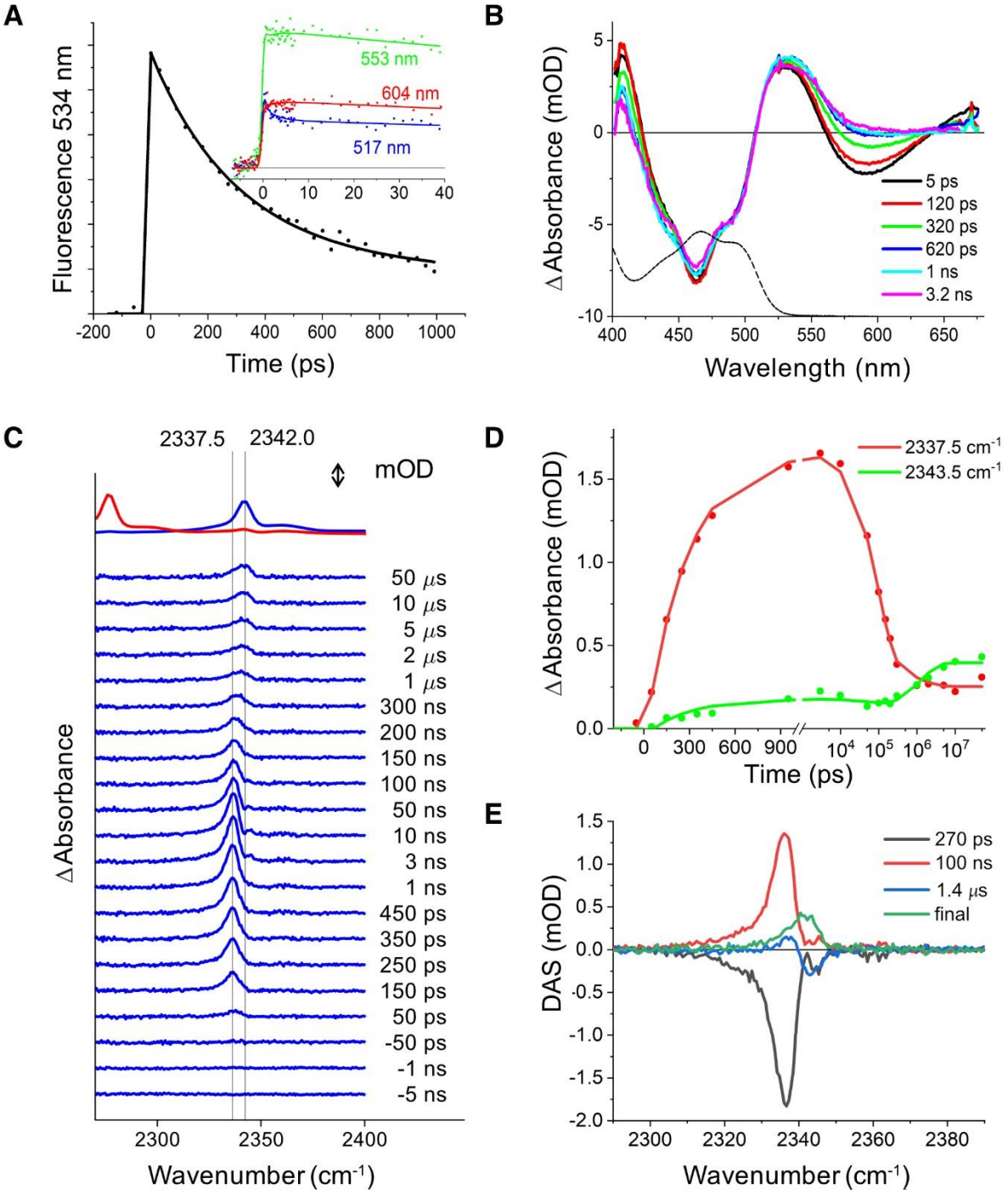
A
Fluorescence 534 nm
553 nm
604 nm
517 nm
Time (ps)
B
ΔAbsorbance (mOD)
5 ps
120 ps
320 ps
620 ps
1 ns
3.2 ns
Wavelength (nm)
C
2337.5
2342.0
mOD
ΔAbsorbance
50 μs
10 μs
5 μs
2 μs
1 μs
300 ns
200 ns
150 ns
100 ns
50 ns
10 ns
3 ns
1 ns
450 ps
350 ps
250 ps
150 ps
50 ps
-50 ps
-1 ns
-5 ns
Wavenumber (cm-1)
D
2337.5 cm-1
2343.5 cm-1
ΔAbsorbance (mOD)
Time (ps)
E
270 ps
100 ns
1.4 μs
final
DAS (mOD)
Wavenumber (cm-1)

Fig. 2. Time-resolved infrared and UV-visible spectroscopies of *Cv*FAP. (A) Fluorescence kinetics reflecting ^{1}FAD* decay. The solid line is a fit with time constants of 300 ps (85%) and 5 ns (the latter time constant was imposed according to (Ref. (*4*)). The *inset* shows an additional ~2 ps wavelength-dependent phase reflecting redshifting of the fluorescence spectrum due to excited state relaxation. **(B)** Transient visible absorption spectra at different delay times in the same time domain. The negative absorption features reflect bleaching of the FAD_{OX} resting state (<525 nm, the black dashed line is the ground state absorption spectrum) and stimulated emission (550 - 650 nm). Full transient fluorescence spectra and global analysis of the transient absorption spectra are shown in fig. S8. (**C**) Transient infrared spectra in the CO_2 spectral region on the picosecond-microsecond time scale. The vertical lines are guides for the eye and correspond to the maximum of released CO_2 in the protein and to the known maximum for CO_2 in aqueous solution, 2342 cm^{-1} (*31*). The upper traces correspond to independent *steady-state* 298 K light-induced FTIR difference spectra with ^{12}C-palmitate and 1-^{13}C-palmitate substrates (black trace and red trace respectively). (**D**) Kinetics at frequencies close to the initial and final maxima of released CO_2. The lines are the result of a global fit. The timescale is linear up to 1 ns and logarithmic thereafter. (**E**) Decay Associated Spectra (DAS) corresponding to a global fit of the data with three exponential phases (time constants of the fit are indicated) and a constant phase.

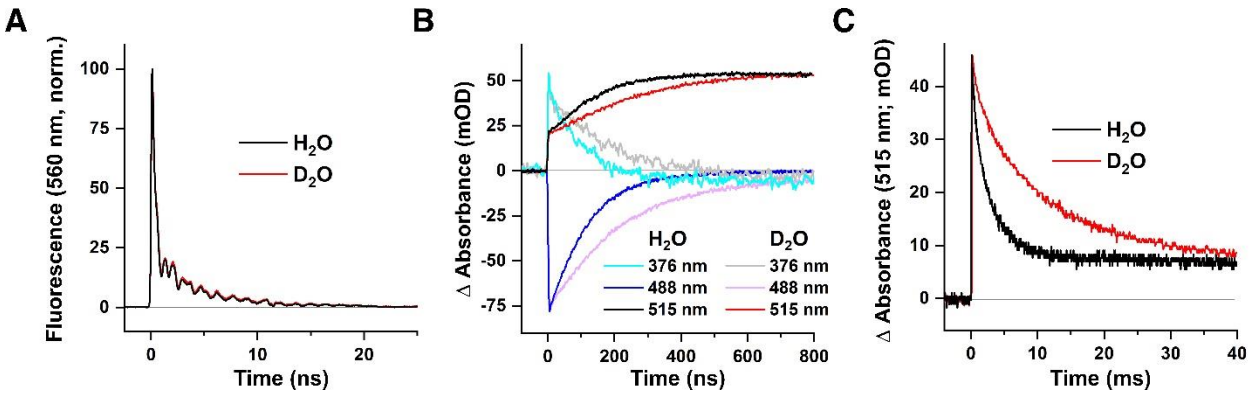

Fig. 3. Effects of H_2O/D_2O exchange on time-resolved fluorescence and UV-visible spectroscopy of *Cv*FAP. (**A**) Normalized signals of time-resolved fluorescence of ^{1}FAD* at 560 nm in H_2O and D_2O buffers. (**B**) Effect of H_2O to D_2O exchange on the kinetics of $FAD^{\bullet-}$ reoxidation to FAD_{RS} followed by transient absorption spectroscopy at selected wavelengths on a sub-microsecond timescale. (**C**) Effect of H_2O to D_2O buffer exchange on the decay of FAD_{RS} measured at 515 nm on the millisecond timescale.

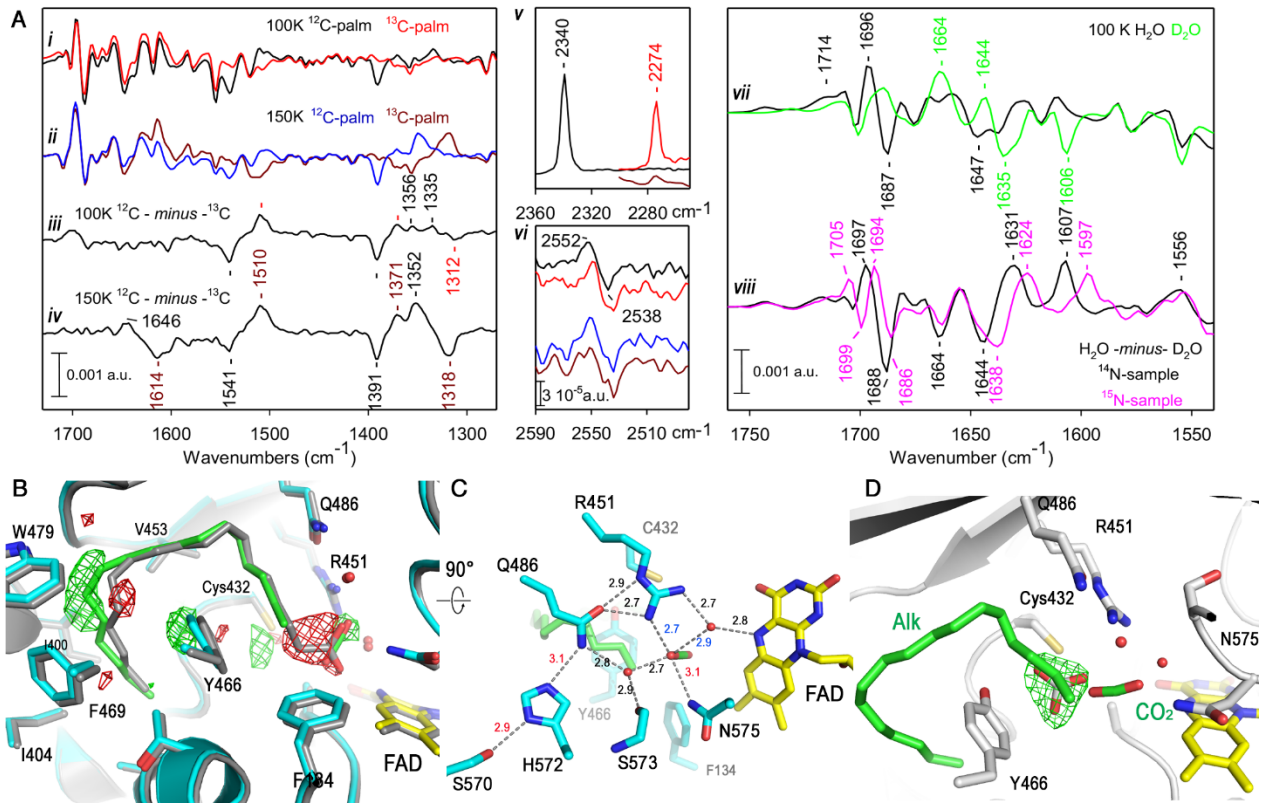
A
i
100K 12C-palm 13C-palm
ii
150K 12C-palm 13C-palm
iii
100K 12C - minus - 13C
iv
150K 12C - minus - 13C
0.001 a.u.
1700 1600 1500 1400 1300
Wavenumbers (cm-1)
v
2340
2274
2360 2320 2280 cm-1
vi
2552
2538
3 10-5 a.u.
2590 2550 2510 cm-1
vii
100 K H2O D2O
viii
H2O -minus- D2O
14N-sample
15N-sample
0.001 a.u.
1750 1700 1650 1600 1550
Wavenumber (cm-1)
B
W479
V453
Q486
R451
Cys432
I400
Y466
F469
I404
F134
FAD
90°
C
R451
C432
Q486
N575
FAD
Y466
H572
S573
S570
F134
D
Q486
R451
Cys432
Alk
N575
CO2
Y466

Fig. 4. Characterization of the *Cv*FAP red-shifted intermediate at cryogenic temperatures (**A**) Light-induced FTIR difference spectra recorded from FAP solutions *i*) and *ii*) and corresponding « ^{12}C- minus - ^{13}C » difference spectra iii) and iv). The 2360 - 2260 cm^{-1} and 2590 - 2490 cm^{-1} regions of the spectra in *i*) and *ii*) are shown in panels *v*) and *vi*). For the spectrum in black, the FTIR spectrometer was continuously purged with N_2 to avoid contamination by gaseous CO_2 that might originate from a dry air purge. This was not the case for spectra recorded from FAP samples with 1-^{13}C-palmitate; these were cut off above 2300 cm^{-1} to avoid bands from gaseous CO_2; vii) overlay of the spectra recorded at 100 K from FAP with ^{12}C-palmitate in H_2O (black) and in D_2O (green); *viii*) « H_2O – minus – D_2O » difference spectra calculated for ^{14}N and ^{15}N-labelled FAP samples. (**B**) Experimental difference density map ($F_{light} - F_{dark}$, 100 K data) contoured at +/– 4σ around the active site substrate, superimposed on the refined structures of the dark state (gray) and the red-shifted form (cyan, with FAD in yellow and alkane/CO_2 in green). The cleavage of the C1-C2 bond is clearly visible. (**C**) Details of the active site of FAP_{RS} formed upon illumination (UV-Vis spectra in fig. S12). All distances shorter than 3.2 Å are labeled, except the fatty acid O1 – FAD C6 distance, which increases from 3.1 Å in the dark to 3.6 Å upon illumination. (**D**) $F_o - F_c$ electron density omit map (3.5 σ) derived from crystals kept at 150 K and pH 8.5, showing positive difference electron density next to C432, consistent with a bicarbonate. Its potential interactions with the environment are shown in fig. S14. Uncleaved fatty acid (~30% occupancy) is omitted for clarity.

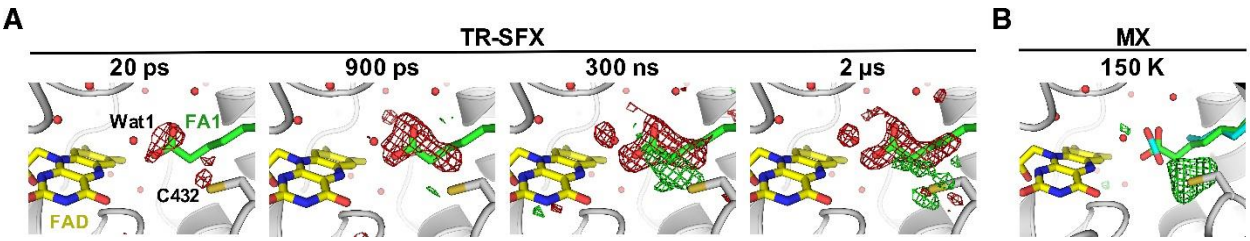

Fig. 5. Time-dependent changes in the *Cv*FAP active site followed by TR-SFX.

(**A**)Locally averaged q-weighted difference Fourier maps calculated between the SFX light and dark data sets ($F_{obs}^{light\_\Delta t} - F_{obs}^{dark}$; with Δt = 20 ps, 900 ps, 300 ns, 2 µs). The 2.2 Å resolution maps are shown at +4 σ (green) and -4 σ (red). The SFX dark state model of molecule B is overlaid, with FAD in yellow, fatty acid in green, and the protein in grey. The q-weighted difference maps for molecules A and B, *i.e.*, without local averaging, are shown in fig. S31. (**B**) $F_{obs} - F_{calc}$ electron density (contoured at 3.5 σ) of **Fig. 3E**, shown in a different orientation, which features unmodeled positive electron density next to C432 that is reminiscent of a bicarbonate (Fig. 4D, fig. S14, see text), in a location similar to where positive difference density is present in the time-resolved maps at 300 ns and 2 µs.

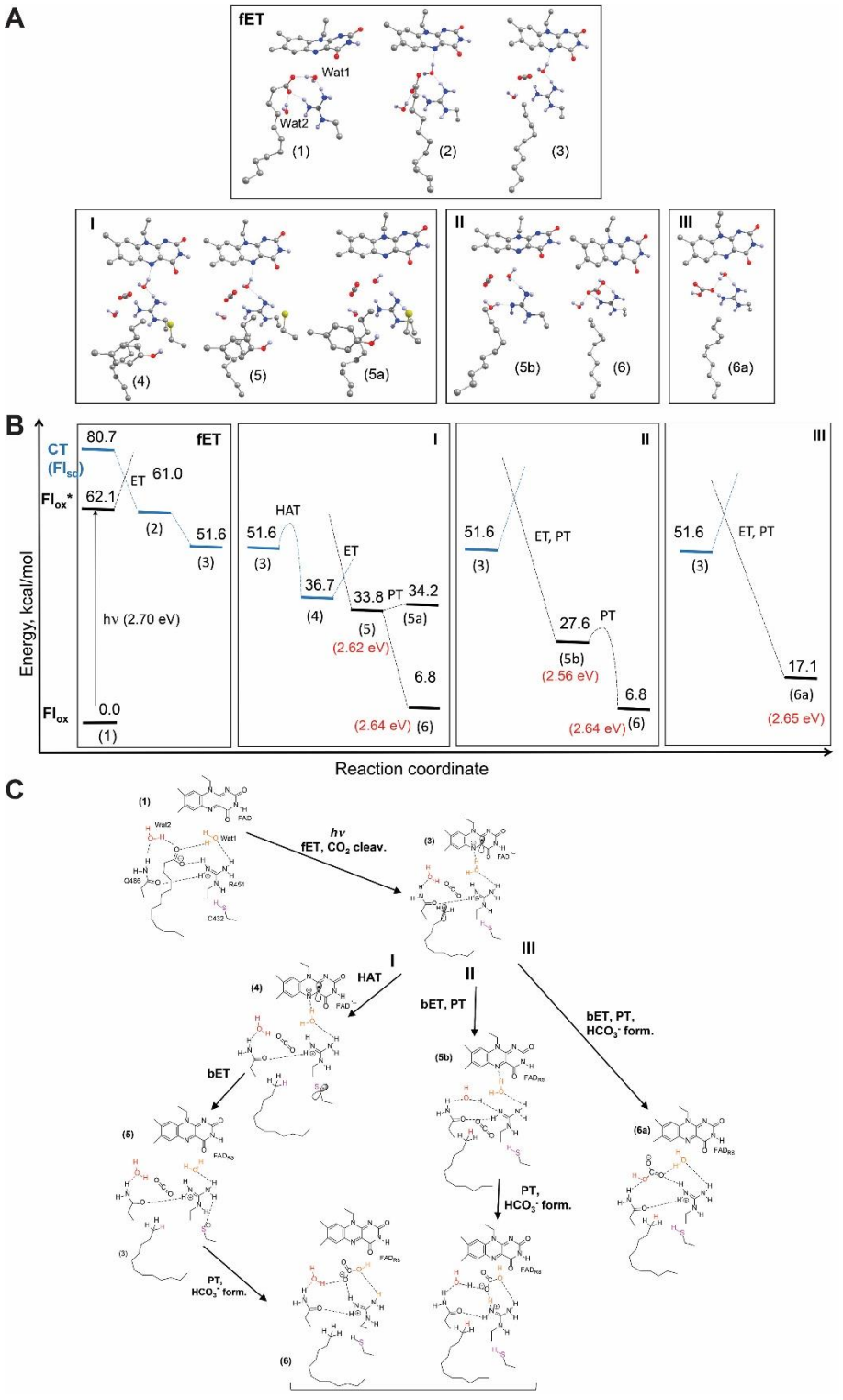
A
fET
Wat1
Wat2
(1)
(2)
(3)
I
II
III
(4)
(5)
(5a)
(5b)
(6)
(6a)
B
CT (FIsc)
FIox*
FIox
80.7
fET
ET
61.0
62.1
(2)
51.6
(3)
hν (2.70 eV)
0.0
(1)
I
HAT
51.6
(3)
36.7
(4)
ET
33.8
PT
34.2
(5)
(5a)
(2.62 eV)
6.8
(2.64 eV)
(6)
II
51.6
(3)
ET, PT
27.6
PT
(5b)
(2.56 eV)
6.8
(2.64 eV)
(6)
III
51.6
(3)
ET, PT
17.1
(6a)
(2.65 eV)
Energy, kcal/mol
Reaction coordinate
C
(1)
Wat2
Wat1
FAD
Q488
R451
C432
hν
fET, CO2 cleav.
(3)
FAD
I
II
III
HAT
(4)
FAD
bET, PT
bET, PT, HCO3- form.
bET
(5)
FADhs
(5b)
FADhs
(6a)
FADhs
PT, HCO3- form.
(3)
PT, HCO3- form.
FADhs
(6)
FADhs

1

2

Fig. 6. Plausible *Cv*FAP photoreaction pathways according to quantum-chemistry calculations. (**A)** Structural changes accompanying decarboxylation and alkane formation in the FAP active site. Flavin butterfly bending angle is 15° and 19° in the oxidized and semiquinone states, respectively. For clarity, only a small part of the active site model is shown. The complete model is presented in fig. S16. (**B**) Energies of the reactants, intermediates and products indicated in (**A**). Common to all pathways is fET mediated by Wat1 rearrangement (1) → (2) followed by CO_2 cleavage (2) → (3). Alkan formation occurs either via HAT (pathway I) or PCET (pathways II and III). Pathway I consist of alkane formation via HAT from C432 (3) → (4), flavin re-oxidation by the C432-radical (4) → (5), and C432 re-protonation and bicarbonate formation (5) → (6). Pathway II involves alkane formation via bET coupled to proton transfer (PT) from Wat2 and subsequent R451 deprotonation (3) → (5b). Bicarbonate formation from CO_2 and Wat1 recovers protonated R451 (5b) → (6). In pathway III, bET is coupled to Wat2 deprotonation and formation of bicarbonate. (3) → (6a). (**C**) Chemical scheme detailing intermediate states of fET and pathways I-III.

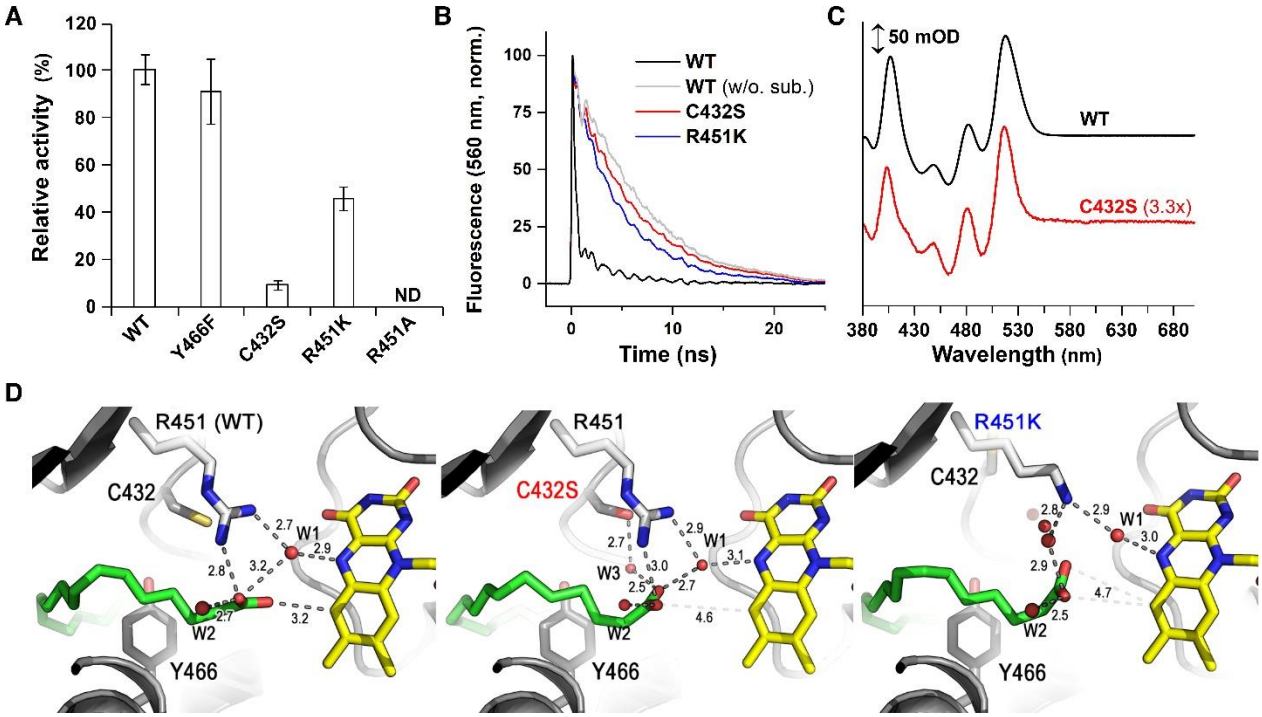

Fig. 7. Impact of mutations of conserved residues on *Cv*FAP activity, ^{1}FAD* fluorescence decay, spectrum of cryo-trapped FAD_{RS} and active site structure. (**A**) Activities of purified recombinant mutant *Cv*FAPs relative to WT (measured by gas chromatography coupled with mass spectrometry for the Y466F, R451K, and R451A mutants) in presence of *cis*-vaccenic acid as substrate. Relative activity of the C432S mutant was measured by membrane inlet mass spectrometry in order to avoid activity underestimation due to low photostability of this particular mutant under continuous illumination conditions. All activities were normalized to FAD content. Mean ± SD (n = 5 repeats). (**B**) Normalized time-resolved fluorescence at 560 nm of WT, C432S and R451K *Cv*FAP in the presence of native substrates (and after their consumption in WT); for Y466F and R451A mutants, see fig. S25B. (**C**) Light minus dark spectrum of WT and mutant C432S at 200K obtained by cryo-UV-Vis spectroscopy and normalized on FAD content. (**D**) Structure of the active site of the WT (left), C432S (middle) and R451K (right) mutants. Distances

(in Å) between substrate (green), FAD (yellow), water molecules (red) and amino acid residues (white/gray) are shown. Compared to WT, in the C432S and R451 mutants the FA carboxylate is rotated ~50° around an axis defined by the fatty acid atoms O2 and C2.

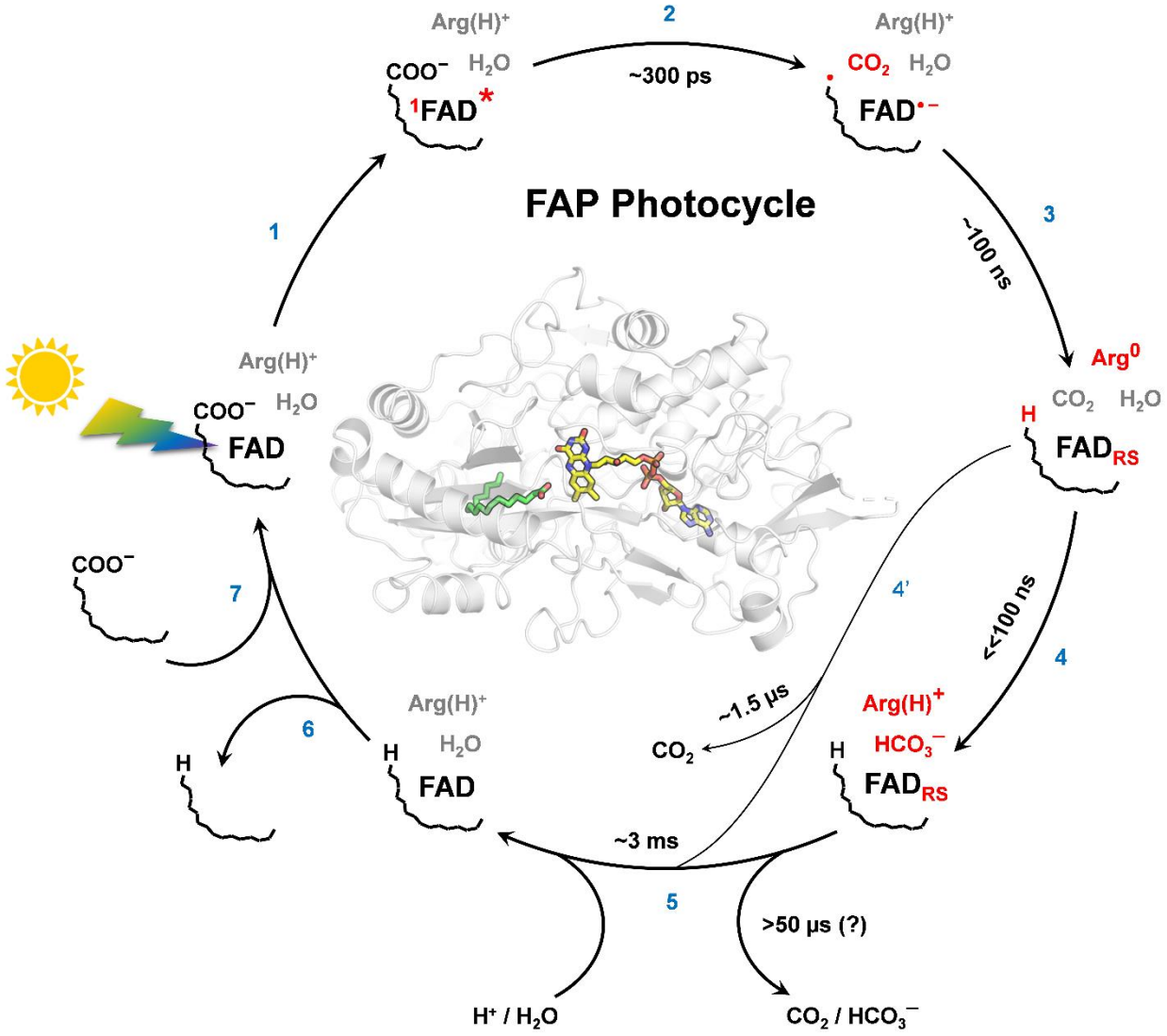

Fig. 8. Suggested *Cv*FAP photocycle. Upon light excitation (1), fET in ~300 ps from the fatty acid anion to ^{1}FAD* (observed by ultrafast fluorescence and transient absorption spectroscopies) leads to its quasi-instantaneous decarboxylation (2), as observed by TR-IR and TR-SFX and supported by the computed absence of an energy barrier. bET in ~100 ns from $FAD^{\bullet-}$ (presumably to the alkyl radical) results in formation of red-shifted (re-)oxidized flavin FAD_{RS}; the H/D *KIE* suggests bET is coupled to and/or limited by PT. Cryotrapping FTIR experiments suggest arginine as the final proton donor to the alkyl (3). Concomitantly, most CO_2 (~75%) is transformed (4) to bicarbonate as indicated by TR-IR and cryotrapping FTIR. FAD_{RS} disappears in ~3 ms (5) with a H/D *KIE* > 3, indicating coupling to PT. Upon alkane release (6), new substrate binds (7). About 25% of the formed CO_2 is not transformed to bicarbonate, likely because it migrates away from the active site within 100 ns, leaving the protein in ~1.5 µs (4'). In this minor fraction, arginine (R451) should re-protonate at latest in the ~3 ms step (5). Changes after individual steps are marked in red, time constants are for room temperature.

Supplementary Materials for

Mechanism and dynamics of fatty acid photodecarboxylase

D. Sorigué[1], K. Hadjidemetriou[2], S. Blangy[1], G. Gotthard[3], A. Bonvalet[4], N. Coquelle[5], P. Samire[1,6], A. Aleksandrov[4], L. Antonucci[4], A. Benachir[4], S. Boutet[7], M. Byrdin[2], M. Cammarata[8], S. Carbajo[7], S. Cuiné[1], R. B. Doak[9], L. Foucar[9], A. Gorel[9], M. Grünbein[9], E. Hartmann[9], R. Hienerwadel[1], M. Hilpert[9], M. Kloos[9], T. J. Lane[7], B. Légeret[1], P. Legrand[10], Y. Li-Beisson[1], S. L. Y. Moulin[1], D. Nurizzo[3], G. Peltier[1], G. Schirò[2], R. L. Shoeman[9], M. Sliwa[11], X. Solinas[4], B. Zhuang[4,6], T. R.M. Barends[9], J.-P. Colletier[2], M. Joffre[4], A. Royant[2,3], C. Berthomieu[1,*], M. Weik[2,*], T. Domratcheva[9,12,*], K. Brettel[6], M. H. Vos[4,*], I. Schlichting[9,*], P. Arnoux[1,*], P. Müller[6,*], F. Beisson[1,*]

Correspondence to: frederic.beisson@cea.fr (F.B.), pavel.muller@i2bc.paris-saclay.fr (P.M.), pascal.arnoux@cea.fr (P.A.), Ilme.Schlichting@mpimf-heidelberg.mpg.de (I.S.), marten.vos@polytechnique.edu (M.H.V.), Tatjana.Domratcheva@mpimf-heidelberg.mpg.de (T.D.), martin.weik@ibs.fr (M.W.), catherine.berthomieu@cea.fr (C.B.)

This PDF file includes:

Materials and Methods

Supplementary Text S1 to S6

Figures. S1 to S31

Tables S1 to S11

Other Supplementary Materials for this manuscript include the following:

Copies of Full wwPDB X-ray Structure Validation Report

Table of contents

Materials and Methods

Expression and purification of recombinant *Cv*FAP and mutant FAPs

The FAP used in all experiments is the previously published recombinant *Cv*FAP (*4*), from *Chlorella variabilis* NC64A (*Cv*FAP or single mutant of it) with an N-terminal truncation of 14 amino residues. This *Cv*FAP corresponds to residues 76-654 of the full-length amino acid sequence. Site-directed *Cv*FAP mutants C432A, C432S, R451A, R451K and Y466F were obtained by introducing point mutations in the previously reported FAP synthetic gene codon-optimized for *E. coli* expression (*4*). The primers used to generate the mutants and the truncated version of the *Cv*FAP are listed in Table S3; for the C432S mutant, a part of the gene (between the MfeI and EcoRI restriction sites) was synthesized (Eurofins Genomics Germany GmbH), thereby introducing the mutation, and then exchanged. Coding sequences for *Cv*FAP and its mutants were cloned into a pET-28 based expression vector containing his-tagged thioredoxin downstream the gene and recombinant proteins were expressed. The recombinant FAP and mutant proteins were produced in BL21-CodonPlus (DE3)-RIL *E. coli* cells (BL21-Rosetta (DE3) *E. coli* for the C432S mutant) cultured in TB medium at 37°C up to OD 1. At this stage, cultures were induced with 500 µM IPTG and the temperature was decreased to 17°C. Cells were grown for an additional 24 h. The cells were harvested by centrifugation at 4000*g* for 30 min and the pellet was frozen. Purification of recombinant protein was performed as previously described (*4*). Briefly, cell pellet was resuspended in lysis buffer containing 300 mM NaCl, 50 mM Tris pH 8.0, 10 mM imidazole, 5% (w/v) glycerol, 0.25 mg mL^{-1} lysozyme, 20 mM $MgSO_4$, 10 µg mL^{-1} DNase, and antiproteases (SIGMA*FAST*™ Protease Inhibitor Tablets). After resuspension, cells were lysed by sonication (sonicator probe at a frequency of 20 kHz, four 45-second cycles separated by a one-minute delay) and centrifuged during 30 min at 12,000*g*. The

supernatant was collected and the enzyme was purified by FPLC. The first purification step was made using a nickel column. Tobacco etch virus (TEV) protease (at 1 mg per 20 mg total protein) was used to cut off the His tag and the thioredoxin. A dialysis was performed overnight in the presence of TEV protease to change the buffer to 300 mM NaCl, 50 mM Tris pH 8.0, 10 mM imidazole, 5% (w/v) glycerol. A second FPLC chromatography step using a nickel column was made to separate the protein from the His-tagged thioredoxin. The last purification step made use of a gel filtration column HiLoad Superdex 200 (26/600 mm). Buffer used for this step contained 150 mM NaCl, 10 mM Tris pH 8.0, 5% (w/v) glycerol. The protein was concentrated using Amicon ® Ultra Centrifugal filters (30 kDa), flash-cooled in liquid nitrogen and stored at –80°C. Protein concentration was calculated using absorbance at 280 nm taking into account the contribution of FAD. Almost 60% of endogenous fatty acids associated with purified FAP were C18 fatty acids (fig. S27).

Analysis of FAP endogenous fatty acids by LC-MS

Briefly, 50 µL of the purified WT FAP (6 mg mL^{-1} in 150 mM NaCl, 10 mM Tris, pH 8.0, 5% (w/v) glycerol buffer) was heated at 85°C for 10 min with 50 µL of ethanol/acid acetic (0.1% v/v) and centrifuged at 14,500*g* for 10 min. The supernatant (2 µL) was analyzed by UPLC/MS/MS using a Kinetex column (C18 2.1 × 150 mm 1.7 µm, Phenomenex) mounted on an ultimate RS 3000 UPLC system (Thermo Fisher). A binary gradient system of acetonitrile−water (60:40, v/v) and isopropanol−acetonitrile (90:10, v/v), both containing 10 mM ammonium formate, was used as eluent A and B, respectively. The elution was performed with a gradient of 30 min; eluant B was increased from 7 to 97% in 26 min and held constant for 5 min, solvent B was then decreased to 7% and held constant for another 6.9 min for column re-

equilibration. The flow-rate was 0.3 mL/min. The column oven temperature was kept at 45°C. This LC system is connected to a quadrupole-time-of-flight (QTOF) 5600 mass spectrometer (AB Sciex, Framingham, MA, USA) equipped with a duo-spray ion source operating in negative mode (4500V). Identification of fatty acids was based on mass accuracy peaks from the MS scan. The percentage of each fatty acid in total fatty acids was calculated with multiquant software (AB Sciex) on the basis of intensity values of extracted masses of identified fatty acids.

FAP activity assays

FAP activities were measured by gas chromatography coupled to mass spectrometry (GC-MS) for WT and mutants Y466F, R451K, R451A and C432S. In the case of mutants with low (C432S) or no activity detected by GC-MS (R451A), the activity was also measured by membrane inlet mass spectroscopy (MIMS) using WT as a reference. For activity measurements performed by GC-MS, enzymatic assays, extraction and quantification of hydrocarbons were performed as previously described (*4*). For activity measurements based on MIMS, 20 µL of purified enzyme (WT, C432S or R451K mutant) at 30 µM concentration were added to a reaction medium composed of 1.45 mL of Tris/Citrate/Borate buffer (100 mM, pH 6.5) containing NaCl 100 mM and supplemented with 50 µL of hexadecanoic acid-1-^{13}C (10 mM in dimethylsulfoxide) and 750 units of bovine carbonic anhydrase (Sigma Aldrich C3934). The measuring chamber was thermo-regulated at 25°C, and stirred continuously and illuminated with continuous 460 nm-emitting diode (Luminus PT39-B-L21). The $^{12}CO_2$ (m/z = 44) and $^{13}CO_2$ (m/z = 45) released by FAP were monitored as described in (*41*).

FTIR spectroscopy

For experiments involving exchange of the substrates present in the FAP, 50 µL of protein at 135 mg mL^{-1} was diluted in 2 mL of buffer (150 mM NaCl, 10 mM Tris pH 8.0). Ten µL of purified palmitate or 1-^{13}C-palmitate (stock solution 100 mM in ethanol or DMSO) was added and the samples were illuminated for 10 s with white light at an intensity of 8000 µmoles m^{-2} s^{-1}. In order to remove excess substrate and proteins that could have precipitated during the incubation and illumination steps, the samples were then centrifuged 45 min at 20,000*g*. After centrifugation, the supernatant was recovered and concentrated using Amicon® Ultra Centrifugal Filters (30 kDa). In order to eliminate ethanol or DMSO, the dilution and concentration steps were repeated twice. The final FAP concentration was adjusted to 135 mg mL^{-1}.

For experiments with fully labeled ^{15}N-FAP, the recombinant FAP protein was produced in cells cultured in M9 minimal medium supplemented with $^{15}NH_4Cl$ as sole nitrogen source and purified as described above. For experiments in D_2O (**Fig. 3A**), the buffer (10 mM Tris–HCl pH 8.0 with 150 mM NaCl) was lyophilized to dry powder and the sublimated H_2O was replaced by D_2O, up to the original volume of the H_2O buffer. For sample preparation, 50 µL of purified FAP at a 135 mg mL^{-1} concentration was diluted in 1 mL of the D_2O buffer. The sample was then concentrated using Amicon® Ultra Centrifugal Filters (30 kDa). These dilution and concentration steps were carried out twice to optimize the replacement of the exchangeable protons by deuterium. The final concentration of the sample was adjusted to 135 mg mL^{-1}.

Except for exchanging substrate, all sample preparation steps were performed in the dark or under non-actinic light conditions (>550 nm) to prevent enzyme activation. For FTIR experiments, 4 µL of the protein solution was deposited between two CaF_2 windows and the

sample absorption was adjusted below 0.9 absorption units for the absorption of the main band at 1640 cm^{-1} (corresponding to the Amide I and water bending modes).

FTIR spectra were recorded with an IFS 66 FTIR spectrometer (Bruker) equipped with a MCT-A detector and a KBr beam-splitter. Experiments at 100 or 150 K were performed using a TBT N_2-flow cryostat equipped with quartz windows for transmission in the UV-Vis range and with a combination of CVD-Diamond and ZnSe windows for IR transmission. Illumination was achieved with a continuous 460 nm-emitting diode (Luminus PT39-B-L21). Light - *minus* - Dark difference spectra were obtained by subtraction of spectra recorded under illumination (Light) and before illumination (Dark). Scans (300 to 400 for each spectrum) were recorded at a 4 cm^{-1} resolution (acquisition time was between 1.5 and 2 minutes). Depending on the samples, spectra were recorded with one sample or with up to six samples (R451K mutant) and averaged to increase the signal-to-noise ratio. Similar light-induced experiments were performed in the UV-Vis domain at 100 or 200 K using a Cary 100 spectrophotometer equipped with the TBT cryostat. Spectra were measured between 380 and 600 nm with 1 nm steps, using custom-made polyethylene cuvettes with a pathlength of 1 mm. Glycerol at a 70 to 85% (v/v) concentration was added to the concentrated FAP sample (final FAD concentration around 200 µM). Spectra were normalized based on FAD content.

Protein crystallization and structure determination for static crystallography

FAP (*Cv*FAP and mutant R451A, R451K and C432S) were concentrated to around 6 mg mL^{-1} (97 µM) in 150 mM NaCl, 10 mM Tris pH 8.0, 5% (w/v) glycerol. Crystallization screening was performed using 96-wells plates in a sitting drop setup using a Freedom EVO 100 pipetting robot (Tecan). Screening was done by mixing 0.7 µL of protein at 6 mg mL^{-1} with 0.7 µL of a mother

liquor from various commercial screens. Hits were obtained in position H8 of the Stura Footprint Combination screen (20% (w/v) PEG 4000, 20% (w/v) 2-propanol, 0.1M Na-Citrate pH 5.5) at 8°C in the dark. Therefore, removing the N-terminal part of the protein did not change drastically crystallization conditions compared to the longer *Cv*FAP construct previously used (*4*). The final crystallization buffer was 25-40% (w/v) PEG 4000, 100 mM Na-Citrate pH 5.5, 10 mM spermidine. After mixing 0.7 µL of protein with 0.7 µL of crystallization buffer, crystallization plates were stored at 8°C, and diamond-shaped crystals appeared after three days and took about one week to reach their final size (around 100 × 150 × 100 μm^3). Mutants R451A, R451K and C432S crystallized under the same conditions. Visualization and manipulation of *Cv*FAP and mutant crystals were done in the dark using a microscope with a red filter eliminating wavelengths below 600 nm. For cryoprotection, crystals were transferred in a drop of mother liquor (40% (w/v) PEG 4000, 100 mM Na citrate) supplemented with 5% (w/v) glycerol before flash cooling directly in liquid nitrogen. Diffraction data were collected at the ESRF (Grenoble) on beamlines BM30A-FIP (*42*), ID29 (*43*) and ID30A-3 (*44*), at the Soleil PX1 beamline (Saint-Aubin, France) and PXII at the Swiss Light Source. Crystals of *CvF*AP, R451K and C432S belong to space group *I*222 and diffraction data were recorded respectively up to 1.8 or 2 Å resolution. Crystals of the R451A variant belong to space group $P2_12_12_1$ and diffract X-rays to 2 Å resolution. A high-resolution structure '100 K dark' was solved by molecular replacement using the medium-resolution structure (*4*) as a starting model, and other structures (referred to as '100 K light', '150 K light', 'RT dark LD', 'R451K' and 'R451A) using the 100 K dark with the Molrep program from the ccp4 suite (*45*). The '100 K light' structure was obtained after illuminating a crystal (grown at pH5.5) at 100 K, using a 5 mW 470 nm LED (see fig. S12 for spectra). The '150 K light' structure was obtained after soaking a crystal in a mother liquor in

which the citrate buffer was replaced by 100 mM Tris pH 8.5 for 10 minutes. Crystal was then flash frozen directly in liquid nitrogen and then placed in a stream of gaseous nitrogen set at 150 K. This crystal was illuminated for 30 minutes to promote the formation of FAD_{RS} state before data collection. All structures were refined using Refmac (*46*) with manual building done using the Coot program (*47*).

In crystallo optical spectroscopy of single crystals

icOS experiments were performed on 100 × 100 × 100 μm^3 WT FAP crystals at room or cryogenic temperature. In the latter case, the crystal was either cryoprotected with glycerol or MPD (2-Methyl-2,4-pentanediol). The appearance of the FAP_{RS} state was monitored at 100 K by following the evolution of the UV-Vis absorption spectrum of a FAP crystal under irradiation by a 470 nm LED at the *ic*OS Lab (*44*). Similarly, this method was used to determine the dose resulting in a reduction of the FAD by following the evolution of the absorption spectrum from FAD_{OX} to FAD_{RS}. The half-dose of X-ray photoreduction of FAP crystals was determined to be ~40 kGy at room temperature (fig. S3) on beamline BM30A-FIP (*42*) using online UV-Vis absorption microspectrophotometry (*48*). Online Raman spectroscopy to monitor X-ray induced damage to the FAD was performed on a FAP crystal at 100 K on beamline ID29 (*43*), as previously described (*49*). Most of the peaks hardly show any decrease in their intensity (fig. S4B,C), in contrast with an online Raman study showing an X-ray-induced butterfly bending of a protein-encased flavin that comes with reduction and is accompanied by a decrease of Raman bands intensities (*26*). Only five stretching modes are affected upon progressive irradiation (4 decreases, 1 increase) and are thus characteristic of the change in electronic structure of the FAD.

Absorbed X-ray dose calculations in in crystallo optical spectroscopy and synchrotron crystallography experiments

Average absorbed doses were calculated using RADDOSE-3D (http://raddo.se/) (*50*) using data collection parameters and characteristics of the used beamlines. All crystals were of 100 × 100 × 100 μm^3 dimensions. The low dose room temperature crystallography experiment was performed on beamline ID30A-3 (*51*) on a single WT crystal using an HC1 humidity controller with a humidity level calculated from the composition of the mother liquor (*52*). The X-ray beam of ID30A-3 (fixed energy of 12.81 keV) has a Gaussian profile of 18 µm (horizontal) × 14 µm (vertical) dimensions (measured at FWHM). The X-ray flux was attenuated to 4.8×10^{10} ph s^{-1}, and a 110° oscillation wedge of diffraction data was collected in 11 s, which amounts to an average absorbed dose of 38 kGy for the irradiated part of the crystal. The high resolution cryogenic data collection of *Cv*FAP was performed on beamline ID29 (*43*) on a single crystal cryocooled at 100 K. The X-ray beam of ID29 (energy set to 12.73 keV) has a Gaussian profile of 40 µm (horizontal) × 30 µm (vertical) dimensions (measured at FWHM) and is collimated with a 50 µm aperture. The X-ray flux was attenuated to 4.1×10^{10} ph s^{-1}, and a 127° oscillation wedge of diffraction data was collected in 47 s, which amounts to an average absorbed dose of 154 kGy for the irradiated part of the crystal. The online Raman microspectrophotometry experiment was performed at cryogenic temperature on beamline ID29 at an energy of 11.56 keV with an X-ray flux of 6.8×10^{10} ph s^{-1} on a crystal irradiated for 0 to 240 s. The UV-Vis absorption microspectrophotometry experiment was performed at room temperature using the

HC1 humidity controller on beamline BM30A-FIP (*42*) at an energy of 12.66 keV with a 300 × 300 μm^2 top-hat beam with a flux of 4.1 × 10^{10} ph s^{-1} on a crystal irradiated from 0 to 1280 s.

Time-resolved fluorescence on ps to ns timescales

Fluorescence kinetics (in **Figs. 3A** and **7B,** and fig. S25A,B) were monitored on a set-up described previously (*4*, *53*), using a Nd:YAG laser as the excitation light source (Continuum Leopard SS-10, pulse duration of 100 ps, 355 nm, energy attenuated to ~25 μJ cm^{-2}, repetition rate 2 Hz). Strong (~5 mJ) or saturating (~10 mJ) pre-flashes at 470 nm of 5 ns duration were used to consume the native substrate when required; (**Fig 7B**, fig. S25A,B) were delivered by a Nd:YAG-pumped optical parametric oscillator (Brillant B/Rainbow, Quantel, France). The detection system consisted of a Hamamatsu microchannel plate photomultiplier tube R2566U-11P (under 3.6 kV) connected to a digital oscilloscope (Infiniium 81004B from Agilent, bandwidth DC-10 GHz, sampling rate 40 GSa/s). The samples were contained in a 2×2×10 mm cell with self-masking solid black walls and four clear windows (Starna). Excitation pulses entered through the 2×10 mm window and fluorescence was detected in front of the 2×2 mm window). An OG-530 Schott orange glass optical filter and a 560 nm interference filter (with a 10 nm bandwidth) were placed between the sample and the detector.

Fluorescence traces shown in **Figs. 3A** and **7B** and fig. S25A,B are mostly averages of 64 signals (or only 16 in the case of the signals of WT after saturating pre-flashes in fig. S25A). ~45 μM WT and 40 – 70 μM mutant *Cv*FAP proteins were used in the presence of the native substrate(s). The signals WT w/o substrate (**Fig. 7B** and fig. S25A,B**)** were recorded posterior to 10 strong (~5 mJ) pre-flashes at 470 nm, which have consumed essentially all the bound fatty acids in the excited/probed volume (see fig. S25A: the lack of significant further slowing of the

fluorescence decay after 3 saturating (~10 mJ) pre-flashes as compared to 2 pre-flashes indicates that already after the 2nd pre-flash less than ~10% of the excited flavins were quenched by a substrate; 10 strong (~5 mJ) pre-flashes have consumed virtually all the native substrates).

Transient absorption spectroscopy on ns to ms timescales

Transient absorption kinetics were recorded on a set-up described previously (*54*, *55*). The FAD cofactor in FAP was excited at 470 nm by laser flashes of 5 ns duration and an energy in the order of 4 mJ cm^{-2}, delivered by a Nd:YAG-pumped optical parametric oscillator (Brillant B/Rainbow, Quantel, France). The monitoring light was provided by three continuous wave lasers: 376 nm – collimated diode laser Toptica iBeam smart 375-S (up to 120 mW); 488 nm – DPSS laser Picarro Cyan-20 from Spectra-Physics (20 mW); 515 nm – DPSS laser Cobolt FandangoTM (150 mW). The sample cell was identical to that used in the time-resolved fluorescence experiments (2×2×10 mm). The monitoring light was attenuated by neutral density filters and mechanically chopped to produce a rectangular pulse of 140 μs duration and an energy in the order of 1 μJ at the entrance of the cell (2x2 mm window), thus avoiding significant actinic effects. This pulse was synchronized with the excitation laser flash entering the sample through the 2×10 mm window. The signals were recorded using an Alphalas UPD-500-UP photodiode (rise time <500 ps; sensitive area 0.5 mm^2) connected via a Femto HCA electronic signal amplifier (DC-325 MHz, 28 dB) to a Tektronix DSA602A digital oscilloscope with bandwidth limit set to 100 MHz.

For experiments on the ms timescale, the chopper was removed, the monitoring light was strongly attenuated by additional neutral density filters (to ~2% intensity) and a Tektronix AM502 amplifier with an upper bandwidth limit set to 100 kHz was used.

Transient absorption kinetics were measured on *Cv*FAP proteins (~45 µM WT, 40 - 70 µM mutants) containing their native substrates (see **Fig. 1**). Addition of ~500 µM palmitic, vaccenic or oleic acid in control experiments did not affect the kinetics, nor the signal amplitudes, only the signal-to-noise ratio worsened (fatty acids are poorly soluble in water and their addition causes scattering of the monitoring light). The state of the samples was controlled by UV-Vis spectroscopy (Uvikon XS spectrophotometer from Secomam) prior to each experiment. All signals shown in **Fig. 3B,C** and in figs. S10 and S25C–F were recorded upon single flash excitation.

For time-resolved spectroscopic experiments in D_2O (**Fig. 3**), our standard buffer (100 mM Tris-HCl buffer at pH 8.2 with 150 mM NaCl) was lyophilized to dry powder and the sublimated H_2O was replaced by D_2O, adding up to the original volume of the H_2O buffer. Isolated FAP samples in the H_2O buffer were passed twice over size-exclusion columns (MicroBio-Spin, Bio-Gel P-6), pre-washed and saturated with the D_2O buffer. The same method of buffer exchange was used to obtain FAP samples at other than 'standard' pH values (fig. S10A,B).

Ultrafast visible absorption and fluorescence spectroscopy

Ultrafast fluorescence and absorption spectroscopy with full spectral resolution and configured for flavoproteins was performed as described (*56*), with a setup operating at 500 Hz. The ~100 fs, ~100 nJ, excitation pulses were centered at 390 nm and focused on the sample with a spot size of ~100 µm. The fluorescence setup (*57*) is based on Kerr-gating and CS_2 was used as a Kerr medium, yielding a temporal response of ~1 ps. For the absorption experiments the

excitation pulses were polarized at magic angle with respect to the white light continuum probe pulses to avoid photoselection effects. The sample (~200 µM of *Cv*FAP containing FAD) was circulated through a 1 mm optical path length cell of local design at a speed sufficient to allow sample renewal between shots. For the experiments in the presence of substrate, as-purified samples were used (fatty acid solubility limitations prohibited the presence of significantly supra-stoichiometric amounts of substrate) and total absorbed photons during the experiments were limited to less than ~20% of the flavins, as verified by absorption spectroscopy.

Excitation power dependence

For experiments on the dependence of the transient absorption signal on the excitation power using picosecond pulses, the 1-mm thick β-barium borate (BBO) crystal used for frequency doubling of the 780-nm fundamental beam was replaced by a custom 20-mm thick BBO crystal (Eksma). In this way, the output energy was distributed over a 4-ps interval due to the group velocity mismatch between the 780-nm and 390-nm beams (*58*). Under conditions allowing a pulse energy up to 1.4 µJ at the level of the sample, the FWHM was found to be ~2.7 ps. Under these conditions, at 1.4 µJ some pre-continuum was generated in the sample, leading to modest distortion of the transient spectra up to ~500 nm. Results are shown in fig. S28.

Multi-scale transient infrared absorption spectroscopy

Time-resolved visible pump mid-infrared (IR) probe spectroscopy on the picosecond to microsecond timescale was performed with a system based on two independent femtosecond laser amplifiers (*59*). Pump pulses centered at 400 nm are generated by frequency doubling of

1-kHz 150-fs 800-nm pulses using a first regenerative amplifier (Hurricane, Spectra-Physics). The output of a second 1-kHz Titanium:Sapphire regenerative amplifier (LIBRA-HE, Coherent) allowed to generate IR probe pulses by difference frequency mixing of the signal and idler pulses delivered by an optical parametric amplifier. For the present experiments, the pulses were centered at 2350 cm^{-1} and have a spectral width (FWHM) of 170 cm^{-1}.

Time delays between pump and probe pulses were rapidly scanned from picoseconds to microseconds thanks to a method combining Arbitrary-Detuning ASynchronous OPtical Sampling (AD-ASOPS) (*32, 60*) and appropriate selection of amplified pulses that is described in details in reference (*33*). This electronically-controlled approach allowed a very broad time delay distribution without any moving part, while the temporal resolution can be as good as 200 fs. To enhance the signal-to-noise ratio on the picosecond timescale here we chose to average spectra over 50-ps time bins, effectively limiting the time resolution.

Pump pulses were chopped mechanically at a frequency of 500 Hz. The pump pulse energy was 700 nJ, and the angle between pump and probe polarizations was set to 90°. The transmitted IR probe spectra were measured with a CCD by chirped-pulse up-conversion (*61*). IR spectra were calibrated by comparison to atmospheric absorption lines (*61*). The part of the set-up involving IR light was placed under dry air to limit the amplitude of these absorption lines, and in particular those of atmospheric CO_2.

Pump and probe pulses were focused on the sample on a 120-µm FWHM spot. The sample (~2 mM flavin concentration) was placed between two round CaF_2 windows separated by a 100 µm thick spacer that leaves a circulation channel in the center, in a Harrick Scientific Products DLC-M25 mount. The sample was continuously circulated using a peristaltic pump connected to the cell so that the irradiated sample was nearly refreshed between two subsequent

laser shots. The temporal overlap between pump and probe pulses is determined using the signal of a GaAs wafer.

Each differential absorption plot shown in **Fig 2C** corresponds to the average of 33 000 laser shots. Baseline fluctuations were removed using a polynomial fit outside of the CO_2 band and the average baseline at two negative time delays (-5 ns and –1 ns) was subtracted from all spectra, thus removing any contribution from the non-refreshed fraction of the sample. Both visible and infrared transient spectra data sets were analyzed using Glotaran (*62*).

Microcrystal growth and injection for TR-SFX

Crystallization screening was performed under red-light conditions at 8°C using 96-wells plates in batch condition. Screening was done by mixing 20 µL of *Cv*FAP in solution 1 (150 mM NaCl, 10 mM Tris pH 8.0, 5% (w/v) glycerol) at different concentrations (3-12 mg mL^{-1}) with 20 µL of mother liquor containing 100 mM Na citrate pH 5.5, 10 mM spermidine and PEG 4000 (12 to 28% w/v). A 1:1 mixture of 19% (w/v) PEG 4000, 0.1 M sodium citrate pH 5.5, 10 mM spermidine (solution 2) and solution 1 at a protein concentration of 6 mg mL^{-1} yielded two types of crystals, hereafter referred to as needle and diamond crystals based on their respective shapes. Efforts to obtain only one crystal form were not successful. The diffraction quality of needle shaped crystals ($30 \times 3 \times 3$ μm^3) was assessed at the microfocus beamline ID23-2 (*63*) of the ESRF (Grenoble) at room temperature (RT; using MicroRT^{TM} mounts from MiTeGen) and at 100 K (in a cryo-loop) after buffer exchange by centrifugation and resuspension in 20% (v/v) glycerol, 23% (w/v) PEG 4000, 100 mM Na citrate pH 5.5 and 10 mM spermidine. The diffraction limit, as judged in the program *Dozor* implemented in *MeshAndCollect* data-

collection workflow (*64*) was 2.3 Å at 100 K and 2.6 Å at room temperature. For TR-SFX experiments, large quantities of microcrystals were generated using the batch method by gently mixing 4 mL of solution 1 at a protein concentration of 6 mg in mL^{-1} with 4 mL of solution 2 at 8°C. 1.5 grs of *Cv*FAP was crystallized using this approach. Batches consisting mostly of needle shaped crystals (100 – 200 × 2 – 5 × 2 – 5 μm^3) were selected and stored at 4°C. Prior to injection, they were reduced in size to about 10 × 2 – 5 × 2 – 5 μm^3 (fig. S29) by flowing a slurry containing 20% (v/v) microcrystals at 2.5 mL min^{-1} successively through a 20 μm and a 10 μm stainless steel filter in tandem. After filtering, the crystal suspension was concentrated to 60% (v/v) by centrifugation and removal of the supernatant and placed in a stainless steel sample syringe for injection. The syringe was installed on an anti-settling device (*65*) equipped with a Peltier element-cooled syringe holder at 4°C. The crystals were injected with a gas dynamic virtual nozzle (GDVN (*66*)), using sample capillaries with an inner diameter of 75 or 100 μm, into the microfocus vacuum chamber of the CXI end station (*67*) of the Linac Coherent Light Source (LCLS) at the SLAC National Accelerator Laboratory. The sample was injected at flow rates between 35 and 55 μL min^{-1} in a liquid jet of about 5 μm in diameter.

Picosecond pump-laser excitation of FAP microcrystals in TR-SFX experiments

*Cv*FAP microcrystals (~10 × 4 × 4 μm^3, $P2_1$, two molecules (A,B) in the asymmetric unit) were photoexcited with pulses of a Ti:sapphire laser (400 nm wavelength; 11 μJ/ pulse, circularly polarized). The pulse length was 4 ps (FWHM), achieved by detuning the pulse compressor. The pump-laser beam of Gaussian shape was focused to a spot of 155 μm (FWHM), resulting in a peak power density of 10 GW/cm^2. Under these excitation conditions, and assuming an extinction coefficient of 9250 $M^{-1}cm^{-1}$ (estimated from Fig. 3A in Sorigué *et al.* 2017 under the

assumption that the extinction coefficient at 467 nm is 11300 $M^{-1}cm^{-1}$) 2.8 photons were absorbed on average per FAD chromophore. The number of absorbed photons in the front and the rear of the crystals (*68*) do not deviate considerably from the average (fig. S30) because of the large penetration depth of 400 nm light into the FAP crystals used (1/e penetration depth at 400 nm is 47 μm, see fig. S30). Excitation-power dependent transient absorption spectroscopy carried out on *Cv*FAP in solution at the pump-power density (10 GW/cm^2) of the TR-SFX experiment (fig. S28) showed that multi-photon processes had decayed by the first TR-SFX time point (20 ps).

TR-SFX data collection and online monitoring

SFX data were collected (LT59, 22, 24 and 25 Nov 2018) in the microfocus chamber of CXI with the LCLS producing X-ray pulses (nominal photon energy 9.5 keV, pulse length 23 fs) at a repetition rate of 120 Hz. The X-ray beam was focused to 1 μm × 1 μm (FWHM), the nominal pulse energy at the sample position was ~1.3 mJ, taking into account a beamline transmission of > 60%. Data were acquired with the CSPAD detector (*69*) operating in a dual-gain mode. During data collection, the hutch lights were switched off. On-line monitoring of the diffraction data, such as estimation of the hit rate, the fraction of multiple hits and of the pixel saturation and diffraction resolution, was carried out using the CFEL–ASG Software Suite (CASS) (*70*). TR-SFX data were recorded according to a 400-nm pump (see above) – X-ray probe scheme, with pump-probe delays of 20 ps, 900 ps, 300 ns and 2 μs. Two dark images without laser excitation and 15 light images with laser excitation were collected in a pseudo-randomly interleaved fashion.

SFX data processing

On-line and off-line hit finding and dark vs. light image-sorting (without and with pump-laser excitation, respectively) was performed using NanoPeakCell (*71*). Hit-finding parameters were adjusted after visual inspection of the first diffraction patterns using the NanoPeakCell graphical interface. A total of 8,141,555 images were collected for all five datasets (dark, light_20ps, light_900ps, light_300ns, light_2μs), 1,001,248 of which were identified as hits, corresponding to an overall hit-rate of 12.3%.

CrystFEL v.0.8.0 (*72*) was used for detector geometry optimization, indexing (*Xgandalf* (*73*)), integration (*rings-grad* method) and merging with the Monte Carlo (MC) algorithm *process_hkl*. MC averaging included the scaling option. The sample-to-detector distance was refined iteratively until the unit cell parameters displayed a Gaussian distribution (*74*). The overall indexing rate (indexed images / hits) was about 25%. A resolution cutoff of 2.0 Å was chosen based on acentric moments of the E distribution except for the light_2μs dataset which was cut at 2.2 Å resolution. The space group is $P2_1$, with two molecules (A, B) in the asymmetric unit. SFX data processing statistics are shown in (**Table S2**).

In view of the large number of images used in the data sets, the high values of R_{split} indicate an underlying problem. We explored different space groups but the problem remained, even when a lower symmetry was used, suggesting inherent disorder in the data as the fundamental issue. There are several possible types of disorder that could affect the SFX data. These include inherent variability in the microcrystals, which we cannot exclude at this time, as well as some particular complications arising from the cell parameters of our FAP microcrystals:

a = 61.4 Å, b = 60.0 Å, c = 182.9 Å and α = 90°, β = 90.6°, γ = 90°. Thus, not only are the cell parameters close to orthorhombic, but also $a \approx b \approx \frac{1}{3}c$. This results in an indexing ambiguity, as it is possible for an indexing algorithm to confuse the three axes. In addition, there is the possibility of actual pseudomerohedral twinning in the crystals. All of these possible complications would result in a high R_{split} and noisy maps. At present, none of our attempts at resolving this static disorder (whether real or apparent) by reindexing of individual images based on their correlation with the rest of the data set, twin refinement, or the screening of various indexing schemes at the data processing stage, have resulted in a satisfactory solution.

SFX dark structure solution and refinement

The microcrystals used for SFX are of another crystal form than those used for the conventional crystallography experiments; specifically, their space group is $P2_1$ with two molecules in the asymmetric unit as opposed to $I222$ with a single molecule in the asymmetric unit for most of the synchrotron structures (the R451K mutant crystallized in $P2_12_12_1$ (one molecule in the asymmetric unit) with very similar unit cell parameters as the $P2_1$ SFX crystal form). The dark structure corresponding to the data set without laser excitation was phased by molecular replacement with *Phaser* (*75*) using as a search model the synchrotron '100 K dark' structure of FAP described in this study devoid of all cofactors and water molecules and with atomic B-factors reset to 30 $Å^2$. This resulted in an unambiguous solution with two molecules in the asymmetric unit and an excellent electron density map showing clear density for the FAD cofactor as well as the fatty acid molecules. Structure refinement was performed using *Refmac5* (*46*) and included positional and isotropic individual B-factor refinement in reciprocal space (25-2 Å resolution range) with local NCS restraints. Model building and real space refinement were

performed using *Coot* (*47*). In the initial model, the isoalloxazine ring of the oxidized FAD cofactor was constrained to be planar. $mF_{obs} - DF_{calc}$ peaks clearly indicated a significant deviation from planarity (fig. S6). Therefore, once refinement of the protein moiety, waters and substrate molecules was completed, the restraints of the isoalloxazine ring were relaxed by increasing the estimated standard deviation of the isoalloxazine torsion angles in the .cif file. In the final model (PDB accession code 6ZH7), the isoalloxazine ring of the FAD cofactor is clearly bent (C4-N5-N10-C9 dihedral angle (butterfly bending angle), deviating from planarity by 14.3° in molecule A and by 11.7° in molecule B; **Fig. 1E,** fig. S7). Figures were made with *PyMOL* (*76*). SFX data-structure refinement statistics are shown in table S2.

Calculation of difference Fourier maps between SFX data sets with and without laser excitation

To assess structural changes induced by illumination, q-weighted (*77*) difference Fourier electron density maps ($F_{obs}^{light\_20ps} - F_{obs}^{dark}$, $F_{obs}^{light\_900ps} - F_{obs}^{dark}$, $F_{obs}^{light\_300ns} - F_{obs}^{dark}$, $F_{obs}^{light\_2\mu s} - F_{obs}^{dark}$) were calculated in CNS (78) using scripts published in Wickstrand et al. (79) and the SFX dark-state structure for phasing. The maps are shown in fig. S31 for each of the two FAP molecules present in the asymmetric unit (A and B). As described in the main text, the calculated q-weighted difference electron density maps show a different extent of decarboxylation of the fatty acid at the various time delays, as well as various positive and negative peaks throughout the active site and beyond. The maps contain some differences between the two molecules in the asymmetric unit, suggesting either differences in the structural change upon illumination or simply the maps' noise level. We therefore also averaged the maps using a procedure based on local averaging (*80*). This resulted in the maps shown in **Fig. 5**.

Molecular dynamics simulations

The model for the Molecular Dynamics (MD) simulations was built using the '100 K dark' structure of FAP obtained in this work. The FAD cofactor in the oxidized state and two stearic acids (STE) present in the crystal structure were included in the model. The simulations included protein residues within a 24 Å sphere, centered on the N5 atom of the bound FAD cofactor in the crystal structure. Protein atoms between 20 and 24 Å from the sphere's center were harmonically restrained to their experimentally determined positions. Protonation states of histidines were assigned by visual inspection and ideal stereochemistry; protonation states of other residues were assigned using PROPKA (*81*, *82*). In addition to crystal waters, a 71-Å cubic box of water was overlaid, and waters overlapping with the protein, FAD, two STE's and crystal water molecules were removed. Periodic boundary conditions were assumed; i.e. the entire 71-Å box was replicated periodically in all directions. All long range electrostatic interactions were computed by the particle mesh Ewald method (*83*). No counterions were included as the system was electrically neutral. MD simulations were performed at constant temperature (300K) and pressure, after 200 ps of thermalization. The CHARMM36 force field (*84*, *85*) was used for the protein and the modified version of the TIP3P water model (*85–87*). The force field parameters for the FAD_{OX} cofactor developed recently were used (*27*). Calculations were done with the NAMD program (*88*). One hundred nanoseconds of MD simulations were performed.

Quantum chemistry calculations

The computations were performed using the Firefly software (*89*), which is partially based on the US GAMESS code (*90*). A series of molecular models was employed in the calculations; all

models were prepared using the coordinates of the '100 K dark' crystal structure. Geometries were optimized using the density-functional theory restricted or unrestricted formalism with the B3LYP functional (*91*, *92*) supplemented with the dispersion energy correction D3 (*93*). The cc-pvdz basis set (*94*) was used throughout. During geometry optimization, some atoms were constrained (fig. S16) to mimic the structural relaxation of the active site being part of the protein structure. The vertical and adiabatic electron affinities and ionization potentials were computed using the R-/U-B3LYP energy calculations. The excitation energies were computed with the XMCQDPT2 method (*95*) applying a denominator shift for intruder-state avoidance (edshft=0.02) (*96*). The zero-order CASSCF wave functions were obtained using a state-averaging procedure with equal weighting for all states included in the calculations (*97*). The so-called minimum-size active space CASSCF calculations were performed for the FAP active site following the approach previously extensively tested and applied for calculations of various chromophores in proteins (*98–102*). The results obtained the FAP modes with different active spaces and numbers of states were compared to evaluate consistency of the predicted excitation energies. All excitation energies that are compared were obtained with the identical active space of the flavin molecular orbitals. The generalized Mulliken-Hush scheme (*103*) was used in conjunction with the XMCQDPT2 calculations to derive electronic couplings as previously suggested for the bacteriorhodopsin active site (*102*).

Comparison of GMC oxidoreductase sequences

Sequences of 14 FAPs and 16 other GMC oxidoreductases that do not group with FAPs in a phylogenetic tree were retrieved from various databases (table S4). FAP sequences were the characterized *Cv*FAP and *Chlamydomonas* FAP plus 12 other putative FAPs from various algal

groups. The non-FAP GMC oxidoreductases were from a wide variety of organisms. Protein sequences were aligned using the Muscle algorithm (*104*) and alignment was visualized and inspected with SeaView (*105*). Logo sequences were generated using WebLogo.

Supplementary Text

S1. Study of FAD bending by low-dose X-ray crystallography, microspectrophotometry and molecular dynamics

FAD reduction occurs during FAP X-ray exposure (with a half dose of 40 kGy) as shown by 20 X-ray dose-dependent *in crystallo* UV-Vis absorption microspectrophotometry scans (fig. S3), *i.e.* well below the dose of the '100 K dark' data (154 kGy). However, a dark-state low-dose (38 kGy) 1.9 Å resolution structure determined of FAP data collected at a synchrotron ('RT dark LD') (fig. S4A and table S1) and a Raman microspectrophotometry experiment performed at 100 K at X-ray doses from 0 to 1.9 MGy (fig. S4B,C) suggest that FAD is in a bent conformation in the initial oxidized state (bending angle is 13.7° in the 'RT dark LD'). FAD bending in the oxidized state is also supported by a molecular dynamics simulation using a recently developed flavin force field (*27*) that yielded an oxidized FAD cofactor bent on average by about 20° (fig. S5A,B).

S2. Band assignment in FTIR spectroscopy

The Light - *minus* - Dark difference spectra recorded at 100 or 150 K (**Fig. 4A**) display vibrational contributions from all groups affected by the light-induced reaction. Negative bands correspond to the Dark state and positive ones to the Light state. Bands from the protein, FAD,

the substrate and products are expected to contribute to these FTIR difference spectra. To identify contributions from the substrate and the reaction products, we substituted the native substrate by ^{12}C or 1-^{13}C-labeled palmitate, as described in the Materials and Methods section, and compared the spectra (**Fig. 4A**, spectra *i* and *ii*). Only IR modes involving the carboxyl group of the substrate and products are expected to be significantly affected by this labeling. Therefore, they can be identified in a ^{12}C - *minus* - ^{13}C difference spectrum calculated from spectra recorded at 100 K (**Fig. 4A**, spectrum *iii*) and from spectra recorded at 150 K (**Fig. 4A**, spectrum *iv*). In addition, downshifts of the band frequencies are expected upon ^{13}C- labeling. In spectra *iii* and *iv*, the negative bands at 1541 and 1391 cm^{-1} are shifted to 1510 and 1371 cm^{-1}, respectively, upon 1-^{13}C-labeling, and are therefore assigned to the $\nu_{as}(COO^-)$ and $\nu_s(COO^-)$ IR modes of ^{12}C-palmitate. The modes frequencies show that the fatty acid is deprotonated in the active site. They appear as two thin and intense bands, indicating a very well defined position of the substrate in the protein. In addition, the frequencies of the $\nu_{as}(COO^-)$ and $\nu_s(COO^-)$ modes are lower than those of carboxylate groups in solution (*106*), which indicates a strong interaction with positive charges within the protein. This is in agreement with the substrate position identified in the '100 K dark' synchrotron structure, showing a clear interaction of the substrate carboxylate group with the side chain of R451 and with carbon C6 of the isoalloxazine ring of FAD **(Fig. 1)**.

The $\nu_{as}(CO_2)$ mode of the CO_2 product of the reaction is clearly identified at 2340 cm^{-1} at 100 K **(Fig. 4A** panel *v***)**. The frequency is lower than that observed for CO_2 in solution (2342 cm^{-1}, (*31*)) and similar to that observed upon *Cv*FAP illumination at room temperature by TR-IR in the time window from 100 ps to 1 µs (**Fig. 2C,E** and fig. S9). For samples with 1-^{13}C-palmitate, it is downshifted by –66 cm^{-1} to 2274 cm^{-1} as expected for $^{13}CO_2$ (*107*).

At 150 K, the intensity of the $\nu_{as}(CO_2)$ mode is very low **(Fig. 4A** panel *v***)**. Between 1800 and 1200 cm^{-1}, bicarbonate in solution is characterized by two main IR modes, the $\nu_{as}(CO)$ and $\nu_s(CO)$ modes at 1650 - 1620 cm^{-1} and 1365 - 1355 cm^{-1}, respectively, and by a small amplitude $\delta(COH)$ mode at 1300 - 1250 cm^{-1} (*108, 109*). Upon ^{13}C labeling, frequency downshifts of –64 and –25 cm^{-1} were reported for the $\nu_{as}(CO)$ and $\nu_s(CO)$ modes of bicarbonate in solution. The frequency of the $\nu_{as}(CO)$ and $\nu_s(CO)$ modes and the frequency shifts upon ^{13}C-labeling are sensitive to the interactions (hydrogen bonding, ionic) formed by bicarbonate with its environment (*109*). In the ^{12}C - *minus* - ^{13}C difference spectrum recorded with FAP at 150 K (**Fig. 4A** panel *iv*), positive bands at 1646 and 1352 cm^{-1} are downshifted to 1614 and 1318 cm^{-1} upon 1-^{13}C-palmitate labeling. The bands' frequency and shifts upon ^{13}C-labeling are fully consistent with contributions of bicarbonate. The FTIR data show that formation of bicarbonate dominates over formation of CO_2 after FAP illumination at 150 K.

Contributions from protein side chain modes are also expected in the FTIR difference spectra. In particular, the cysteine sulfhydryl group contributes by its $\nu(SH)$ mode in a specific region of the FTIR spectra between 2700 and 2480 cm^{-1}, depending on the interactions formed by the sulfhydryl group and its environment (*110*, *111*). FTIR spectra in the spectral range where cysteine $\nu(SH)$ vibrations contribute show that, upon illumination of *Cv*FAP at 100 or 150 K, a band shift occurs from ≈ 2540 (dark) to ≈ 2550 cm^{-1} (light) **(Fig. 4A** panel *vi***)**. This indicates that a SH group is present at 100 and 150 K, both in the Dark and Light states and that it undergoes a slight change in hydrogen bonding interactions (*110, 111*). The lack of a negative band in this region suggests that there is no stable cysteine deprotonation after illumination at cryogenic temperatures.

Tyrosine side chains contribute with an intense ν_{19}(CC) mode at 1515 cm^{-1} in the infrared, which is sensitive to the Tyr protonation state and appears at 1495 - 1500 cm^{-1} for tyrosinate (*106*, *112*). Spectra recorded from the WT and the Y466F mutant are highly similar in this spectral region (fig. S26A). This rules out significant contribution of the Y466 side chain mode in the 1515 - 1495 cm^{-1} region of the light-induced FTIR difference spectrum. This is a strong indication that there is no stable deprotonation of Y466 after illumination at cryogenic temperatures.

In an attempt to identify IR bands of the R451 side chain, we compared light-induced FTIR difference spectra recorded at 100 K with WT FAP and with the R451K mutant (fig. S26B). Unfortunately, only a very small-amplitude FTIR difference spectrum was obtained from the R451K mutant, and the spectrum was very different from that obtained from the WT FAP. This prevented any conclusion on the contributions of the R451 side chain to the spectrum obtained from WT FAP. On the other hand, we can formulate hypotheses from the spectra recorded with WT FAP in H_2O, in D_2O, and with fully ^{15}N-labeled FAP (**Fig. 4A**, panels *vii-viii*). The side chain of arginine is characterized by two intense IR modes, the ν_{as} and $\nu_s(C_2N_3H_5)$ guanidinium modes, at *circa* 1675 cm^{-1} and 1635 cm^{-1}, respectively, in H_2O (*106*). These modes are downshifted by –65 and –47 cm^{-1} in D_2O, respectively (*113*). These modes are highly sensitive to interactions formed by the Arg side chain and its deprotonation, as detailed in Braiman *et al.* (*114*). Characteristics of these bands are their large intensity in D_2O as well as the larger effect of H/D exchange compared to that expected for other IR modes contributing in the 1700 - 1600 cm^{-1} region, *i.e.*, mainly Amide I modes of peptide carbonyl groups (which are not expected to shift by more than 10 cm^{-1} in D_2O). Therefore, they can be distinguished from other contributions by comparing spectra recorded in H_2O and D_2O and especially in calculated H_2O

- *minus* - D_2O spectra, such as those presented in **Fig. 4A** panel *viii*. If we cannot unambiguously assign the Arg side chain modes in H_2O, due to possible overlap with other bands, we can propose that the band observed at 1606 cm^{-1} in D_2O is due to an arginine ν_s(guanidium) mode. Indeed, the negative band observed at 1606 cm^{-1} in D_2O has no clear counterpart in the close-by region in H_2O : it therefore results from a downshift in D_2O of at least –30 cm^{-1}. In addition, this band is intense. To our knowledge, there is no other amino acid side chain that could show such a contribution in D_2O (and not in H_2O) in this spectral region. We can also exclude contributions from Amide II modes at this frequency since Amide II modes contribute usually in the 1580 - 1500 cm^{-1} region in H_2O, and are downshifted upon H/D exchange by about –100 cm^{-1} to the 1500 - 1400 cm^{-1} region. The band at 1606 cm^{-1} is clearly a well defined, thin negative band present in the spectrum recorded with samples in D_2O and not in H_2O. This frequency value (1606 cm^{-1}) is well above that expected for Amide II modes in D_2O. To further support the proposed assignment, we produced fully ^{15}N-labeled FAP and recorded spectra with samples in H_2O and D_2O. The corresponding H_2O - *minus* - D_2O difference spectrum recorded at 100 K shows that the band at 1606 cm^{-1} is downshifted to 1597 cm^{-1} (**Fig. 4A** panel *viii*). This strongly supports the assignment of this band to an arginine side chain mode. In addition, it allows us to exclude the assignment of this band to an Amide I mode, since, upon ^{15}N-labeling, the Amide I bands are expected to shift only by a few wavenumbers (–1 to –3 cm^{-1}) due to a small coupling between the ν(C=O) mode and the NH in plane bending mode. Although FAP ^{15}N-labeling induces downshifts of bands of the H_2O - *minus* - D_2O spectrum in the 1703 - 1686 cm^{-1} region and at 1644/1631 cm^{-1} (to 1638/1624 cm^{-1}), we cannot assign some of these bands to arginine side chain modes, since contributions from Asn or Gln side chains cannot be excluded in this spectral range, as well as small downshifts of Amide I bands. However, the frequency and

intensity of the band at 1606 cm^{-1}, the effect of H/D exchange and $^{14}N/^{15}N$ exchange on this band altogether point to a contribution from an arginine side chain mode in D_2O at 1606 cm^{-1}. This band is negative, with no clear positive counterpart. This is also clear in the H_2O - *minus* - D_2O difference spectrum of **Fig. 4A** spectrum *viii* calculated from spectra in *vii*. This is a strong argument to infer a large change in properties of the Arg side chain after illumination of the sample at 100 K. Therefore, the FTIR data are consistent with a model in which an Arg side chain is deprotonated after illumination at 100 K. In their study of bacteriorhodopsin, Braiman *et al.* assigned a weak IR band at circa 1555 cm^{-1} to deprotonated guanidium (*114*). This band occurs in the region where peptide Amide II modes also contribute, so that any assignment would be ambiguous in this region in **Fig. 4A** spectrum *viii*.

S3. Time-resolved fluorescence in solution on ps to ns timescales

WT CvFAP

The fluorescence kinetics of the WT *Cv*FAP in the presence of the native substrate(s) (**Fig. 3A**, **Fig. 7B** and fig S25A,B) show that the substrate quenches the singlet excited state ^{1}FAD*, shortening its lifetime from ~6.5 ns (typical time constant for unquenched flavins (*115*)) to ~300 ps (both in H_2O and D_2O, see **Fig. 3A**). Interestingly, fluorescence signals recorded in the presence of one or two native substrate molecules (see X-ray structures in **Fig. 1**) or even >10-fold excess of added substrate still contain a non-negligible contribution of the slow phase (corresponding to ~15% of the recorded signal amplitude). This suggests that there is always a certain fraction of enzymes that upon photoexcitation cannot undergo the productive fET step (inactive proteins), but in which the ^{1}FAD* undergoes intersystem-crossing (ISC) to a non-

productive triplet state ^{3}FAD* (like in the absence of a substrate as shown previously *(4)*), which then decays back to the ground state FAD in ~80 μs. Noteworthy, competition between fET and ISC in a homogeneous sample should lead to a monoexponential decay of the ^{1}FAD* fluorescence. It hence seems that the fate of ^{1}FAD* is decided prior to the FAD excitation. Reasons for the small fraction of inactive WT proteins can be diverse, ranging from an overstabilization of the carboxylate by a transient bidentate interaction with R451, to an incomplete occupation of the substrate binding site or an incomplete deprotonation of the substrate therein.

CvFAP mutants

In the Y466F mutant, the time-resolved fluorescence signal (fig. S25B) is very similar to that of the WT protein. Apart from a slightly increased relative amplitude of the slower phase (indicative of a minor increase in the fraction of flavins that cannot undergo fET and eventually leading to a slightly lower enzymatic activity; **Fig. 7A**), ^{1}FAD* fluorescence quenching by ET from the substrate seems to occur with the same kinetics in Y466F as in WT (*i.e.*, in ~300 ps).

Fluorescence signals of the R451 mutants (see **Fig. 7B** for R451K and fig. S25B for R451A) resemble those obtained for the WT *Cv*FAP after the photocatalytic consumption of the native substrate (fig. S25A), in spite of the fact that the substrates are still present at the catalytic site (see **Fig. 7D** (R451K) & fig. S26D (R451A)).

In the R451K mutant, ^{1}FAD* fluorescence decays significantly faster than in the WT after the consumption of the substrate (**Fig. 7B**). Due to the systemic initial perturbations in the signal caused by the detection system, we are not capable of distinguishing whether the decay is

monophasic or biphasic in this case. A biexponential fit yields time constants of ~300 ps and ~5 ns, *i.e.*, similar to those for the WT in the presence of substrate (~300 ps and ~6.5 ns), but with an inverse amplitude ratio (*i.e.*, ~15% fast phase and ~85% slow phase). A monoexponential fit yields a time constant of ~4.5 ns (*vs.* ~6.5 ns for WT after substrate consumption). If we assume the decay is monoexponential and reflects two competing processes, fET and ISC, the rate constant k_{obs} (= $1/\tau_{obs}$) is a sum of $k_{fET} + k_{ISC}$. For τ_{obs} of 4.5 ns (R451K) and 6.5 ns (WT without substrate, *i.e.*, 100% ISC), we obtain k_{obs} of 2.2×10^8 s^{-1} and 1.54×10^8 s^{-1}, respectively. If we further assume that the k_{ISC} is the same in WT and in the mutant (which may or may not be the case; *i.e.*, $k_{ISC} = 1.54\times10^8$ s^{-1}), we obtain k_{fET} of 6.8×10^7 s^{-1}, which converts into an intrinsic time constant for fET of ~15 ns in R451K. Since k_{fET} is ~30% of k_{obs}, ^{1}FAD* should decay by ~30% fET and ~70% ISC in R451K. The tests of enzymatic activity (**Fig. 7A**), and the transient absorption signals (fig. S25D) show that the R451K mutant is indeed partially active (~45% of WT, which would correspond to ~38% fET, since fET yield in WT is ~85%). The small difference in the two numbers (30% *vs.* 38%) could be explained in at least threeways: 1) k_{ISC} might be slightly slower in R451K than in WT, 2) the fET yield for the native substrates (in the fluorescence experiment) may be slightly lower than for the added ones (in the activity test), or 3) the recovery of the catalytic site (steps 5 to 7 of our photocycle, **Fig. 8**) might be slightly faster in the mutant than in the WT protein, which would not affect the yield of fET but it would increase the apparent enzymatic activity under continuous illumination conditions (as it seems to be the case for Y466F; see discussion in the supplementary text S4). In any case, the observed decrease in both fET yield and enzymatic activity under steady-state illumination is likely due to an increased FAD-substrate distance (from 3.2 Å in WT to 4.6 Å in R451K) and to an

'overstabilization' of the fatty acid carboxylate by the presence of the additional water molecule Wat3 (see **Fig. 7D**).

In the R451A mutant, ^{1}FAD* fluorescence decays monophasically with a time constant of ~8 ns and no rapid process indicative of its quenching by productive fET is observed (fig. S25B). Accordingly, the transient absorption data (fig. S25E) do not display any significant evolution, which could be attributed to the bET reaction on the sub-μs timescale, and the mutant exhibits essentially no enzymatic activity (**Fig. 7A**). We propose that the inactivity of the R451A mutant is primarily due to the 'wrong' protonation state of the substrate, which, in the absence of a positive counterion on residue 451, is most probably protonated and thus cannot reduce the photoexcited ^{1}FAD*.

In the C432S mutant, fluorescence of ^{1}FAD* (**Fig. 7B**) decays apparently monophasically in ~6.0 ns (*i.e.*, only slightly faster than in WT after consumption of the native substrate (~6.5 ns), indicating that fET does occur to a small extent in C432S). Partial consumption of the native substrates (by 10 strong flashes at 470 nm) slowed the fluorescence decay down to ~6.2 ns, addition of a five-fold excess of oleic acid, on the other hand, led to its minor acceleration to ~5.7 ns (not shown). Applying the same procedure for the estimation of intrinsic fET rate as we used for R451K above, the time constants of ~6.0 ns (C432S with native substrates) and ~5.7 ns (C432S in the presence of excess oleic acid) translate into k_{fET} of 1.3×10^7 s^{-1} (τ_{fET} of ~80 ns) and 2.1×10^7 s^{-1} (τ_{fET} of ~50 ns), respectively, and fET yields of 8 and 12%, respectively. The latter two numbers are both consistent with the ~10% activity of C432S determined by membrane inlet mass spectroscopy.

S4. Transient absorption spectroscopy in solution on ns to ms timescales

WT CvFAP

Based on our initial characterizations of the FAP photocycle by transient absorption spectroscopy (*4*), we have chosen three characteristic wavelengths to monitor FAD-associated spectral changes following its photoexcitation in WT and mutant *Cv*FAP: 376 nm, where $FAD^{\bullet-}$ absorbs more strongly than oxidized FAD (observation of $FAD^{\bullet-}$ formation and decay); 488 nm, where the $FAD^{\bullet-}$ anion absorption is weaker than that of oxidized FAD (observation of FAD absorption bleaching and its recovery upon $FAD^{\bullet-}$ reoxidation); and finally 515 nm, where $FAD^{\bullet-}$ absorbs more than oxidized FAD but less than the red-shifted re-oxidized FAD (observation of $FAD^{\bullet-}$ formation and its conversion into FAD_{RS} on the sub-µs timescale, and the subsequent decay of FAD_{RS} back to the "dark-state" FAD on the ms timescale).

Both fluorescence and transient absorption signals obtained for the truncated *Cv*FAP in H_2O buffer (**Fig. 3**) are highly similar to those obtained previously for the full-length *Cv*FAP (Fig. 5C and fig. S6 in (*4*)), indicating that the truncation of the protein does not affect its photochemistry.

A change in pH (of the 100 mM Tris Buffer) in the interval between 7.5 and 9.1 (*i.e.*, around the enzymatic optimum according to fig. S3D in (*4*)) affected neither the kinetics, nor the amplitude of any of the signals (fig. S10A,B).

Consumption of the native substrates by saturating flashes at 470 nm (in the absence of added substrate) did, as expected, lead to a decrease in the amplitude of the signals recorded on the ms timescale but their kinetics remained essentially unaffected (fig. S10C).

On the contrary, the exchange of an H_2O buffer to a D_2O buffer had no impact on the amplitudes of the observed signals but it did substantially slow down the kinetics of both processes followed by transient absorption spectroscopy: the reoxidation of $FAD^{\bullet-}$ to FAD_{RS} (from ~100 ns to ~200 ns; **Fig. 3B**) and the reversion of FAD_{RS} back to the "dark-state" FAD (from ~3 ms to ~10 ms; **Fig. 3C**). For the former process ($FAD^{\bullet-}$ reoxidation), Heyes and coworkers (*24*) reported a kinetic isotope effect (*KIE*) of only ~1.2 (lifetimes of ~180 ns and ~215 ns in H_2O and D_2O, respectively) at 520 nm and concluded that 'H-transfer events did not have a major effect on the rate of formation of the red-shifted flavin intermediate'. The origin of the deviation from our data (obtained at three different wavelengths, including 515 nm; see **Fig. 3B**) might be an insufficient time resolution in Ref. (*24*) that not only affected the faster kinetics (in H_2O) more than the slower one (in D_2O) but also made it difficult to discriminate the rise in a few hundreds of nanoseconds from the preceding much faster (step-like) rise due to $FAD^{\bullet-}$ formation, that is not affected by the isotope exchange (compare Fig. 3A in Ref. (*24*) with our **Fig. 3B** (signals at 515 nm)). The much stronger *KIE* documented here argues for direct coupling of bET to a $H^+/H^\bullet$ transfer event. Note that an indirect coupling due to, *e.g.*, structural changes in the substrate/flavin region induced by solvation of the protein in D_2O instead of H_2O cannot be reconciled with the absence of *KIE* on fET from the substrate to the excited flavin (**Fig. 3A**).

The absence of a pH effect in the interval between 7.5 and 9.1 (fig. S10A,B) indicates that if these reaction steps (steps 3 and 5 in **Fig. 8**) involve PT (or HAT), the pK_a of the proton or hydrogen atom donor lies outside of the tested pH interval (note that the pK_a of the used Tris buffer is ~8.1; as the total buffer concentration was constant in these experiments, the concentration of its acidic and basic forms changed strongly with pH, but this did not affect the kinetics, indicating that Tris-buffer molecules are not directly involved). Finally, the lack of

influence of the availability of a fresh substrate on the kinetics of FAD_{RS} reversion to the "dark-state" FAD (fig. S10C) suggests that the disappearance of the transient FAD red shift is not associated with binding of a new substrate.

CvFAP mutants

Like in the case of fluorescence signals (fig. S25B), transient absorption changes in the Y466F mutant on the sub-microsecond time scale reflecting bET/FAD_{RS} formation (fig. S25C) also resemble those obtained for the WT protein (**Fig. 3B** or fig. S10A), even though a moderate acceleration of bET can be noticed in Y466F. Together with the almost identical FTIR signals of WT and Y466F *Cv*FAP (fig. S26A) and a high enzymatic activity of this mutant (**Fig. 7A**), all our results suggest that tyrosine Y466 does not directly participate in any of the PT/HAT or ET steps in the FAP photocycle. However, Heyes *et al.* (*24*) have shown that the decay of the FAD_{RS} species (step 5 in our photocycle; **Fig. 8**) is substantially accelerated in the Y466F mutant (we observed the same phenomenon - acceleration of the FAD_{RS} decay from ~3 ms in WT to ~300 μs in Y466F; data not shown). Heyes *et al.* suggest that it 'might reflect differences in local reorganization in the active site'. Alternatively, since the phenyl group of Y466 makes a hydrogen bond to the backbone carbonyl oxygen of T430 (O-O distance of 2.6 Å), serving as a "clasp" around the alkyl chain, one can also speculate that F466 (being incapable of such an interaction) is likely more flexible than Y466 and that the missing "clasp" might facilitate egress of the product chain through the tunnel (lined by the second FA) connecting to the solvent. This could allow for a faster recovery of the active site after the photoreaction (steps 5 to 7 in our photocycle; **Fig. 8**). According to fig. S10A in (*24*), the Y466F mutant seems to be a bit more active than WT in the first minutes of the activity test (under continuous illumination). Given that the quantum yield of fET is actually slightly lower in Y466F than in WT (the relative

amplitude of the slower phase in the ^{1}FAD* fluorescence decay corresponding to futile ISC is a bit more pronounced in Y466F than in WT, see fig. S25B), this observation can only be explained in terms of a faster recovery of the active site in Y466F (combined with a faster photodegradation of the mutant protein).

Transient absorption changes recorded for the R451K and R451A mutants on the sub-microsecond timescale are shown in fig. S25D and E, respectively. In the signals of the R451K mutant, the amplitudes of the first kinetic phase (reflecting the reoxidation of $FAD^{\bullet-}$ to FAD_{RS}) are considerably smaller than in WT *Cv*FAP (corresponding to ~30% bET, judging from the signal at 488 nm, fig. S25D), but this process seems to be markedly accelerated (from ~100 ns in WT to ~30 ns in R451K; fig. S25D). While the 515 nm signal remains constant after the initial ~30 ns phase, we observe further partial reversion of the negative absorption change at 488 nm with a time constant of a few microseconds. The additional phase at 488 nm most probably corresponds to decay of free FAD triplet (characteristic ^{3}FAD* lifetime in solution is ~3 μs; note that the absorption change due to ^{3}FAD* should be much more pronounced at 488 nm than at 515 nm; see fig. S6D in (*4*)). Remarkably, in the (dark) crystal structure of the R451K mutant (**Fig. 7D**), the side chain of C432 changes its position so that its SH group recedes farther both from the FAD (from 6.9 Å to 9.6 Å) and from the C2 atom of the substrate (from 4.7 Å to 9.2 Å). If reduction of the alkyl radical were due to HAT from C432 followed by bET from $FAD^{\bullet-}$ to the C432 radical (without large structural rearrangement following CO_2 formation), one would expect the reoxidation of $FAD^{\bullet-}$ to slow down in the R451K mutant. The opposite observation argues against both the hydrogen atom transfer from and the coupled back electron transfer to the C432 residue as the mechanism of alkyl radical reduction by $FAD^{\bullet-}$. On the other hand, the

higher acidity of lysine should increase the driving force for a PT from the residue 451 (coupled to bET from $FAD^{\bullet-}$) to the alkyl radical in the arginine to lysine mutant.

In the case of the R451A mutant, we observe essentially only step-like absorption changes at both selected wavelengths (fig. S25E), compatible with the formation of a protein-bound FAD triplet (with a lifetime of ~80 μs; see fig. S6E,F in (*4*)): the signal recorded at 488 nm very much resembles that recorded for the WT protein after consumption of the native substrate (see fig. S6D in (*4*)). Yet, the signal at 515 nm in the R451A mutant shows a significant negative absorption change (instead of almost zero in WT after substrate consumption), which is probably caused by a pronounced (~8 nm) red shift in the 'dark state' FAD spectrum in R451A (see fig. S24D or inset of fig. S25E). The minor initial phase seen in the 488 nm signal (fig. S25E) likely reflects ISC from ^{1}FAD* to ^{3}FAD* (~8 ns; see fig. S25B).

Transient absorption changes at 488 nm recorded for the C432S mutant on the ns and μs timescales (fig. S25F) also resemble those recorded for the WT protein after consumption of the native substrate (see fig. S6D,E in (*4*)), indicating that the formation and decay of ^{3}FAD* are the dominating processes (compared to WT, ^{3}FAD* decay is mildly accelerated in C432S: from ~80 μs to ~30 μs; see lower inset of fig. S25F)(compared to WT, 3FAD* decay is mildly accelerated in C432S: from ~80 μs to ~30 μs; see lower inset of fig. S25F). At 515 nm (where the signal WT FAP w/o substrate in fig. S6D in (*4*) returns to almost zero after the initial ^{1}FAD* decay phase in a few ns), however, the signal remains markedly positive in C432S (with an amplitude corresponding to ~15% of WT with substrate) and most (about ⅔) of this positive absorption change decays in ~3 ms (upper inset of fig. S25F), *i.e.*, with the same kinetics as the FAD_{RS} decays in the WT protein (see also Fig. 3D in *(24)*). As evidenced by cryo-trapping (**Fig. 7C**),

FAD_{RS} indeed forms in the C432S mutant and while we could not properly resolve the kinetics of its formation, we attribute the ~3 ms decay to its disappearance.

S5. Time-resolved fluorescence spectroscopy of *Cv*FAP crystals

Even though most crystalline proteins are biologically active, their reaction kinetics often differ from the solution state (*116*, *117*). In preparation for TR-SFX experiments, we assessed the kinetics of FAP in the crystalline and solution state by carrying out fluorescence-decay measurements. For solution experiments, the 6 mg mL^{-1} FAP solution was diluted to 0.375 mg mL^{-1} in buffer (50 mM Tris pH 8.5, 100 mM NaCl). Experiments on crystalline FAP were carried out on a suspension of microcrystals (1% (v/v); each about 10 × 2 – 5 × 2 – 5 μm^3 in size) in 19% (w/v) PEG 4000, 100 mM Na citrate pH 5.5, 10 mM spermidine. Single photon counting fluorescence experiments were performed using an excitation pulse (400 nm) delivered by doubling (harmonic generator, SHG, APE) a femtosecond Ti:sapphire laser (800 nm, Coherent Chameleon Ultra II, 80 MHz, 180 fs) coupled to a pulse picker (APE, 4 MHz). Emission decays were measured using an FT200 Picoquant spectrometer and analyzed by the *FluoFit* software. By using a low excitation power (100 nW), a small excitation beam size (100 µm) and a large volume (2 mL) of sample that was constantly stirred, fluorescence spectra could be acquired for about 3 min without notable chromophore bleaching (as assessed by a UV-Vis absorption spectrum). The measured emission decay of ^{1}FAD* at 560 nm (fig. S15) was fitted by a weighted-sum of three exponentials. For FAP in solution, the retrieved time constants corresponding to three different FAD populations were 318 ps (± 5 ps), 980 ps (± 30 ps) and 3.9 ns (± 40 ps) with contributions of 76%, 16% and 8%, respectively. The first population corresponds to FAD undergoing efficient fET, the second to a population undergoing less

efficient fET or being photobleached, and the last to a non-reactive population. For the crystal suspension, similar time constants were retrieved (320 ps, 1.45 ns, 4.8 ns) but with different contributions (62%, 14%, 24%), leading to an overall fluorescence decay that is slower in crystals than in solution (fig. S15). To assess whether the decrease in the population undergoing efficient fET in the crystal suspension (62%) compared to solution (72%) is due to the difference in pH (5.5 in crystals versus 8.5 in solution), the experiment was repeated on a FAP solution (0.375 mg mL^{-1} protein concentration) in the crystal buffer (19% (w/v) PEG 4000, 100 mM Na citrate pH 5.5, 10 mM spermidine). The contribution of the population with a fluorescence decay of 322 ps was 75%, indicating that it is the crystal packing and not the pH value that decreases the efficiency of fET in the microcrystal suspension from 72% to 62%. Most importantly, however, we conclude that fET proceeds on the same timescale in crystals (320 ps) as in solution (318 ps at pH 8.5, 322 ps at pH 5.5).

S6. Quantum chemistry study of the *Cv*FAP reaction mechanism

6.1. Model of the CvFAP active site

We computed a series of active-site models to analyze the chemical mechanism of the *Cv*FAP photoenzyme. Starting from the coordinates of the high-resolution 100 K dark X-ray structure, a model (272 atoms) containing a fatty acid (FA; $C_{10}H_{21}CO_2^-$), oxidized flavin, water molecules Wat1 and Wat2 and conserved residues of the FAP active site (fig. S16) was prepared; its geometry (1) was optimized using the R-B3LYP method. The structures of the diradical charge-transfer (CT) intermediates (3) and (4), and intermediates/products (5), (5a), (5b), (6), and (6a) formed after back electron transfer (bET) were obtained by gradually introducing the desired

changes of the initial atomic coordinates to the optimized geometry (1) and subsequent geometry optimization with the restricted (R-) or unrestricted (U-) B3LYP method depending on the electronic state of interest. The energies and energy gradients of the optimized geometries are listed in table S5**.**

The flavin demonstrates noticeable butterfly bending (in both oxidized and semiquinone state) in all optimized active-site geometries, indicating that the intermolecular interactions leading to bending are accounted for by our active site model. These interactions involve not only the hydrogen bonds suggested by the distances in the high-resolution crystal structure, but also by charge-transfer interactions between the flavin and protein, e.g. the electron-donating polypeptide loop comprising A171-T172, as demonstrated by excitation energies and electronic couplings (tables S6, S7).

6.2. Forward electron transfer (fET) is facilitated by rearrangement of Wat1

Fig. 6 and fig. S22 illustrates hydrogen-bonding interactions of the fatty acid carboxylate in the dark state (1) and the proposed rearrangement of Wat1 (2). In the dark state (1), the carboxylate forms multiple hydrogen bonds with surrounding residues and notably, with two water molecules Wat1 and Wat2 resolved in the high-resolution crystal structures. Wat1 is positioned between the flavin and R451, donating hydrogen bonds to the carbonyl backbone of S574 and fatty acid carboxylate (O...O distance is 2.78 and 2.71 Å, respectively), and accepting a hydrogen bond from R451 (O...N distance is 2.70 Å). Wat2 accepts a hydrogen bond from Q486 (O...N distance is 2.80 Å), and donates hydrogen bonds to the carbonyl backbone of S573 and carboxylate (O...O distance is 2.84 and 2.67 Å, respectively). All distances are given for the optimized structure (1).

Attempts to optimize a geometry with Wat1 hydrogen-bonded with N5-flavin failed. Structure (2) featuring the Wat1 - flavin N5 hydrogen bond undergoes rearrangement to structure (1) during geometry optimization. The preferred interaction of Wat1 is consistent with the negative charges on the hydrogen-bond accepting atoms of the surrounding groups: (-0.38) – O of the carboxylate, (-0.20) – N5-flavin, and (-0.31) – O of the S573 backbone carbonyl (the charges are given for geometry (2) according to the Mulliken analysis of the B3LYP electron density).

The excitation spectrum in table S6 includes the excited states of the flavin and charge-transfer (CT) states corresponding to electron transfer from the protein to the flavin. Among the computed states at geometry (1), two transitions with high oscillator strengths predict two absorption bands at 459 and 350 nm (computed energies 2.70 and 3.54 eV, respectively) in agreement with the optical spectrum of oxidized FAD. The transition at 2.36 eV corresponds to a $n\pi^*$ excitation of the N5 lone pair of flavin with a weak oscillator strength. The transitions indicated as charge transfer (CT) correspond to electron transfer from the protein to flavin, namely from the side chains of Y466 and C432 as well as backbone and side chains of the A171-T172 stretch. The CT transitions, as expected, have weak oscillator strengths.

Surprisingly, we did not find a state corresponding to electron abstraction from the fatty acid carboxylate by flavin among the CT states computed at (1). All our attempts to obtain the CASSCF solution with the carboxylate MOs contributing to the active space failed. Obviously, multiple hydrogen bonds weaken the carboxylate electron-donor ability, in particular interactions with Wat1 and Wat2. To demonstrate the effect of these water molecules, we computed excited states for geometry (2) and additionally for geometry (1) from which we excluded Wat2 (indicated as (1)-wo-Wat2 in table S6). Rearrangement of Wat1 in (2) favors electron abstraction from the carboxylate because breakage of the hydrogen bond between Wat1

and carboxylate reduces the carboxylate negative charge stabilization whereas formation of a hydrogen bond between Wat1 and N5 stabilizes the negative charge of the flavin radical anion. We obtained the CT fatty acid energy 2.8 eV for model (1)-wo-Wat2 and 1.8 eV for model (2).

We propose that rearrangement of Wat1 is triggered by flavin photoexcitation. Indeed, a charge-transfer interaction with the loop forming the flavin binding pocket (CT A171-T172 state in table S6) may facilitate Wat1 rearrangement following flavin photoexcitation. A significant electronic coupling between the excited flavin and A171-T172 (40 meV; table S7) indicates that the photoexcited flavin is readily converted to the flavin radical anion that becomes stabilized by a hydrogen bond from Wat1. This Wat1 rearrangement in (2) not only reduces the CT fatty acid energy, but also increases the electronic coupling driving electron abstraction from the fatty acid carboxylate to 47 meV (table S7).

6.3. Fatty acid decarboxylation in the charge-transfer (CT) state

To characterize fatty acid decarboxylation triggered by electron abstraction, we performed relaxed-scan energy calculations along the OCO bending coordinate for a reduced model of the active site (fig. S18) consisting of the fatty acid radical, several side chains and Wat2. This model was computed with the U-B3LYP method to obtain an estimate of the decarboxylation energy barrier for the fatty acid radical in the FAP active site. The relaxed geometry scan for the OCO bending coordinate indicates that CO_2 dissociation from the fatty acid radical proceeds without any energy barrier, whereas the energy of the alkyl radical and CO_2 products is substantially lower than the energy of the initial fatty acid radical. The dissociation is accompanied by rotation of the CO_2 group with respect to the alkyl chain.

6.4. Stabilization of the alkyl-radical intermediate in FAP

Formation of the alkyl and flavin radicals in the FAP active site was modeled starting from the coordinates of the partially optimized geometry (2) containing Wat1 hydrogen bonded to flavin N5. The OCO angle in the fatty acid was increased to 160 degrees and the geometry was optimized in the triplet state (unpaired electrons on the alkyl and flavin radicals) using the U-B3LYP method. Optimization led to CO_2 dissociation. Changing the coordinates of the alkyl radical in order to decrease the distance between the CH_2(rad) center and Y466 side chain (which is suggested by the substantial electronic coupling of these radicals; 142 meV in table S7) followed by geometry optimization yielded structure (3). The flavin geometry remained bent in the radical-anion state.The excited-state calculations (table S11) demonstrate that the diradical CT state becomes the ground state of structure (3) whereas the closed-shell (CS) state, corresponding to bET, is more than 3 eV above the CT diradical state. Two electronic transitions (0-1) and (0-2) with high oscillator strengths predict the flavin radical absorption to be red-shifted compared to the oxidized flavin which is consistent with spectroscopy data on FAP and other flavoproteins.

6.5. Pathways leading to alkane formation

6.5.1. HAT pathway involving Cys432

Theoretically, the alkyl radical can be converted to the alkane by hydrogen atom transfer (HAT) from Y466 or C432. For the possible HAT process, Y466 is ruled out by the experimental data obtained for the Y466F mutant showing almost unperturbed electron-transfer kinetics in comparison to the wild type. To address HAT from C432, we optimized the geometries of the diradical intermediate, resulting from the HAT reaction (4) using the UB3YP method. At the

optimized geometry (4), flavin re-oxidation was modelled by switching the electronic state from the diradical to the closed shell (CS), continuing geometry optimization with the R-B3LYP method. Obtained intermediate (5) contains oxidized flavin and deprotonated thiol C432. Intermediate (5a) was obtained by proton transfer (PT) along the hydrogen bond of R451 with C432 in (5) and R-B3LYP geometry optimization. Reaction (3) → (4) is energetically favorable (energy decrease by 15 kcal/mol; table S5), and it has a 8 kcal/mol energy barrier (estimated using a truncated model; figure S18). Much less energetically favorable is subsequent bET (4) → (5) (only 3 kcal/mol energy reduction; table S5). The excitation energies in table S11 suggest that flavin-radical absorption band might blue-shift in intermediate (4) in comparison to intermediate (3) (2.67 and 2.44 eV) whereas the CS energy (corresponding to bET) is lower in (4) than in (3) (0.83 and 3.14 eV). Electronic coupling driving bET from flavin to C432 radicals is only 4 meV (table S7), indicating that flavin re-oxidation by C432 might be limited by electronic coupling.

6.5.2. PCET pathways involving Wat1, Wat2, and Arg451

We modelled bET for geometry (3) by continuing its geometry optimization in the closed-shell state with R-B3LYP. The optimization demonstrated an increase of interactions between Wat2 and alkane anion suggesting protonation of the alkane in concert with bET. This protonation yielded alkane and OH^- anion that obtained a proton from R451 recovering Wat2 in geometry (5) (fig. S19). The energy of (5) is 27 kcal/mol higher than the energy of (1) (table S5) due to the presence of deprotonated R451, and hence, it is conceivable that (5) undergoes further stabilization (fig. S19). The energy decreases when Wat1 forms a hydrogen bond with R451 instead of Wat2. Further substantial stabilization by about 15 kcal/mol involves R451 protonation by Wat1 and bicarbonate formation from the hydroxyl anion OH^- derived from Wat1

and CO_2 (6). The energy barrier for (5) → (6) was estimated by relaxed energy scan calculations (fig. S19). The energy barrier for bicarbonate formation facilitated by re-protonation of R451 is about 4 kcal/mol. Bicarbonate formation might involve Wat2 instead of Wat1: the hydroxyl anion OH^- derived from Wat2 directly binds CO_2 (5b). The bicarbonate involving Wat2 is 10 kcal/mol less energetically favorable than formation involving Wat1.

The reaction scheme (**Fig. 6C**) highlights specific roles of Wat1 and Wat2 in the proposed catalytic mechanism. Alkane formation involves Wat2 and R451 as primary and secondary proton donors, respectively. However, deprotonated arginine is a high-energy species, and its reprotonation by either Wat1 or Wat2 followed by bicarbonate formation is energetically favorable. Irrespective of the origin, the bicarbonate is rather stable with respect to back conversion to CO_2, since protonated R451 is a rather poor acid for bicarbonate destabilization (fig. S19). An alternative stronger acid cannot be suggested by our present computations.

Thus, our calculations starting from high-resolution crystal structures suggest that FAP needs two waters, Wat1 and Wat2, interacting with the substrate at the active site for its functional mechanism. The distinct chemical roles of these waters are defined by their interactions at the active site. Wat1 facilitates fET by stabilizing the flavin radical anion whereas Wat2 serves as a primary proton donor during the alkane formation. In addition, both Wat1 and Wat2 may participate in the formation of the bicarbonate byproduct by interacting with R451 hence facilitating the unusual for arginine proton-donor function. According to our current active site model, Wat1 is slightly more preferred than Wat2 for bicarbonate formation.

6.6. Red-shifted intermediate of FAP

Table S8 presents computed excitation spectra of species (5), (5a), (5b) and (6) that are candidates for the spectroscopically identified red-shifted flavin state FAD_{RS}. The flavin excitation energy decreases for all candidates compared to the dark state (1). The spectral shift results from moving the anionic charge away from the flavin (geometries (5), (6), and (6a)) or from charge neutralization and Wat1 hydrogen bonding to flavin N5 (geometry (5a). The flavin butterfly bending angle and distances from the anionic or neutral CO_2 fragment to flavin N5 in the FAD_{RS} candidate structures are shown in fig. S20.

6.7. Effects of the C432S mutation on fET

To address the effect of the C432S mutation, a model of the active site (275 atoms) was prepared, in a similar way as the WT model, from the coordinates of the C432S X-ray structure. The calculations were performed for structures ($1^{C/S}$) and ($2^{C/S}$) that are analogous to structures (1) and (2) of WT. Interaction with an additional water molecule (Wat3; fig. S22) further reduce the ability of the bicarbonate to donate an electron to excited flavin. By computing excitation energies (table S10), we demonstrate the effect of water molecules Wat2 and Wat3 on the CT energy. Stabilization of the carboxylate with Wat3 increases the energy of the CT fatty acid by 0.2 eV in comparison to WT. The CT A171-T172 energy also increases in C432S. At the same time, the excited flavin energy does not change in the mutant model in comparison to WT. This energy charge (decrease of the S_1 energy in comparison to the CT energies) suggests a decrease of the driving force for fET. The electronic coupling of flavin with the A171-T172 loop controlling Wat1 rearrangement and facilitating fET decreases in the mutant in comparison to WT (22 and 40 meV, respectively; Table S7), and at the same time, after rearrangement of Wat1

the coupling to the fatty acid remains moderate (8 meV in mutant and 47 meV in WT; table S7). Accordingly, fET in the mutant is limited by the weak interactions with the substrate, whereas wt fET is determined by flavin coupling to A171-T172. Using the semiclassical formula of Marcus theory, the five time smaller electronic coupling (40 meV in WT and 8 eV in C432S) together with the decrease of the driving force by 0.2 eV reduce the ET rate by a factor of 175 (assuming 1 eV reorganization energy). This estimate is in quantitative agreement with the experimentally observed reduction of the fET rate in the mutated protein. Hence, the computational analysis demonstrates that structural differences observed in the WT and mutated proteins are consistent with changes of fET in these proteins determined by transient spectroscopy experiments.

6.8. Excitation and redox energies of bent flavin

Our protein crystallography analysis demonstrates that the isoalloxazine ring of the flavin chromophore adapts a butterfly bent configuration in the dark state of *Cv*FAP, which is a manifestation of the steric and electronic interactions of the flavin with the surrounding protein. Previous computational results suggest that in general, flavin bending facilitates flavin reduction (*36*). In the case of FAP this indicates that bending stabilizes flavin radical anion against bET.

Table S9 presents our computational results addressing the effect of bending on photoinduced fET. To study the effect of bending qualitatively, we modeled the geometric effect of the steric interactions in a simplified flavin model fixing the torsions around the C-N bonds of the middle ring to 160 or 150 degree during geometry optimization (corresponding to butterfly bending of 20 or 30 degree, respectively). This simple model does not account for electronic interactions between the flavin and protein, which contribute in addition to the steric constraints.

To compensate for this limitation, we considered an active site (AS) model derived in the oxidized and radical state derived from geometries (1) and (3), respectively. Despite smaller 15-degree bending, the energy changes in the AS model (with respect to the panar flavin) are substantially larger in comparison to those in the simplified model with the 20- and 30- degree bending angle, suggesting that electronic interactions omitted in the simplified model significantly enhance the effect of the restrained torsion.

Figure S21 demonstrates changes of the flavin excitation energy, and vertical and adiabatic electron affinity. Notably, bending significantly decreases the oxidized-flavin excitation energy. Even to a larger extent, bending diminishes the vertical electron affinity which defines the CT energies in the flavin excitation spectrum. Hence, bending stabilizes the CT states with respect to the excited flavin facilitating fET.

6.9. Comparison of computational and experimental results

Computational results addressed the most prominent features of the FAP active site that were revealed by the high-resolution protein structures. These features include the oxidized flavin demonstrating a bent conformation of the isoalloxazine system, two water molecules interacting with the substrate and the R451 counterion of the fatty acid substrate and changes of the fatty-acid carboxyl interactions in the mutated proteins. The molecular interactions associated with these features were linked by the spectroscopic observations: the red-shifted UV-Vis absorption of the flavin chromophore, flavin fluorescence signal decay, changes of the flavin absorption accompanying the catalytic cycle, formation of CO_2 on the sub nanosecond time scale, back electron transfer coupled to proton transfer (PCET) suggested by the kinetic isotope effect.

Moreover, the calculations suggest a possible mechanism for bicarbonate formation and arginine deprotonation, which would be consistent with the FTIR spectral changes.

In particular, the computations predict bicarbonate formation involving either Wat1 or Wat2 that may follow splitting of Wat2 coupled to bET. In both identified PCET pathways (II and III in **Fig.6**), the hydroxyl derived from Wat2 is transiently formed at the bET step. This OH^- either deprotonates R451 or interacts with CO_2 yielding a bicarbonate. Such a partitioning reaction presumably leading to formation of the red-shifted species would be in line with the concomitant disappearance of the CO_2 signal with formation of the red-shifted species observed by time-resolved IR (**Fig. 2**). In contrast, the reaction involving Wat1 to form bicarbonate is likely a sequential process following bET, and thus, it occurs in the flavin red-shifted state. The reaction involves a re-protonation of R451 by Wat1 leading to bicarbonate formation. In order to be consistent with the spectroscopic data, bicarbonate formation involving Wat1 would have to occur on a similar time-scale as the disappearance of the CO_2 signal and formation of the red-shifted species, which implies a very short lifetime of the deprotonated R451. Consistent with a rather small energy barrier stabilizing the deprotonated R451 state, the FTIR signal assigned to arginine deprotonation was observed only at 100 K but not at 150 K.

While the sites of bicarbonate formation differ slightly for the partitioning reaction and sequential reaction, they are both close to the flavin and R451. In particular, hydrogen bonding with the protonated R451 is expected to stabilize the newly formed bicarbonate in either case. It is thus rather surprising that no electron density features consistent with bicarbonate were observed close to FAD and R451 in the cryocrystallography (**Fig. 4D**) or TR-SFX (**Fig. 5A**) data of illuminated crystals. Instead, electron density consistent with bicarbonate was observed very close to C432. This would imply that bicarbonate diffused there shortly after its formation, but

the driving force for this process is unclear. Alternatively, bicarbonate might actually be formed close to C432 which would suggest that C432 has a catalytic role, e.g. involved in a hydrogen atom transfer (HAT). In this case, the formed C432 radical would then be reduced by bET from $FAD^{\bullet-}$, resulting in a red-shifted oxidized flavin FAD_{RS} in ~100 ns. However, to be consistent with the absence of cysteine deprotonation in the FAD_{RS} form as assessed by cryotrapping FTIR (**Fig. 4A**), this bET would have to be coupled to protonation of the C432 anion (within the ~100 ns phase). Furthermore, the acceleration of bET/red shift formation in the R451K mutant occurring in spite of the unfavorable orientation of the C432 side chain for HAT to the alkyl radical and bET from $FAD^{\bullet-}$ in this mutant, would argue against a catalytic role of C432 in the FAP photocycle.

The fate of the bicarbonate pool and possible transformation of bicarbonate back to CO_2. remains unclear. Transformation of CO_2 to HCO_3^- involving either Wat1 or Wat2 lowers the energy. Therefore, reverse reactions – proton transfer from R451 to bicarbonate to recover Wat1 or Wat2 and CO_2 – are ruled out because of their unfavorable energy. If HCO_3^- escapes from the protein as such, it should not turn into CO_2 in solution given the experimental pH of 8.2 (and certainly not on the microsecond/millisecond time scale). Back transformation of HCO_3^- to H_2O + CO_2 is hence more likely initiated within the protein by a residue other than R451. This process is subject to future investigations.

Supplementary Figures

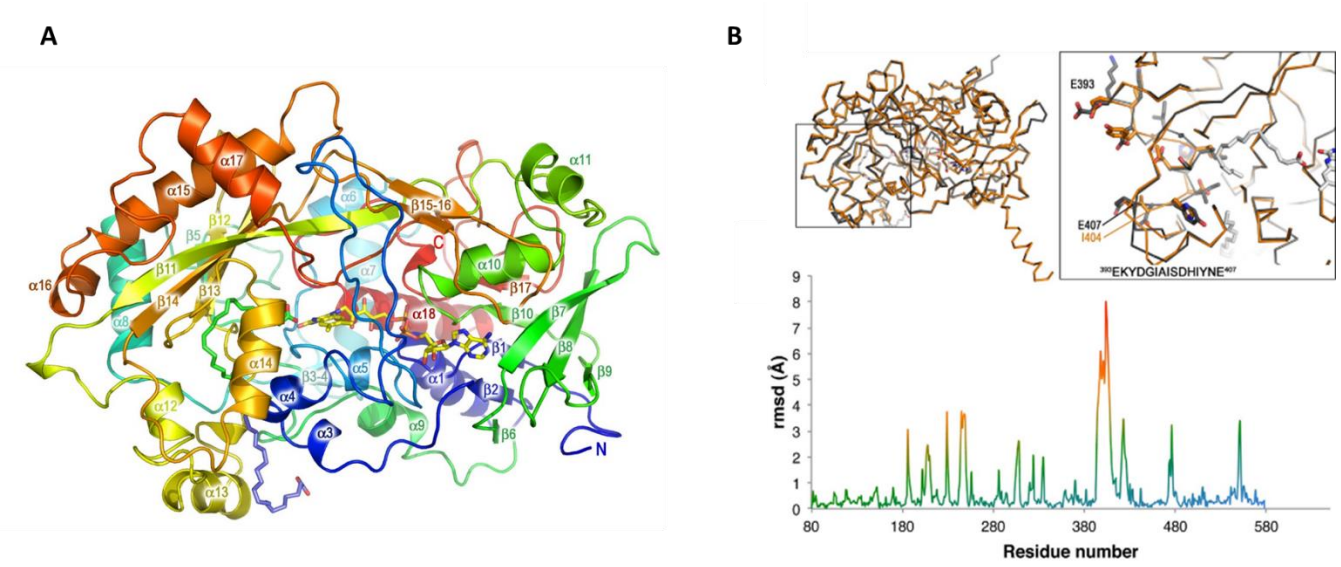

Fig. S1: High-resolution synchrotron structure (1.8Å) of *Cv*FAP.

(**A**) Overall structure of *Chlorella variabilis* FAP (*Cv*FAP) in the dark ('100 K dark') showing the numbered secondary structure elements. (**B**) Structural comparison between medium- (4) and high-resolution structures of *Cv*FAP (present study). Upper panel: the medium-resolution structure (featuring an N-terminal tail, residues 61 to 76) is shown in gold and the high-resolution one (no N-terminal tail) is shown in silver. Inset: magnification of the region that appeared to be poorly structured in the medium-resolution structure (residues 392 to 407). Lower panel: average distance between the Cα atoms of the two superimposed structures as shown by the root-mean-square deviation of atomic positions.

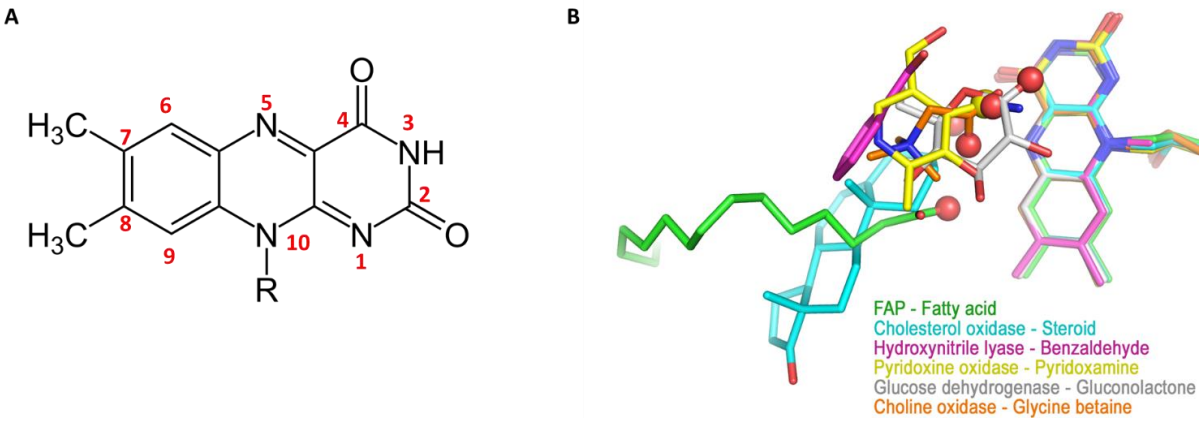

Fig. S2: Isoalloxazine ring of FAD.

(**A**) Numbering of the atoms in the isoalloxazine ring of FAD. (**B**) Comparison of substrate or product position relative to FAD isoalloxazine ring in GMC oxidoreductase family of enzymes. FAD cofactors are shown as sticks on the right . Substrates or products are also shown as sticks, with their closest atom involved in the catalytic reaction shown as a sphere. Except for FAP, all the major GMC stabilize their substrate close to the central N5 atom of FAD. PDB used are 1COY (Cholesterol oxidase), 3GDN (Hydroxynitrile lyase), 4HA6 (Pyridoxine oxidase), 4YNU (Glucose dehydrogenase) and 4MJW (Choline oxidase). The shortest distance between the carboxyl group and the benzene ring plane of the flavin is 3.1 Å and the angle between them is below 35°, indicative of an anion-quadrupole interaction (*118*). To our knowledge, it is the first clear structural characterization of such a feature in enzyme substrate interaction, with two other putative examples in chloride transport (*119*, *120*).

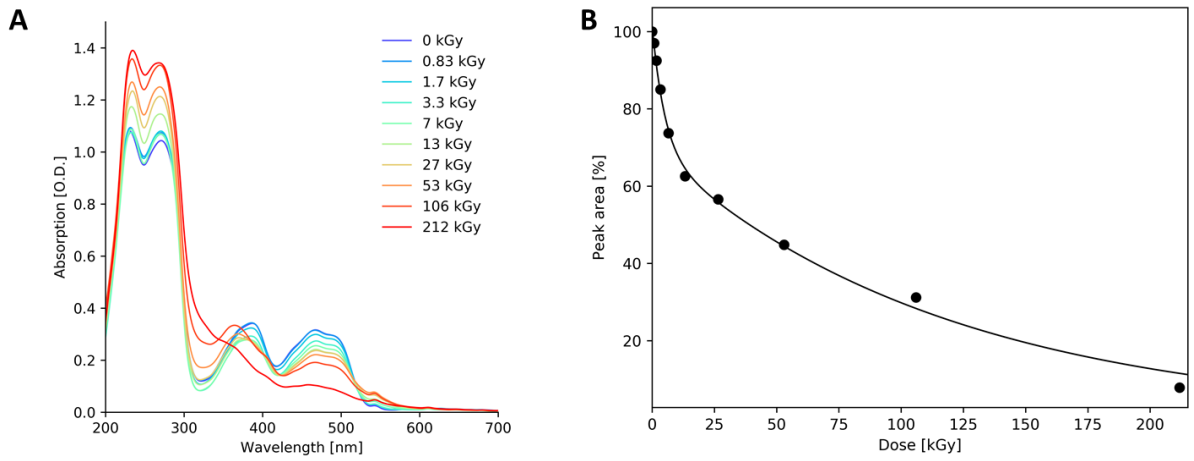

Fig. S3: X-ray dose-resolved UV-Vis absorption spectra of a *Cv*FAP crystal at room temperature.

(**A**) Series of UV-Vis absorption spectra recorded at room temperature on a FAP crystal with increasing X-ray doses showing the progressive reduction of the FAD. (**B**) Decay curve of the area of the FAD absorption peak between 410 and 540 nm (black circles) and an exponential fit (black curve) indicating a reduction half-dose of ~40 kGy.

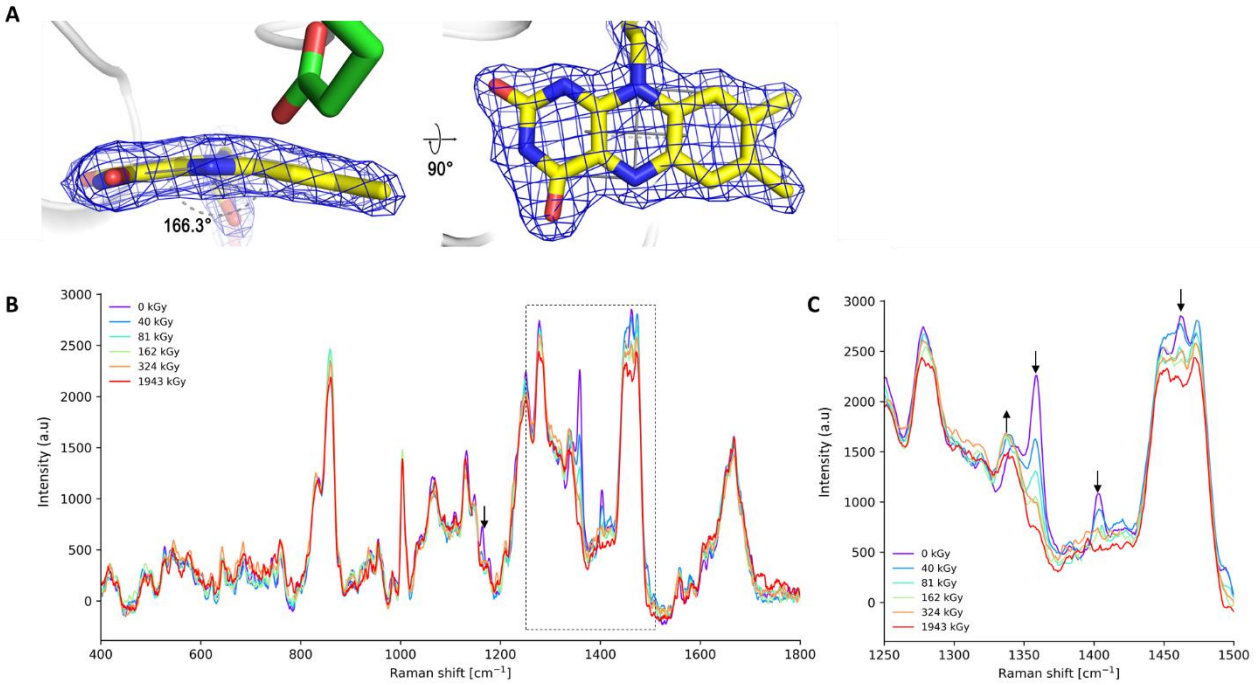

Fig. S4: Low dose structure at room temperature and X-ray dose-resolved Raman spectra series of a *Cv*FAP crystal at 100 K.

(**A**) 'RT dark low-dose' FAP structure depicting a bent FAD. The dihedral angle (C4-N5-N10-C9) is indicated and the $2F_o - F_c$ map is contoured at 2.5 σ. (**B**) Series of non-resonant Raman spectra recorded at 100 K on a FAP crystal cryoprotected with 20% glycerol with increasing X-ray doses. (**C**) Close-up on the region showing the decrease, or increase of FAD Raman modes due to X-ray induced reduction. The spectra do not show the global collapse of peak intensity for the Raman modes of FAD that is expected for the X-ray induced butterfly movement (*26*), and only a few stretching modes are affected (indicated by arrows), which can be explained by the change in redox state of FAD without a significant structural change.

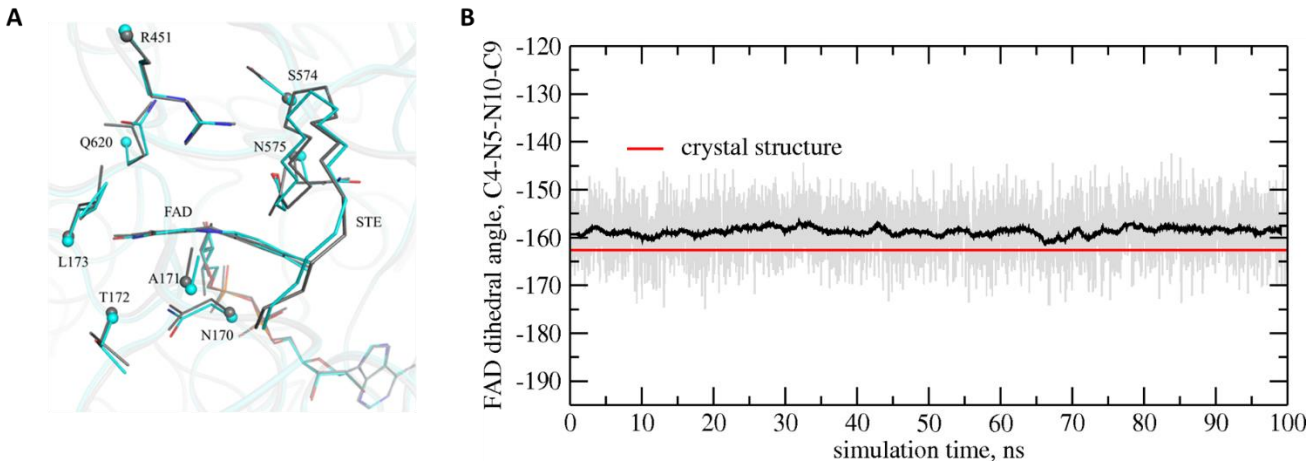

Fig. S5: Flavin dihedral angle observed in Molecular Dynamics simulations.

(**A**) Superposition of the crystal structure (synchrotron dark structure) around FAD and an average structure observed in Molecular Dynamics (MD) simulations. The experimental structure is shown in gray and the averaged MD structure is in color. The bent conformation of flavin is clearly visible. (**B**) The black line shows average fluctuations of the dihedral angle C4-N5-N10-C9 of the oxidized FAD observed in MD simulations and the black line shows the dihedral angle of the oxidized FAD in the crystal structure (synchrotron dark structure).

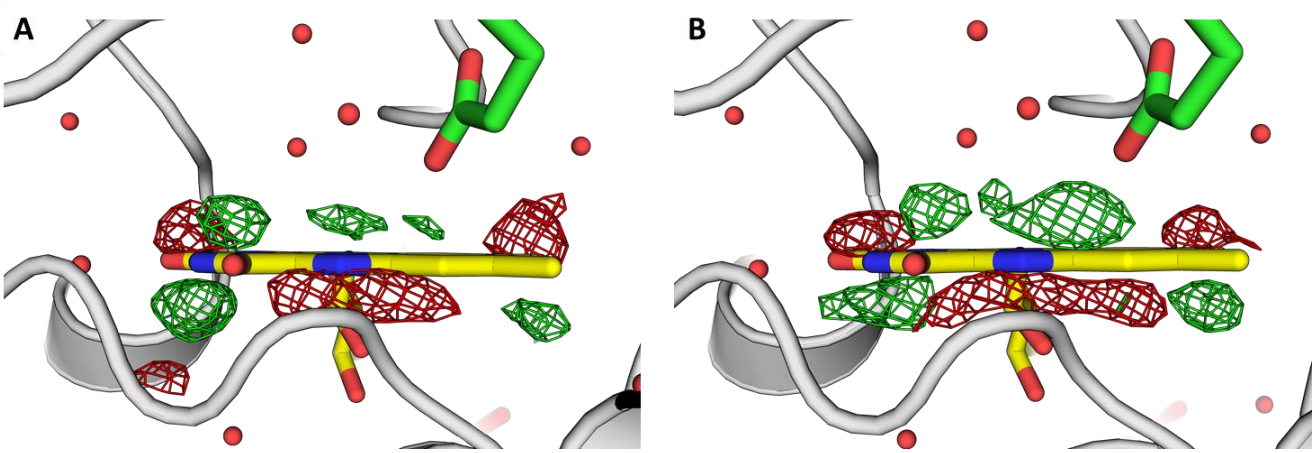

Fig. S6: Residual $mF_{obs} - DF_{calc}$ peaks indicate isoalloxazine rings of the FAD cofactor are not planar in the SFX dark-state structure.

When the isoalloxazine ring of the FAD cofactor (yellow stick model) are restrained to be planar in the SFX structure ((***A***) molecule A, (***B***) molecule B), peaks in the $mF_{obs} - DF_{calc}$ map (+3 σ and –3 σ in green and red, respectively) indicate bending. The fatty acid is shown in green, the protein moiety in grey.

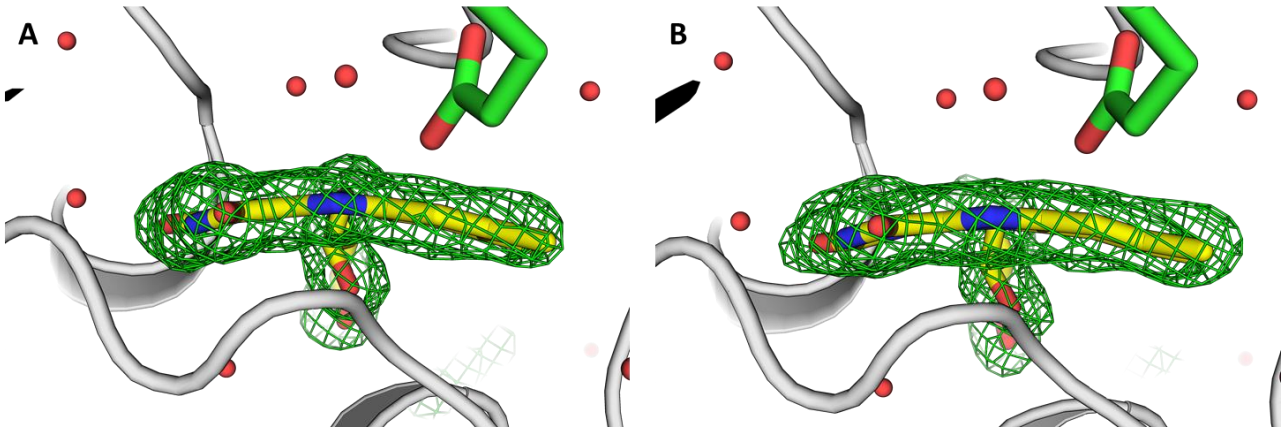

Fig. S7: FAD bending in the SFX dark-state structure.

The $mF_{obs} - DF_{calc}$ omit map (3 σ, green) indicates bending of the isoalloxazine ring of the FAD cofactor (dark-blue stick model) in molecules A (***A***) and B (***B***) . The bending angle is 14.3° and 11.7° in molecule A and B, respectively. The fatty acid is shown in green, the protein moiety in grey.

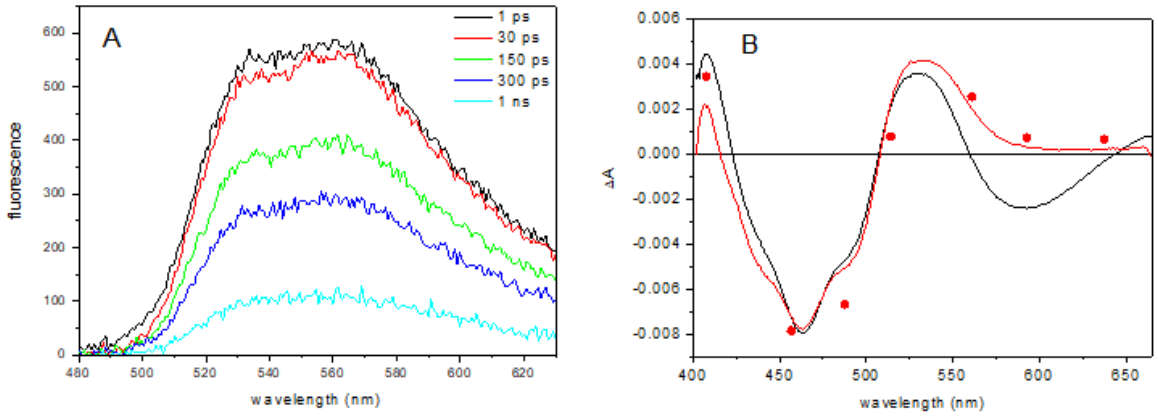

Fig. S8: Ultrafast fluorescence and visible absorption spectroscopy on *Cv*FAP in solution in the presence of substrate.

(**A**) Fluorescence spectra at different delay times, highlighting dominant decay on the 300-ps timescale. The corresponding kinetics are shown in **Fig. 2A**. Upon long exposure of the sample to light and higher excitation densities the decay slows down (not shown), reflecting substrate depletion. **(B)** Global analysis of the transient absorption data corresponding to **Fig. 2B** in terms of a 350 ps phase (close to the time constant found for fluorescence decay rise of the CO_2 signal in the mid-IR) and a long-lived phase. The spectra associated with the initial state (black line, FAD* – FAD_{OX}) and the final state (red line) emerging from the analysis are shown. The spectrum of the final state is in close agreement with the initial spectrum (red points, 10 ns) from single flash absorption experiments *(4)* assigned to $FAD^{\bullet-}$ – FAD_{OX}. As no further phases were observed, this implies that electron transfer from the substrate to FAD occurs concomitant with FAD* decay in ~300 ps. In passing we mention that the present full spectral characterization allows to assess a significant difference in the 500-550 nm region in the final spectrum with a model spectrum based on the $FAD^{\bullet-}$ spectrum of glucose oxidase (*4*) suggesting that $FAD^{\bullet-}$ absorbs stronger in the red part of the spectrum in FAP.

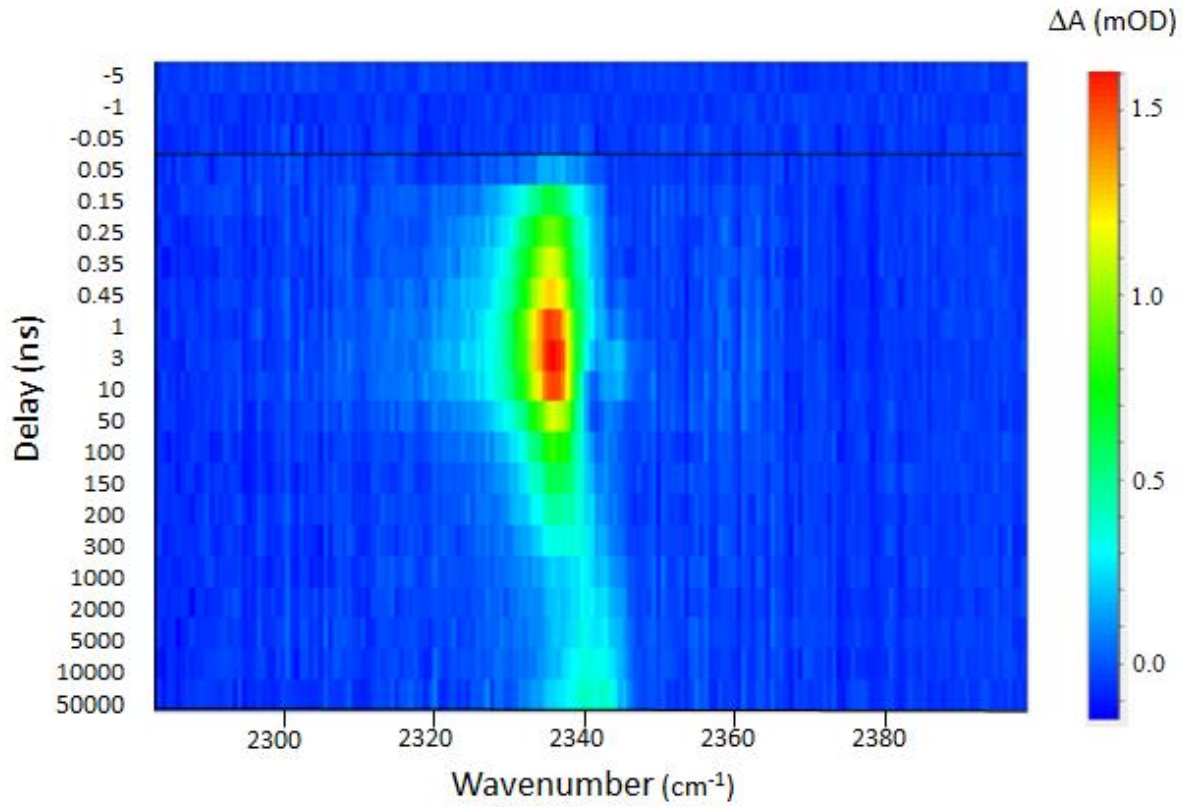

Fig. S9: Formation of CO_2 co-product studied by TR-IR.

False-color representation of time-resolved IR data corresponding to **Fig. 2C** highlights shifting to the value of CO_2 in solution in a few µs.

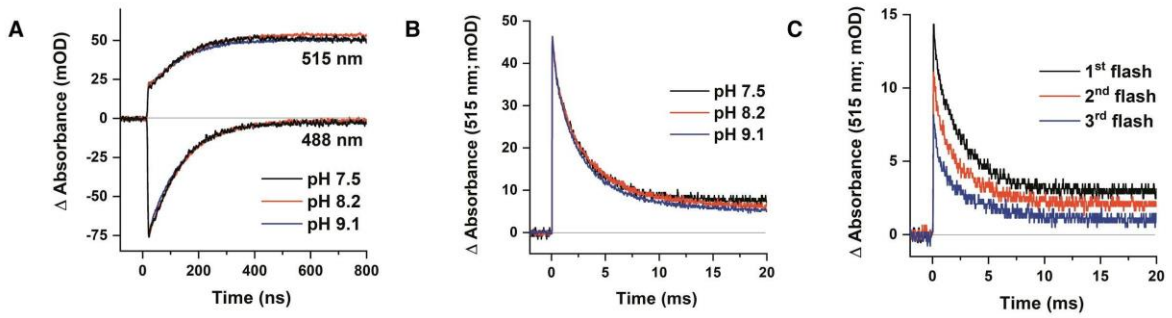

Fig. S10: Effects of pH and substrate consumption on the transient FAD absorption changes in WT *Cv*FAP.

(**A**) FAD transient absorption changes on the sub-microsecond timescale at different pH values. Signals at 488 nm shows absorption bleaching due to FAD reduction to $FAD^{\bullet-}$, followed by its back reoxidation; signals at 515 nm reflect formation of the red-shifted reoxidized FAD (FAD_{RS}). (**B**) Reversion of the transient FAD red shift at different pH values monitored at 515 nm on the millisecond timescale. (**C**) Effect of the native substrate(s) consumption (by saturating laser flashes at 470 nm) on the disappearance of the transient FAD red shift monitored at 515 nm.

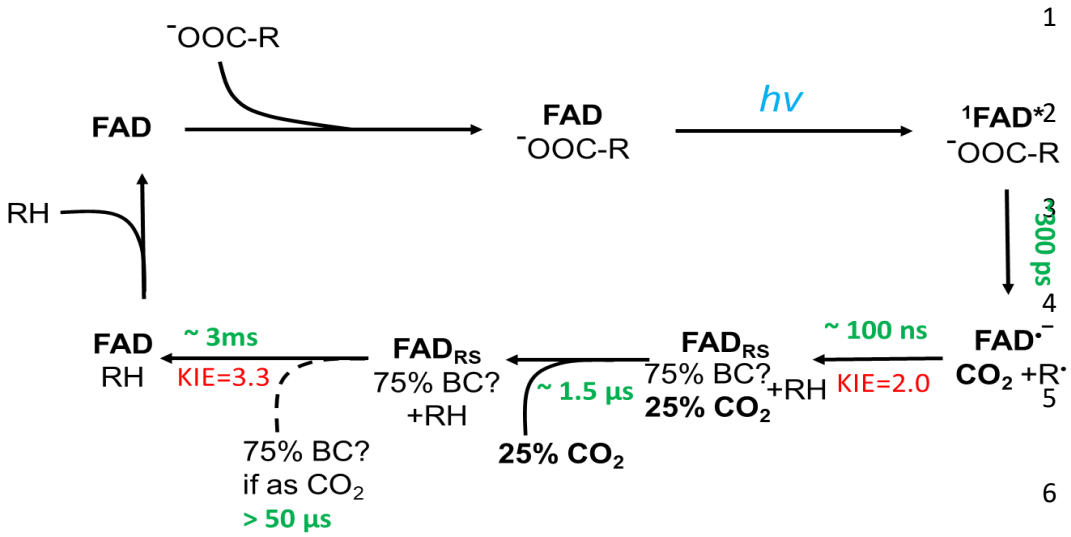

Fig. S11: Summary of the results obtained on *Cv*FAP using time-resolved infrared and UV-Visible spectroscopies.

Spectroscopy shows that light-induced formation of a flavin radical $FAD^{\bullet-}$ occurs with a time constant $\tau \sim 300$ ps, concomitant with decarboxylation of the deprotonated fatty acid substrate $^{-}$OOC-R. Back electron transfer occurs with $\tau \sim 100$ ns, resulting in FAD_{RS}, reoxidized FAD displaying a transiently red-shifted absorption spectrum. The pronounced kinetic isotope effect ($KIE \approx 2$) of this process suggests that it is coupled to a proton or hydrogen atom transfer to the alkyl radical. On the same time scale, a major fraction of the formed CO_2 is transformed to a species believed to be bicarbonate (BC), which is supported by complementing cryotrapping FTIR spectroscopy and possibly X-ray crystallography. During the subsequent process ($\tau \sim 1.5$ µs) the remaining CO_2 changes towards an environment spectroscopically identical to aqueous solution. The TR-IR CO_2 signal lost during the ~100 ns may recover on a timescale beyond 50 µs, the time window of the experiment. FAD_{RS} decays to the initial state with $\tau \sim 3$ ms, the second process in the photocycle displaying an isotope effect ($KIE \approx 3$). Species in bold were directly observed by time-resolved spectroscopy.

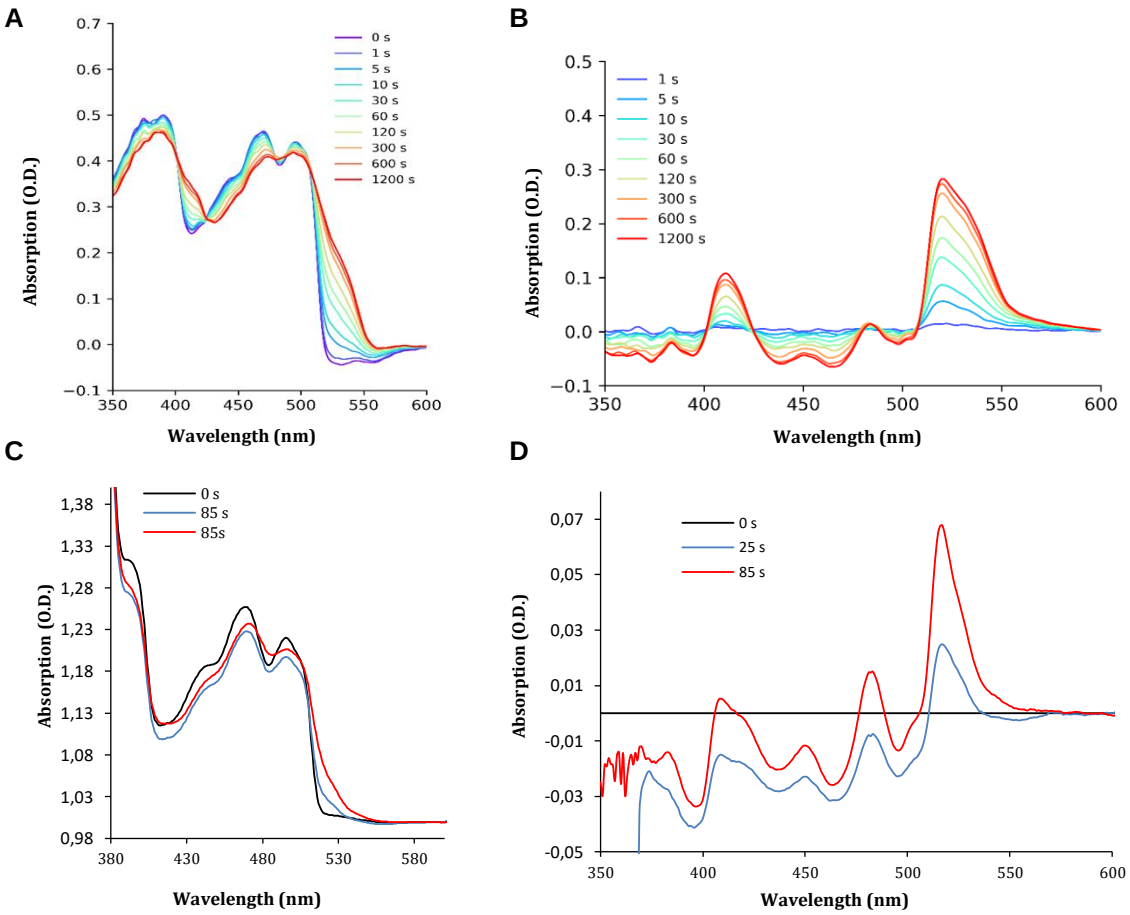

<u>Fig. S12: Absorption spectra of the red-shifted intermediate in *Cv*FAP crystals and solution.</u>

(**A**) Series of UV-Vis absorption spectra recorded at 100 K on a FAP crystal cryoprotected with 20% glycerol with increasing irradiation times from a 470 nm LED. (**B**) Series of corresponding difference spectra [spectrum (*t*) – spectrum (t_0)]. (**C**) Series of UV-Vis absorption spectra recorded at 100 K on a solution of FAP with increasing irradiation times from a 470 nm LED. (**D**) Series of corresponding difference spectra [spectrum (*t*) – spectrum (t_0)].

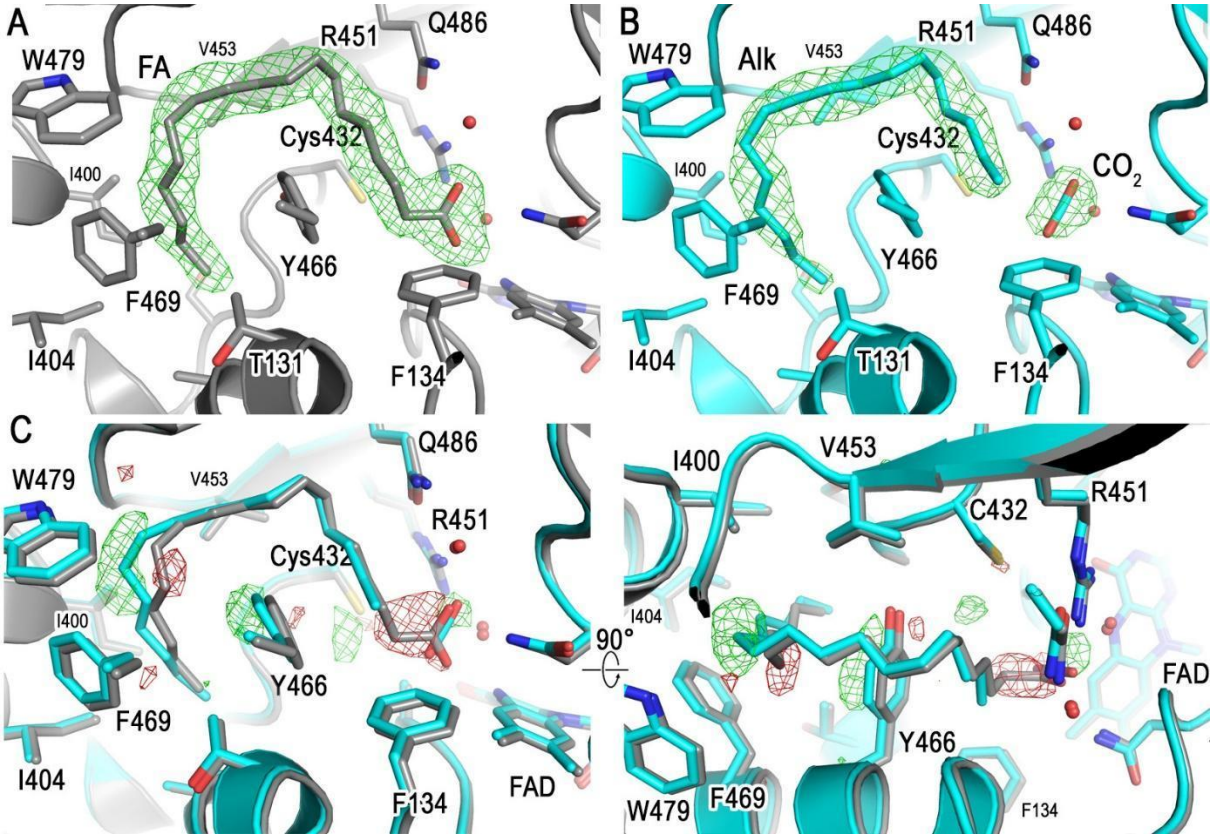

Fig. S13: Characterization of the red-shifted intermediate in *Cv*FAP crystals.

Structures were obtained from data collected from crystals kept at cryogenic temperature using synchrotron radiation ('100 K light' and '100 K dark'). (**A**) Omit map around the active site substrate in the dark and (**B**) after blue light illumination. (**C**) Experimental difference ($F_{light} - F_{dark}$) map at 100 K contoured at +/– 4σ and centered on the active site substrate, superposed on the refined structures of the dark state (gray) and the red-shifted form (cyan). The cleavage of the C1-C2 bond is clearly visible, together with the recoil of the alkane product toward the exterior along the substrate tunnel, and a rotation of the side chain of Y466 that accompanies this recoil.

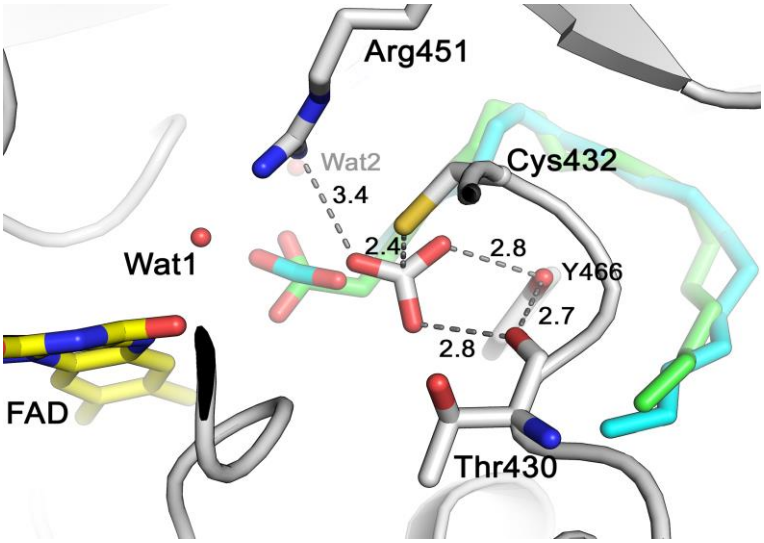

Fig. S14: Environment of the bicarbonate modelled in the electron density next to C432 in the 150 K pH 8.5 structure ('150 K light').

The environment of the bicarbonate, with putative H-bonds and contacts, is shown. The electron density omit map is shown in **Fig. 3D**.

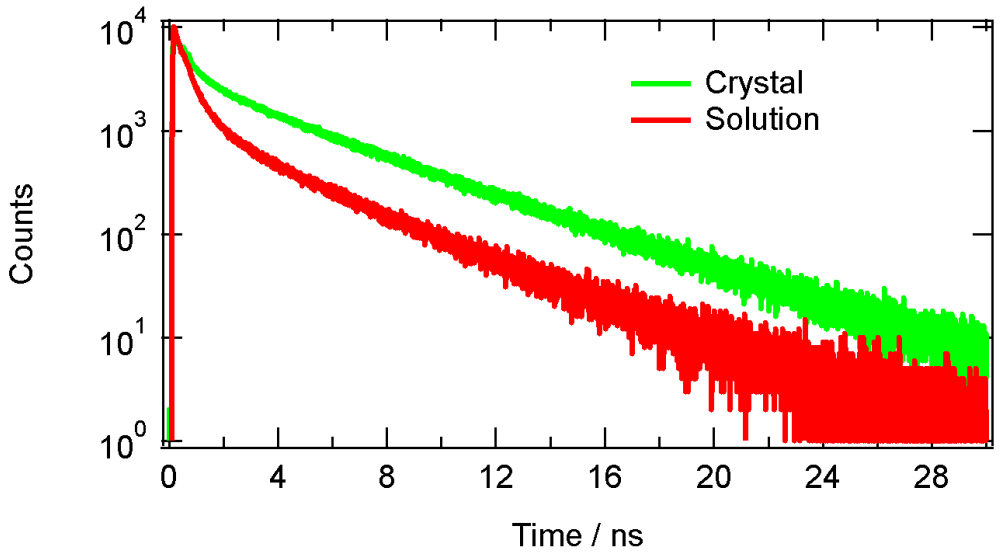

Fig. S15: Fluorescence decays measured using single photon counting technique.

Decays were measured at 560 nm after a 400 nm excitation of FAP in solution (50 mM Tris pH 8.5, 100 mM NaCl) and in microcrystals (in 19% (w/v) PEG 4000, 0.1 M Na citrate pH 5.5, 0.01 M spermidine).

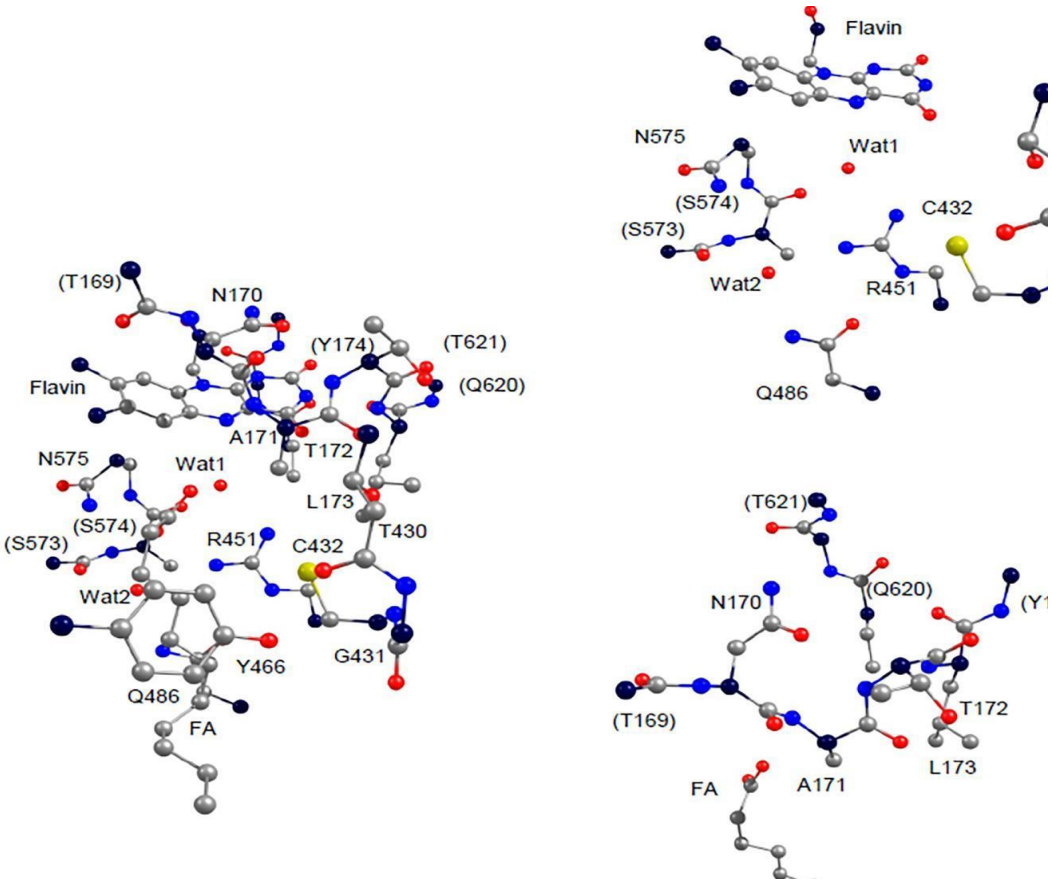

Fig. S16: Model of the *Cv*FAP active site.

Model of the active site (272 atoms, net charge 0) employed in pathway calculations to obtain the geometries listed in table S5. The hydrogen atoms are not shown. Atoms fixed during geometry optimization are indicated in black. Flavin, fatty acid (FA), water molecules (Wat) and residues are labeled. The residues whose side chain was not included in the model are indicated in brackets. The model consists of the following fragments: flavin, fatty acid (deprotonated), Wat1, Wat2, polypeptide fragments (T169)-N170-A171-T172-L173-(Y174), T430-G431-C432, (S573)-(S574)-N575, (Q620)-(T621), and side chains R451 (protonated), Y466 , Q486. On the right-hand side, we show the same model split in two parts for better clarity.

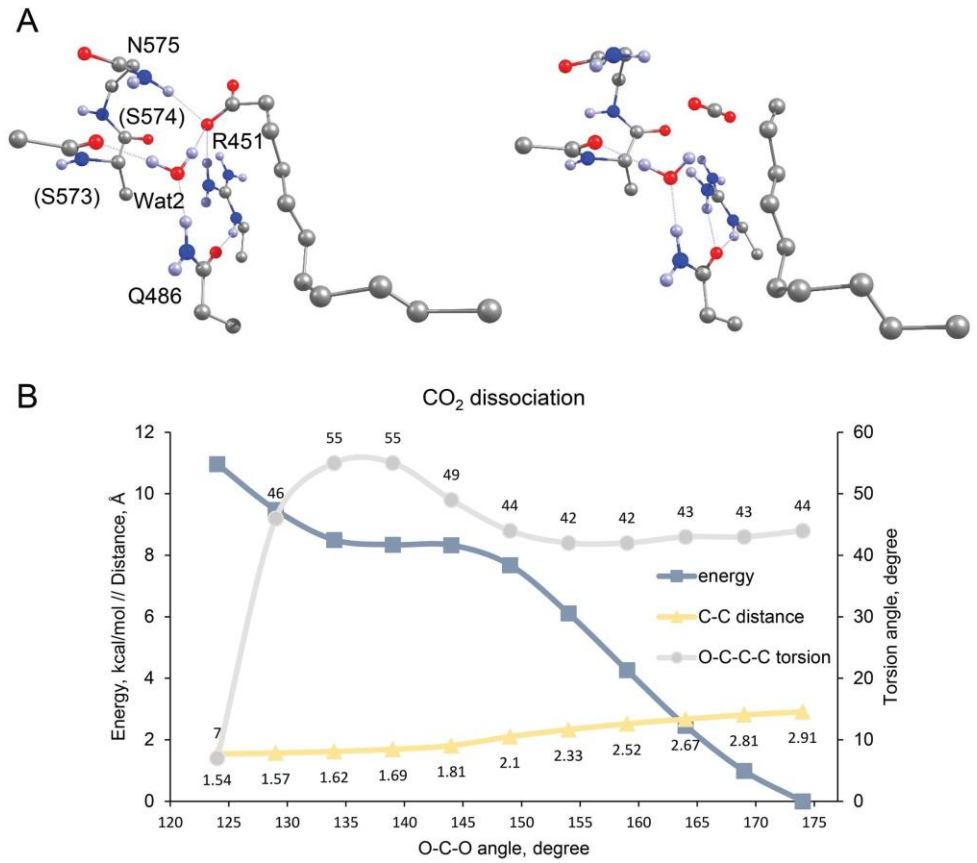

Fig. S17: Fatty acid decarboxylation in the charge-transfer (radical) state.

(**A**) The initial and final geometries of the relaxed energy scan in the radical state. A truncated model (94 atoms, net charge 1) was employed in the calculations. The hydrogen atoms bound to the carbon atoms are omitted for clarity. (**B**) The relaxed energy scan results. The initial geometry was first optimized in the FA anionic state (R-B3LYP/cc-pvdz); after constraining the OCO angle, geometry optimization was continued in the radical state (U-B3LYP/cc-pvdz). All observed changes are triggered by increasing the OCO angle. Relative energy (blue), distance corresponding to the dissociating C-C bond (yellow) and CO_2 rotation angle (grey) are shown for all partially optimized geometry with the OCO angle fixed at the indicated value.

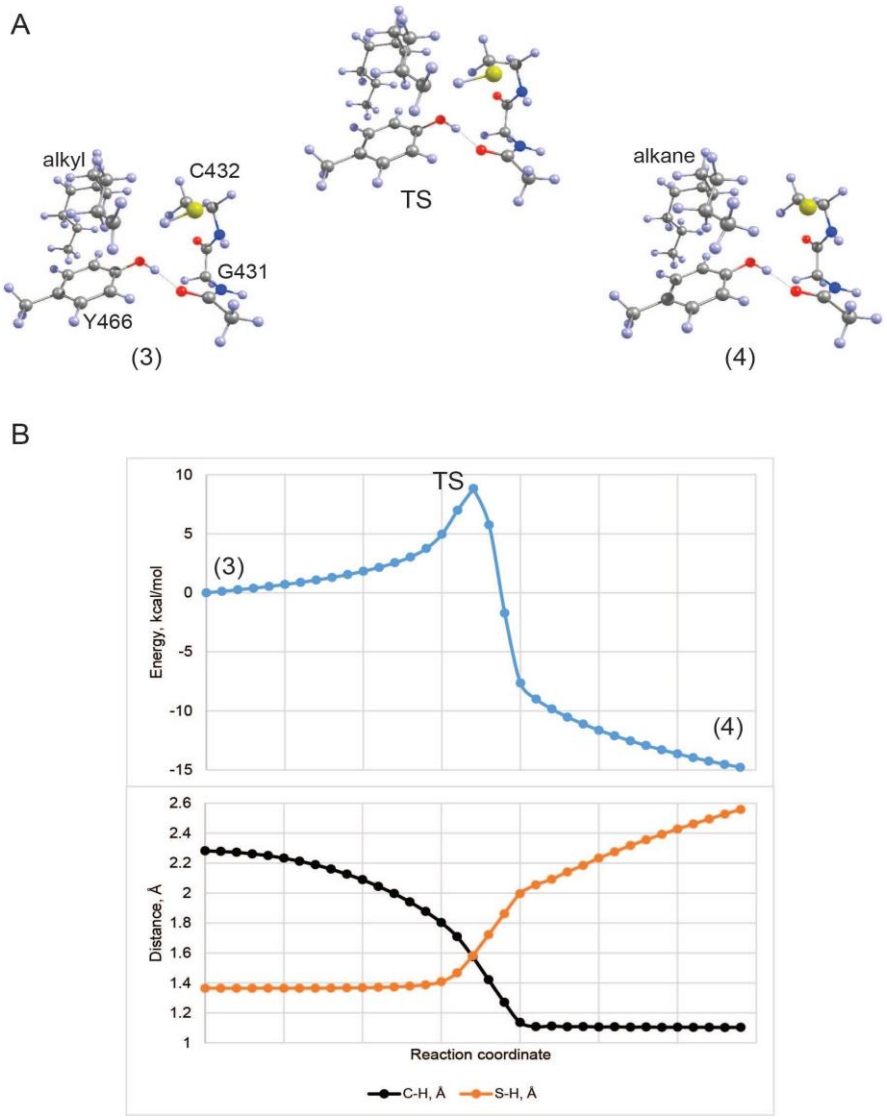

Fig. S18: Energy and transition state of HAT reaction.

(**A**) The initial (3), final (4) and transition state (TS) geometries describing the HAT reaction. Calculations performed for a truncated model shown in the panel (70 atoms, net charge 0) in the radical state, using U-B3LYP/cc-pvdz. The imaginary frequency (1470i cm^{-1}) mode corresponds to a coupled C-H and H-S stretch. (**B**) The energy and geometry changes obtained from the intrinsic reaction coordinate (irc) calculations starting from the saddle point geometry (TS) toward (3) and (4).

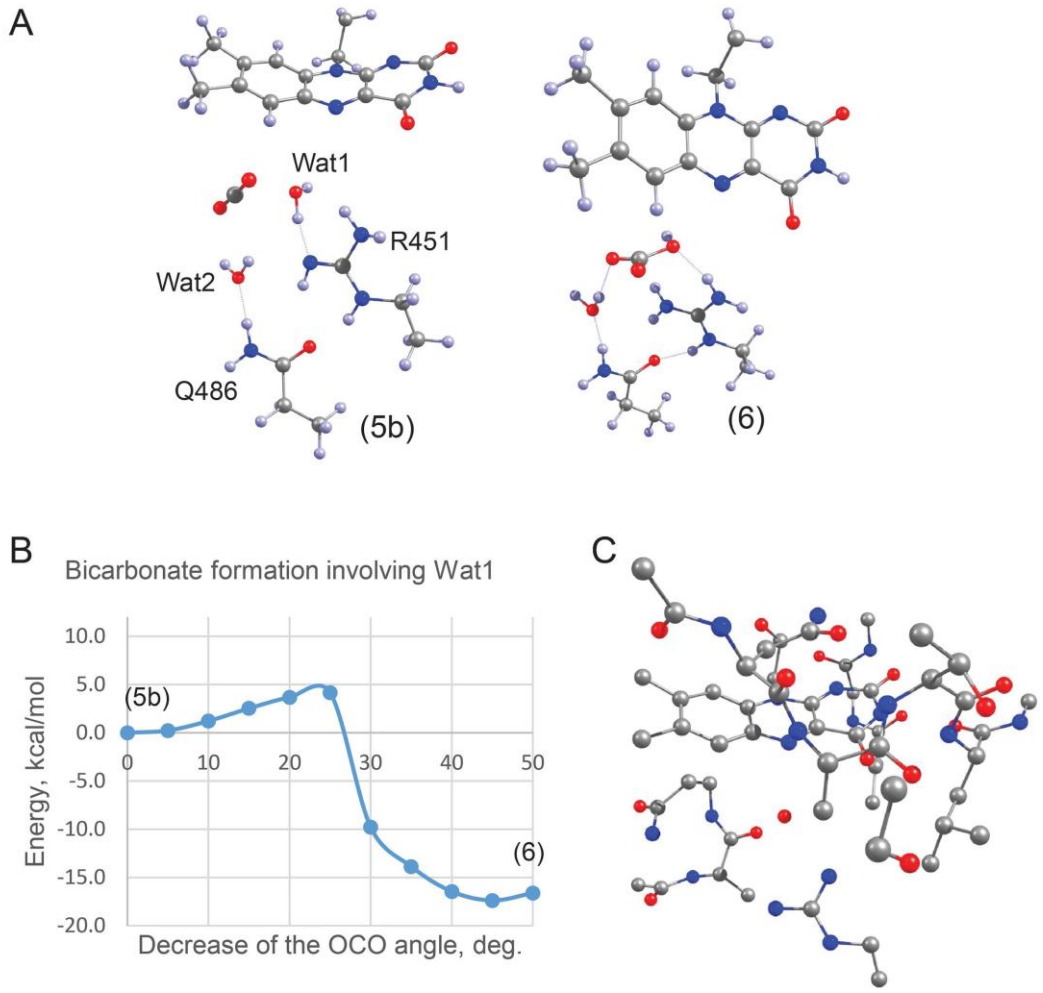

Fig. S19: Bicarbonate formation from CO_2 and Wat1.

(**A**) Bicarbonate formation from Wat1 and carbon dioxide catalyzed by R451 in FAP. Fragments of the model are shown to detail structural changes due to carbon dioxide-bicarbonate conversion. (**B**) Energies of bicarbonate formation computed with R-B3LYP/cc-pvdz. The relaxed-scan energy calculations were performed along the OCO bending coordinate of carbon dioxide. (**C**) Truncated active site model employed in the relaxed scan computations addressing bicarbonate formation from Wat1. The hydrogen atoms are omitted for clarity.

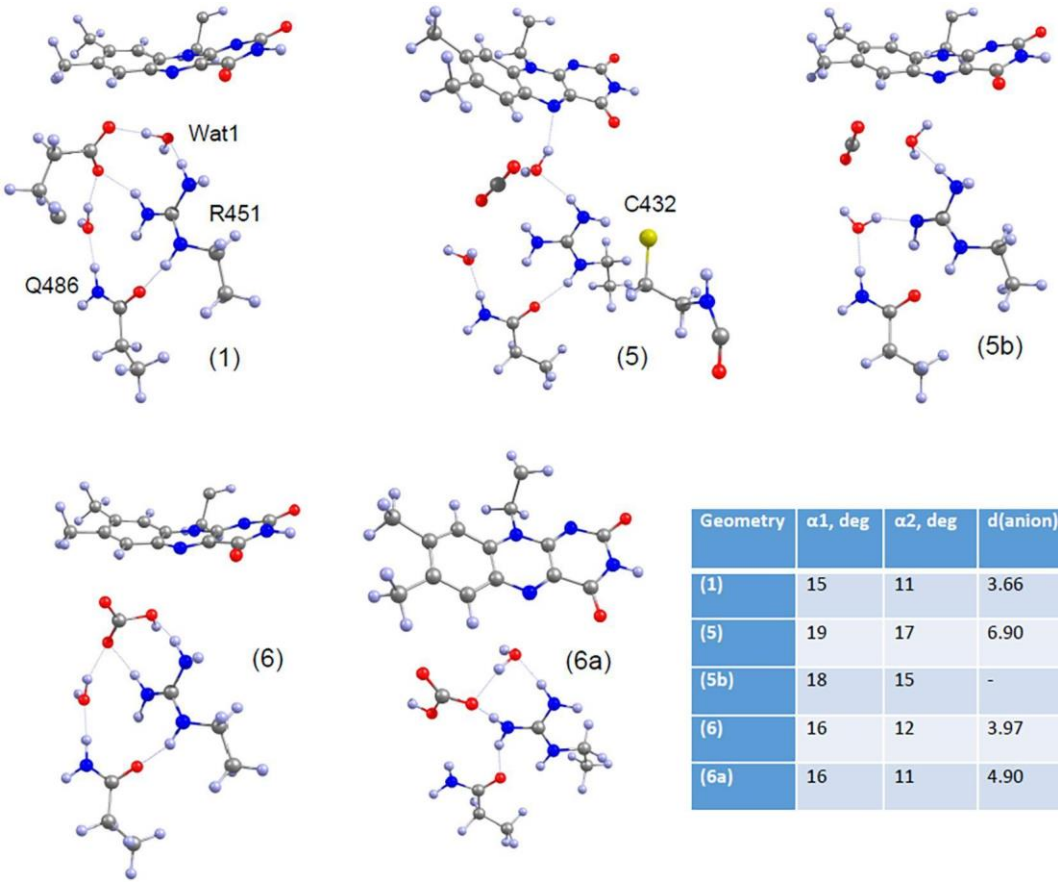

Geometry	α1, deg	α2, deg	d(anion), Å	d(Wat1), Å
(1)	15	11	3.66	2.77
(5)	19	17	6.90	2.92
(5b)	18	15	-	2.97
(6)	16	12	3.97	3.01 (OH)
(6a)	16	11	4.90	5.18

Fig. S20: Suggested red-shifted FAD_{RS} intermediates.

Flavin bending is defined by angles α1(C9N10N5C4) and α2(C6N5N10N1); d(anion) is the shortest distance from flavin N5 to the anionic species (R-CO_2^-, HCO_3^- and $C432^-$); d(Wat1) is the distance from favin N5 to Wat1 oxygen.

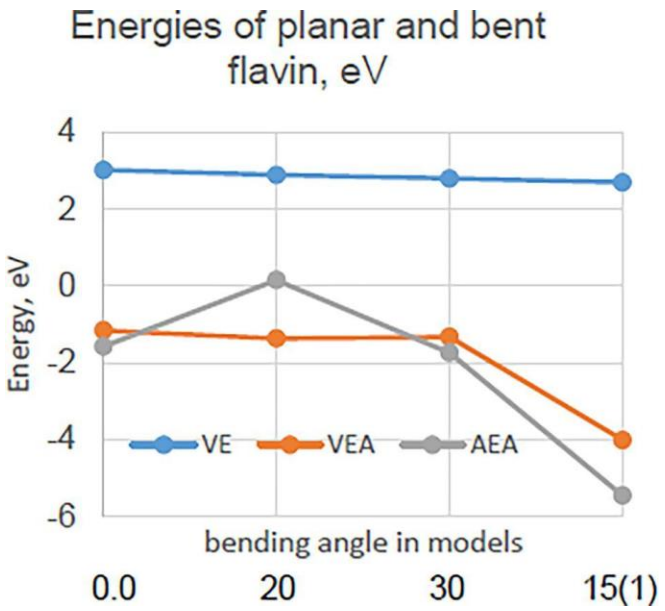

Fig. S21: Flavin butterfly bending energies.

The energies compared in this figure are listed in table S9. The negative vertical electron affinity (VEA) and adiabatic electron affinity (AEA) energies indicate that flavin semiquinone has a lower energy (electronically more stable) than the oxidised state. Flavin bending decreases the vertical excitation (VE) energy. The decrease of the AEA value indicates stabilization of flavin semiquinone against re-oxidation. At a 15-degree bent geometry and in the active-site model (1) (bending angle 15(1) in the figure), the VEA value decreases to a larger extent than VE energy (in comparison to the planar geometry), indicating stabilization of CT states (flavin semiquinone) and hence, favoring fET. Notably, the effect of bending is enhanced by intermolecular interactions in the FAP active-site model (1). Hence, flavin bending (along with intermolecular interactions) red-shifts the absorbance of the oxidized flavin and facilitates fET.

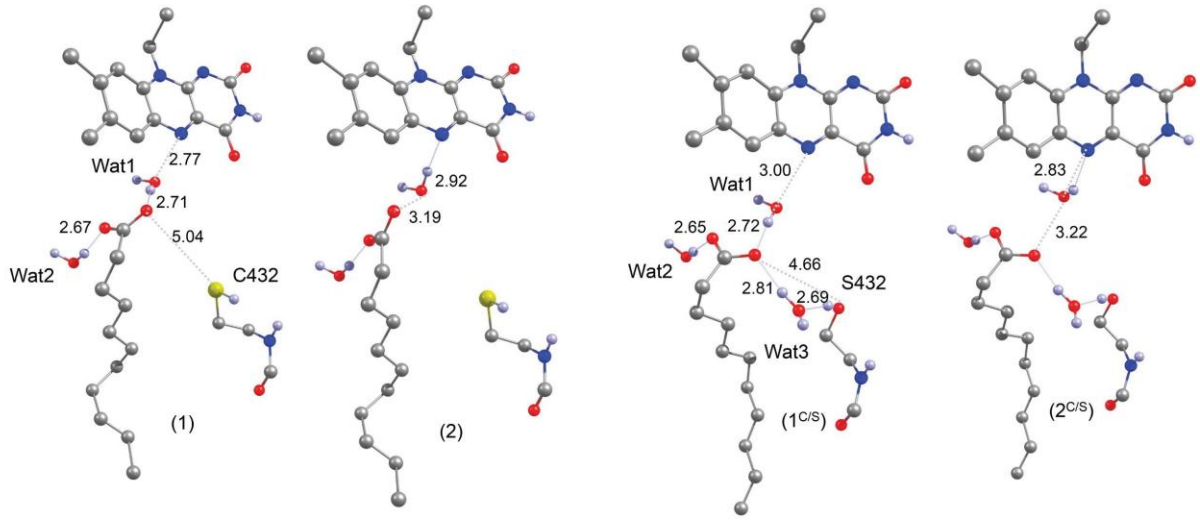

Fig. S22: Interaction of the fatty acid carboxylate with water molecules in wild type and C432S models.

Distances (Å) characterize interactions of the fatty acid substrate with the active-site water molecules.

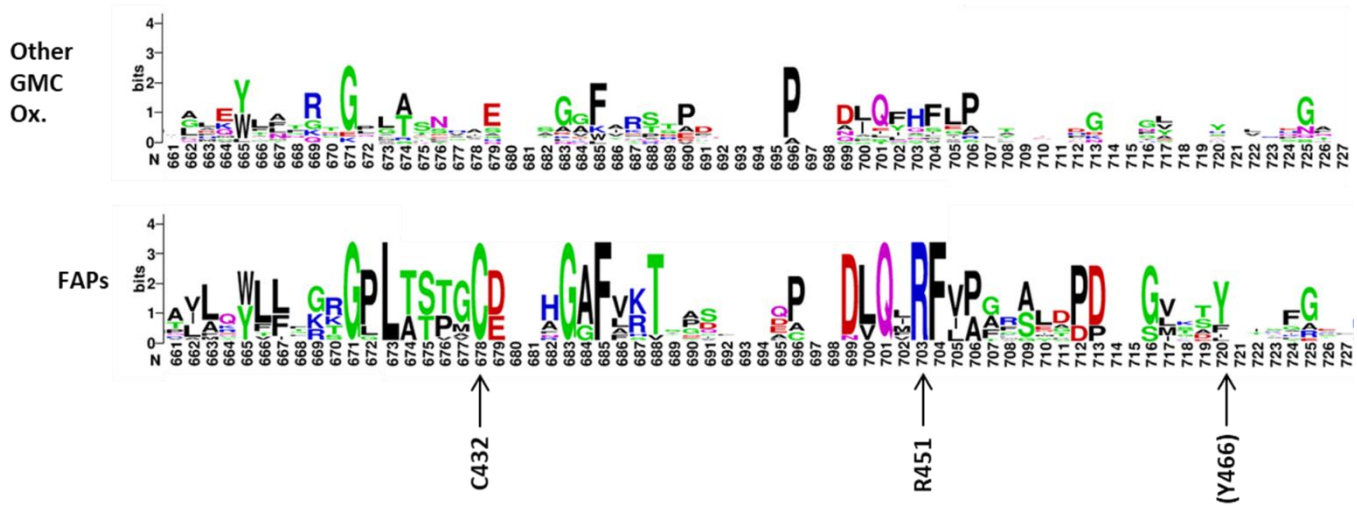

Fig. S23: Conservation of residues specific to FAPs within the active site of the GMC oxidoreductases.

Protein sequences of 14 FAPs and 16 other GMC oxidoreductases (table S4) were aligned and a sequence logo generated. Only the part of the sequence logo featuring the possible proton donors to the alkyl radical is shown (C432, R451, Y466 in *Cv*FAP). Letters represent amino acids at successive positions in the multiple alignment. The overall height of the stack indicates the sequence conservation at that position, while the height of symbols within the stack indicates the relative frequency of each amino acid at that position. The sequence logo highlights that C432 and R451 are 100% and specifically conserved in FAPs .

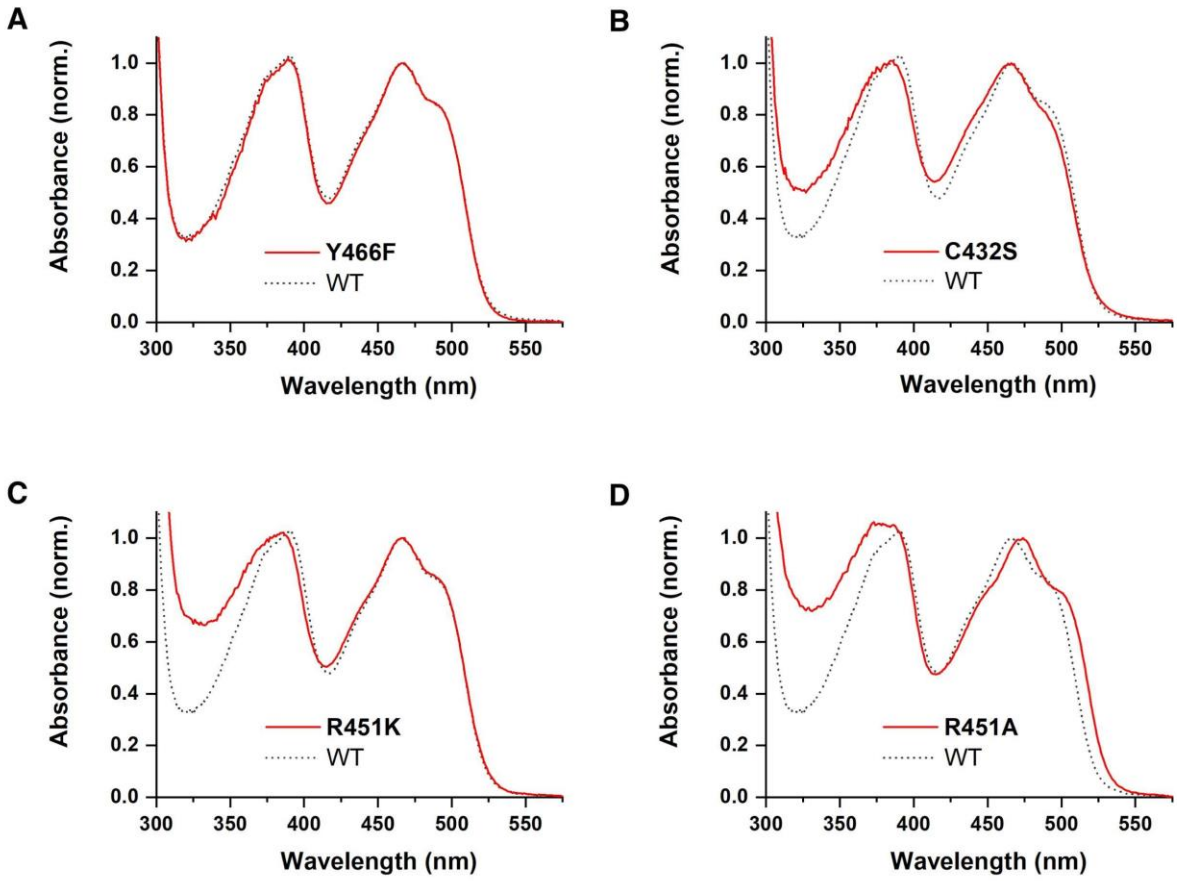

Fig S24: UV-Vis spectra of WT and mutant *Cv*FAP.

UV-Vis spectra of Y466F (A), C432S (B), R451K (C) and R451A (D) mutants compared to WT. The absorption maximum in the C432S mutant is 2 nm blue-shifted and that of R451A is 9 nm red-shifted compared to WT.

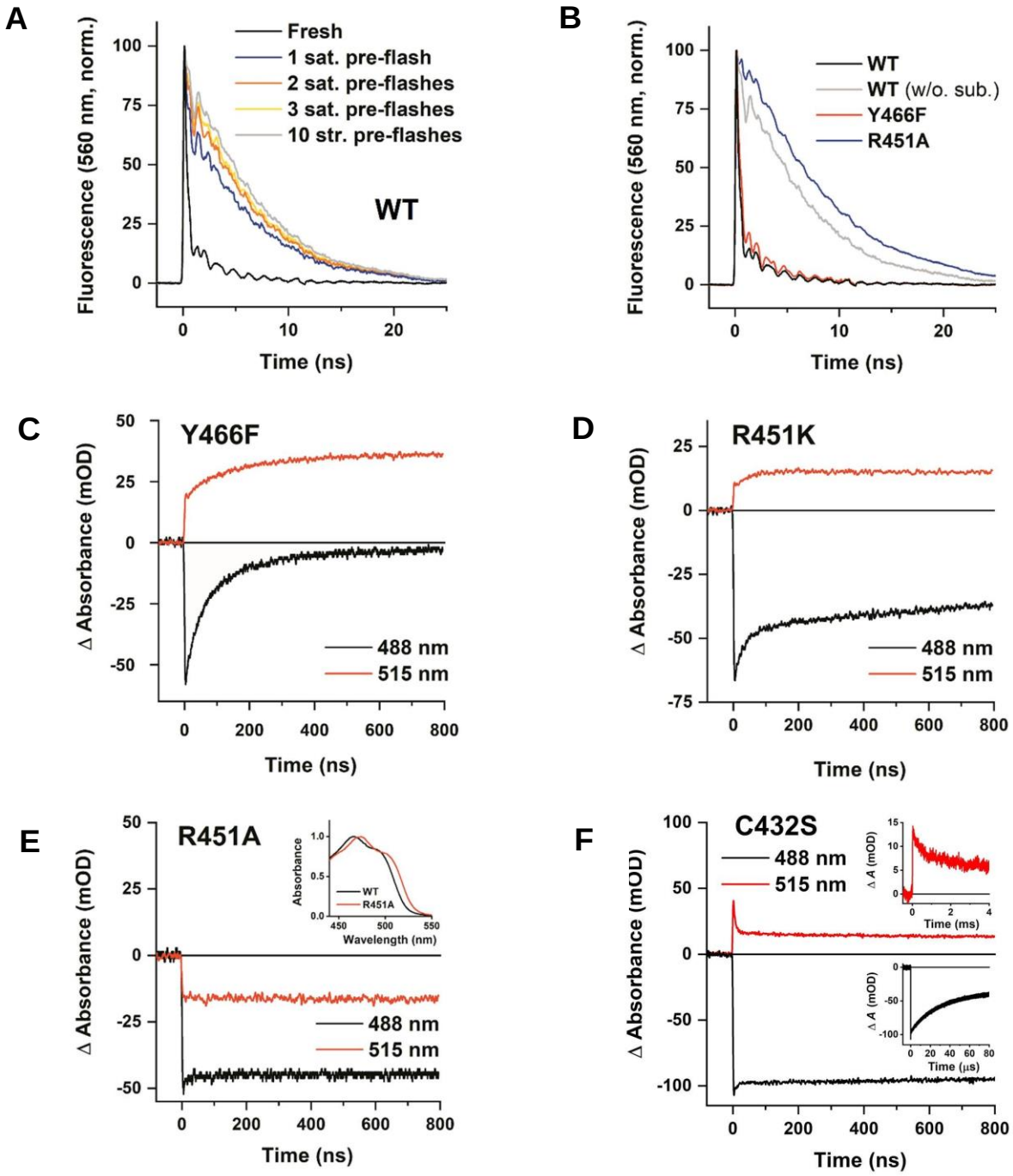

Fig. S25: Time-resolved fluorescence and transient absorption signals of WT and mutant *Cv*FAP.

(**A**) Effect of the native substrate(s) consumption by saturating (~10 mJ) and strong (~5 mJ) pre-flashes at 470 nm on time-resolved ^{1}FAD* fluorescence decay in WT *Cv*FAP at 560 nm

(normalized). (**B**) Comparison of normalized time-resolved ^{1}FAD* fluorescence in ~45 μM WT (before and after consumption of the native substrates) and in ~40 μM Y466F and R451A *Cv*FAP (in the presence of native substrates); for C432S and R451K mutants, see **Fig. 7B**. (**C**) Kinetics of $FAD^{\bullet-}$ reoxidation in ~40 μM Y466F mutant monitored at 488 nm and 515 nm. (**D**) Kinetics of $FAD^{\bullet-}$ reoxidation in ~40 μM R451K mutant. (**E**) Transient absorption changes recorded on the sub-microsecond timescale for ~40 μM R451A *Cv*FAP. Inset: comparison of FAD absorption spectra in WT and R451A *Cv*FAP. (**F**) Transient absorption changes recorded on the sub-microsecond timescale for ~70 μM C432S *Cv*FAP. Lower inset: decay of the signal at 488 nm on the microsecond timescale. Upper iInset: decay of the signal at 515 nm on the millisecond timescale.

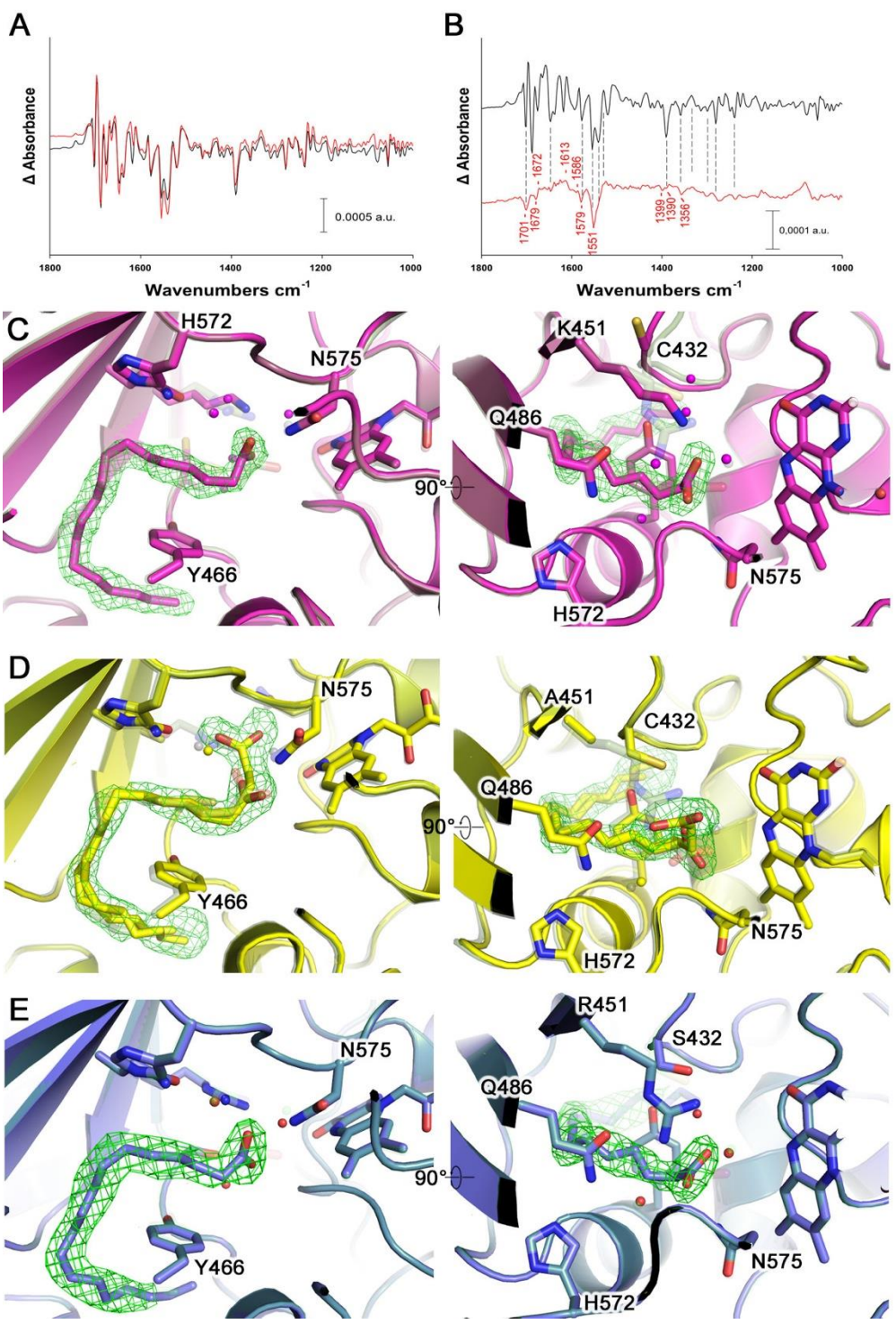
A
Δ Absorbance
0.0005 a.u.
1800
1600
1400
1200
1000
Wavenumbers cm-1
B
Δ Absorbance
1701
1679
1672
1613
1596
1579
1551
1399
1390
1356
0,0001 a.u.
1800
1600
1400
1200
1000
Wavenumbers cm-1
C
H572
N575
90°
Y466
K451
C432
Q486
N575
H572
D
N575
90°
Y466
A451
C432
Q486
N575
H572
E
N575
90°
Y466
R451
S432
Q486
N575
H572

Fig. S26: Comparison of the light-induced FTIR difference spectra of *Cv*FAP and *Cv*FAP mutants recorded at 100 K, and omit map electron density maps of R451K, R451A and C432S mutants.

(**A**) FTIR spectra of *Cv*FAP WT (black) and Y466F mutant (red). (**B**) FTIR spectra of *Cv*FAP and R451K mutant (red). The size of the *Cv*FAP spectrum was divided by a factor of ~6 for the comparison. (**C**) Structure of the R451K mutant (purple) superimposed with the structure of WT (dark and semi-transparent). Note the rotation of the carboxylate compared to the WT. (**D**) Structure of the R451A mutant (yellow) superimposed with the structure of WT (dark and semi-transparent). Note the deeper penetration of the fatty acid substrate in the space left by the missing side chain or R451 and the impossibility to stabilise Wat1. (**E**) Structure of the C432S mutant (blue) superimposed with the structure of WT (dark and semi-transparent). The $F_o - F_c$ omit map (contoured at 3 σ level) corresponding to the fatty acid substrate is shown in green for panels C-E.

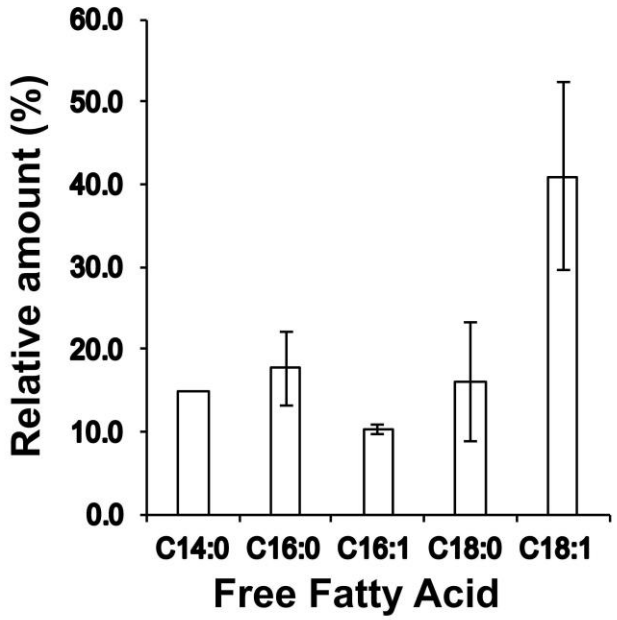

Fig. S27: Analysis of the fatty acids associated with purified WT *Cv*FAP.

Fatty acids co-purified with WT *Cv*FAP were extracted and the composition was analyzed by LC-MS. Mean ± SD (n=3).

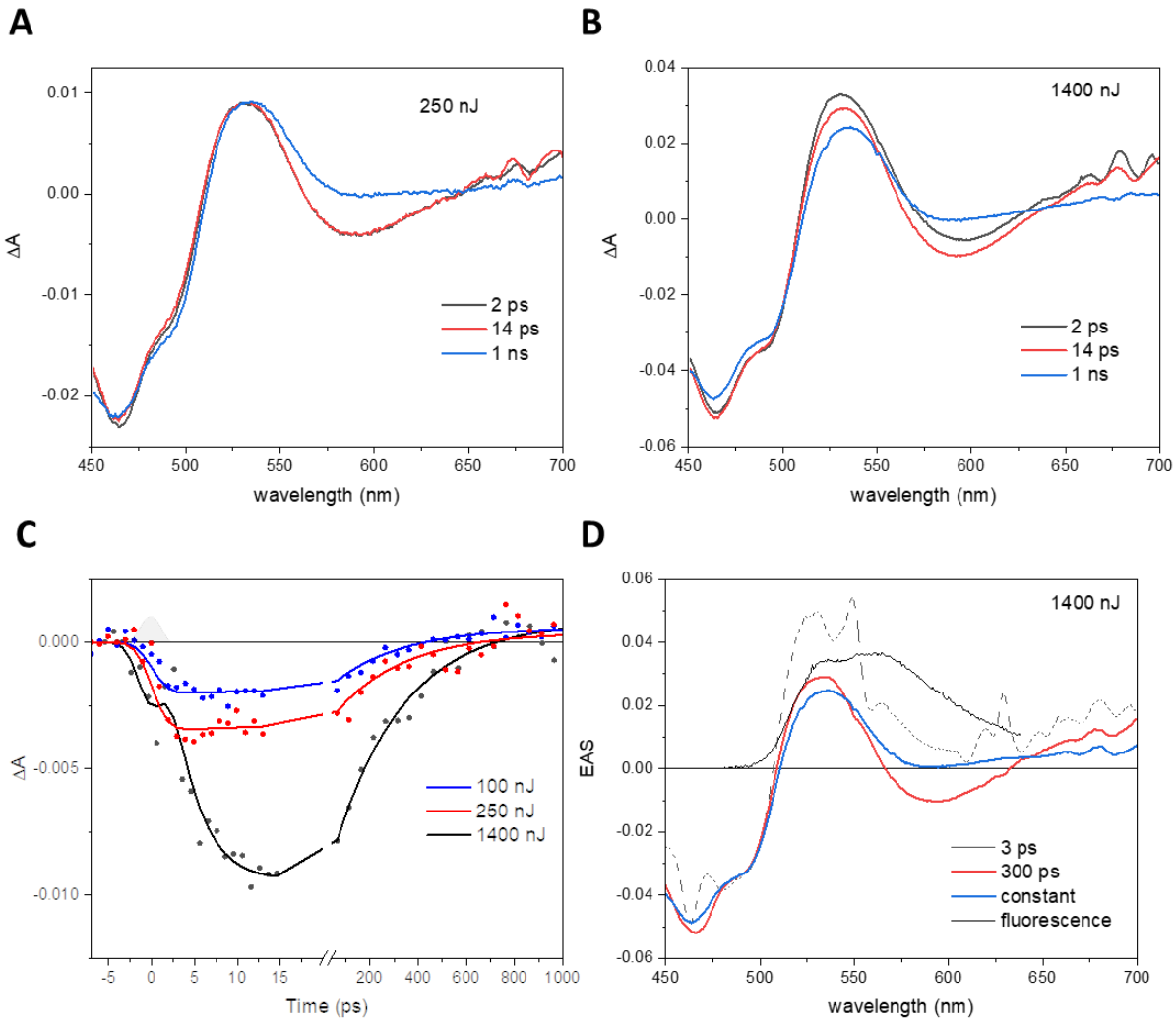

Fig. S28: Excitation power dependence of transient absorption with picosecond excitation pulses.

To investigate possible multiphoton effects under the conditions of the SFX experiments, transient absorption experiments were performed with 2.7-ps pulses (temporal profile in grey in panel C) with energies in the range 100-1400 nJ; the highest energy corresponds to average power density of ~10 GW/cm^2 and absorption of ~2.3 photons/flavin in the excitation volume. The overall shape of the transient spectra is very similar for 100 and 250 nJ, but only at higher

powers in the range 520-620 nm decay of a more positive signal between 2 ps and 14 ps is observed (**A**-**B**). Consistently, whereas the global analysis of the data in terms of a multiexponential model required only a 300-ps and a constant phase at low energy (as with the low-energy 100-fs excitation pulses, fig. S6D), a ~3 ps additional phase was required for high energy (panel **C**-**D**; the strong wiggles around 470, 550 and 630 nm in the 3-ps EAS correspond to cross-phase modulation artifacts that are difficult to eliminate from the fit given that the pulse width is similar to the 3-ps rise time). The spectral evolution associated with this phase (difference between 3-ps and 300-ps EAS) has a similar shape as the FAP fluorescence spectrum (black line) suggesting it represents a rise in the stimulated emission. Altogether it appears that under multiphoton excitation there is a ~3 ps rise component of the S1→S0 emission, whereas it occurs instantaneously at sub-stoichiometric excitation. We assign this to excitation to higher electronic levels by absorption of multiple photons, and subsequent internal conversion to and cooling in the S1 level. These processes occur on a much shorter timescale than the ~300 ps ET time that appears not sensitive to the excitation power. The small differences in shape of the 1-ns spectra (long-lived component) at 1400 nJ and 250 nJ can be assigned to a fraction of long-lived FAD* due to substrate depletion at very high excitation power. No evidence was found for further flavin photoproducts.

Fig. S29: Filtering effect on FAP microcrystal size.

Before filtering, the crystal size was about 100 – 200 × 2 – 5 × 2 – 5 μm^3 (left). After flowing them through a 20 µm (middle) and then a 10 µm filter the size was 10 × 2 – 5 × 2 – 5 μm^3 (right). The scale bar corresponds to 40 µm.

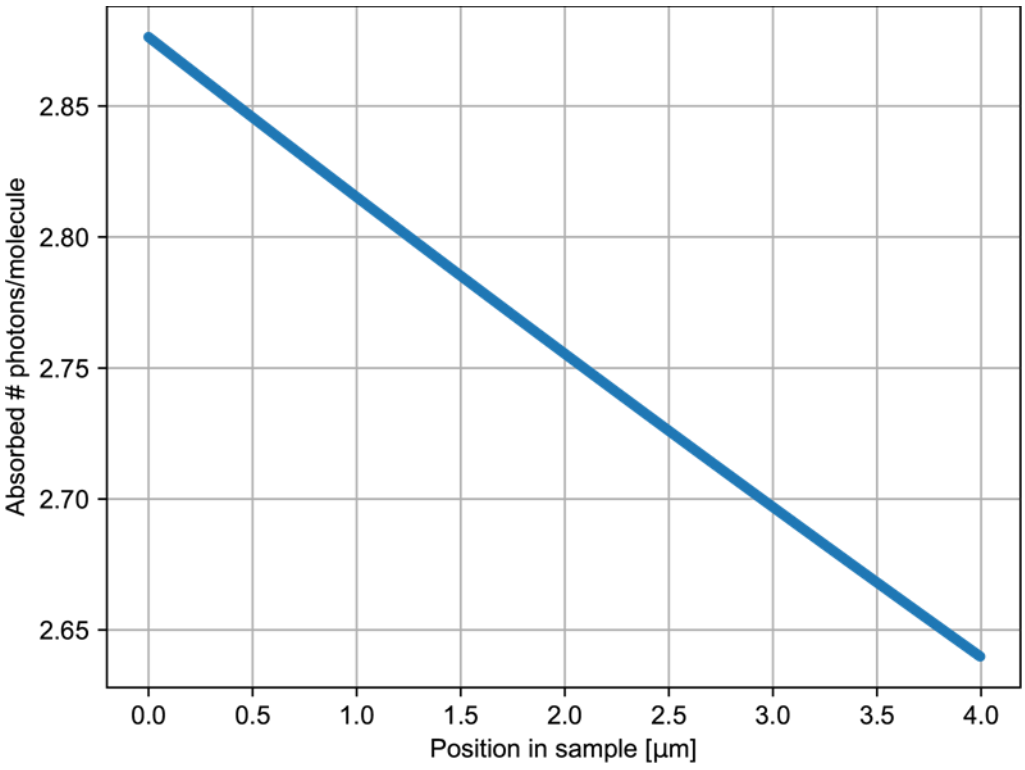

Fig. S30: Depth-dependent photon absorption regimes inside FAP crystals

Depth-dependent photon absorption (9250 $M^{-1}cm^{-1}$ at 400 nm) regime in a 4-µm FAP crystal (FAD concentration 10.3 mM) with pump-laser illumination (4 ps pulse length, 11 µJ pulse energy, 155 µm (FWHM) spot size). The 1/e penetration depth is 47 µm.

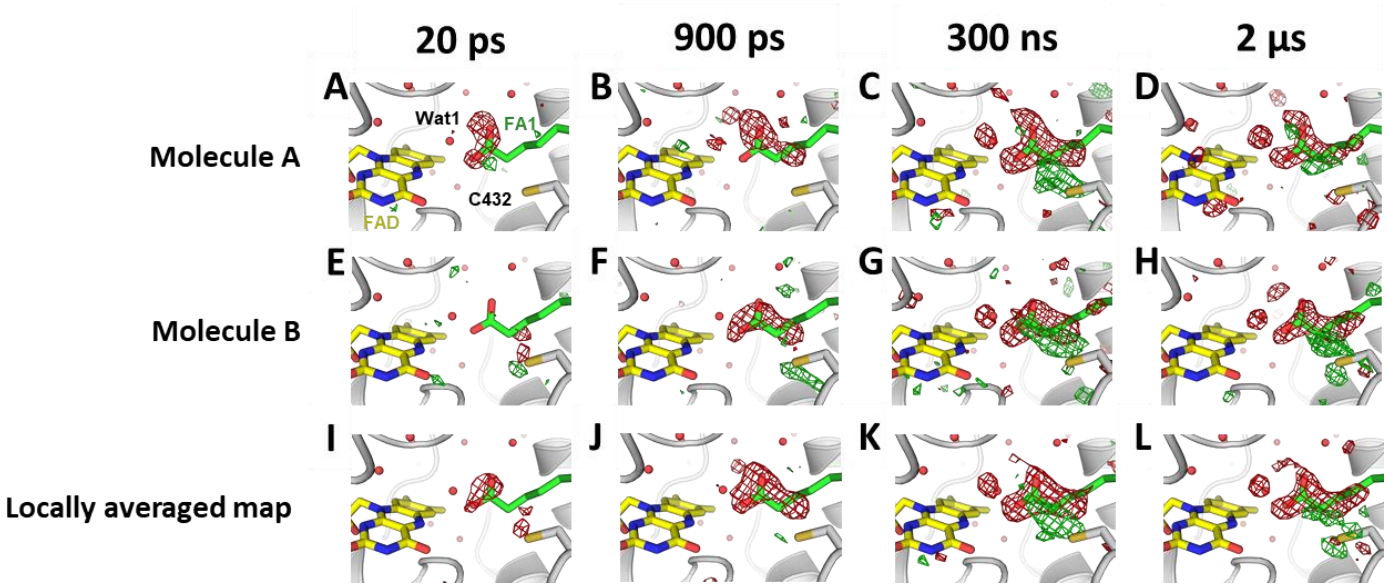

Fig. S31: Time-dependent changes in the *Cv*FAP active site by TR-SFX

Q-weighted difference Fourier electron density maps calculated between the SFX light and dark data sets ($F_{obs}^{\Delta t} - F_{obs}^{dark}$; with Δt = 20 ps (*A, E, I*), 900 ps (*B, F, J*), 300 ns (***C, G, K***), 2 µs (***D, H, L***)) at 2.2 Å resolution. Maps corresponding to molecules A (***A-D***) and B (***E-H***) are shown at +3.5 σ (green) and -3.5 σ (red) and locally NCS-averaged maps (*I-L*) at +4 σ (green) and -4 σ (red). The SFX dark-state model (FAD in yellow, fatty acid in green , protein moiety in light grey) of molecule A is overlaid in panels *A-D* and of molecule B in panels *E-L*. The maps were calculated from 68,421 dark images and 88,919, 50,214, 44,868 and 18,600 light images for Δt = 20 ps, 900 ps and 300 ns and 2 µs, respectively. Panels *I-L* are identical to those in **Fig. 5**.

Supplementary Tables

Table S1. Crystal data, data-collection and refinement statistics.

Data collection							
Data Set Name PDB code	Dark 6YRU	Red-shift 6YRV	Low-Dose 6YRX	pH8.5 6YRZ	R451K 6YS1	R451A 6YS2	
Beamline	ID29/ESRF	ID29/ESRF	ID30-A3/ESRF	PX1/SOLEIL	ID29/ESRF	ID29/ESRF	;
Dark/Light	Dark	Light	Dark	Light	Dark	Dark	
pH	5.5	5.5	5.5	8.5	5.5	5.5	
Temperature	100 K	100 K	RT	150 K	100 K	100 K	
Space Group	*I*222	*I*222	*I*222	*I*222	$P2_12_12_1$	*I*222	
Unit-cell parameters (Å)							
a	89.7	89.9	95.6	90.5	58.9	89.6	
b	103.6	103.7	105.7	104.6	60.8	102.8	
c	155.9	156.3	158.0	156.9	180.1	155.8	
Resolution range (Å)	86 – 1.78	86 – 1.94	88 – 1.87	87 – 1.82	90 – 1.97	86 – 1.64	.
High resolution range (Å)	1.9 – 1.78	2 – 1.94	2 – 1.87	1.93 – 1.82	2.1 – 1.97	1.75 – 1.64	ł
Observed reflections	327,307	359,526	278,791	895,789	225,269	370,900	
No. of unique reflections	69,240	54,600	65,032	66,267	46,463	87,644	
Completeness (%)	99.3 (99.4)	100 (100)	98.1 (99.7)	99.7 (98.2)	99.5 (99)	99.5 (99.5)	1)
Multiplicity							
CC1/2	99.8 (51.2)	99.8 (72.4)	99.6 (43.6)	99.9 (81.6)	99.6 (56.8)	99.8 (53.7)	0)
$\langle I/\sigma(I)\rangle$	11 (1)	11.7 (2.2)	7.6 (1)	18.4 (2.1)	8.8 (1.4)	12.2 (1.5)	)
R_{meas}(%)[#]	9.6 (127)	11.6 (84.9)	10.9 (106.4)	8.9 (107.8)	15 (113.1)	8.3 (98.4)	3)
Refinement							
Resolution range (Å)	46.5 – 1.78	86.5 – 1.94	87.8 – 1.87	87 – 1.82	86 – 1.97	90 – 1.97	
R_{work}/ R_{free}	17.2 / 20.2	16.5 / 20.4	15.1 / 18.0	15.5 / 18.6	16.5 / 19.4	17.9 / 23.0	1
No. of non-H atoms:							
Protein	4,267	4,267	4,257	4,292	4,302	4,192	
FAD	53	53	53	53	53	53	
FA1[‡]	20	-	20	20	20	20 (0.8) / 20 (0.2)	
FA2	20	20	20	20	20	20	
HDE*	-	17	-	17	-		

CO_2‡	-	3	-	3	-	-
Bicarbonate				4		
B-Factors						
Protein	31.7	30.9	36.3	35.8	24.2	35.1
FAD	23.9	22.7	25.4	26.9	18.0	28.4
FA1‡	30.5	-	34.9		30.2	18.7
FA2	45.8	44.7	61.2	52.8	45.3	45.3
HDE‡	-	32	-	39.2	-	-
CO_2‡	-	52	-	59.3	-	-
Ramachandran outliers (%)	1.1	0.9	0.4	0.2	0.2	0.4
R.m.s. deviation from ideal geometry						
Bond lengths (Å)	0.019	0.019	0.019	0.012	0.012	0.009
Bond angles (°)	1.97	1.94	1.98	1.72	1.80	1.63

Values in parentheses are for the highest resolution shell. #R_{meas} corresponds to redundancy-independant Rsym.. ‡Number in parentheses corresponds to the refined occupancies. *HDE stands for heptadecane, the modeled product of stearate decarboxylation.

1 **Table S2: SFX data processing and refinement statistics**

Dataset	dark	light_20ps	light_900ps	light_300ns	light_2µs
PDB ID code	6ZH7				
Pump-laser excitation (400 nm)	no	yes	yes	yes	yes
Nominal pump-probe delay	n/a	20 ps	900 ps	300 ns	2 µs
Space group	$P2_1$	$P2_1$	$P2_1$	$P2_1$	$P2_1$
Unit cell parameters a (Å) b (Å) c (Å) β (°)	 61.4± 0.1 60.0 ± 0.1 182.9 ± 0.3 90.6	 61.4 ± 0.1 60.0 ± 0.1 182.9 ± 0.3 90.6	 61.4 ± 0.1 60.0 ± 0.1 182.9 ± 0.3 90.6	 61.4 ± 0.1 60.0 ± 0.1 182.9 ± 0.3 90.6	 61.4 ± 0.1 60.0 ± 0.1 182.9 ± 0.3 90.6
Collected frames	2,579,455	1,625,450	1,728,093	1,298,912	909,645
Hits	264,812	290,962	227,517	151,599	66,358
Indexed images	68,421	88,919	50,214	44,868	18,600
Resolution (Å)	25– 2.00 (2.05 – 2.00)	25– 2.00 (2.05 – 2.00)	25– 2.00 (2.05 –2.00)	25– 2.00 (2.05 – 2.00)	25– 2.20 (2.25 – 2.20)
Observations	33,069,955 (1,438,474)	42,928,992 (1,869,092)	25,083,092 (1,091,803)	20,934,706 (907,081)	8,076,033 (383,644)
Unique reflections	93,061 (6,086)	93,060 (6,086)	93,064 (6,086)	93,055 (6,086)	70,385 (4,671)
R_{split}[#] (%)	15.1 (68.5)	13.4 (61.3)	18.0 (80.0)	19.4 (84.5)	24.9 (67.8)
CC*	0.996 (0.841)	0.996 (0.869)	0.994 (0.797)	0.992 (0.790)	0.983 (0.816)
I / σ(I)	5.6 (1.7)	6.40 (1.9)	4.8 (1.4)	4.4 (1.3)	3.7 (1.6)
Completeness (%)	100 (100)	100 (100)	100 (100)	100 (100)	100 (100)
Multiplicity	355 (236)	461 (307)	270 (179)	225 (149)	115 (82)
R_{iso}[$] (with respect to dark dataset)	n.a	0.157	0.171	0.174	0.202
Refinement statistics					
Refinement strategy	Classical refinement	n.a	n.a	n.a	n.a
Resolution (Å)	25– 2.00 (2.05 – 2.00)				
R_{free}	0.235				
R_{work}	0.196				
Number of protein atoms	8417				
Number of ligand atoms	166				

Number of water atoms	394				
B-factor protein (Å^2)	31				
r.m.s.d. bond lengths (Å)	0.01				
r.m.s.d. angles (°)	1.8				
Ramachandran favored	95.8 %				
Ramachandran allowed	3.7 %				
Ramachadran outliers	0.2 %				
Rotamer outliers	1.6 %				
C-beta outliers	0				
Clashscore	5				

1 Values in brackets are for the highest resolution shell

$$^{\#}:R_{split} = \frac{1}{\sqrt{2}} \times \frac{\sum_{hkl}\left|I_{hkl}^{even} - I_{hkl}^{odd}\right|}{0.5 \times \sum_{hkl}\left|I_{hkl}^{even} + I_{hkl}^{odd}\right|}$$

2

3 CC*: see (*121*)

4 $R_{iso}^{\$}$ was calculated using *Phenix* up to 2.2 Å resolution

5

6

7

Table S3: Primers list

FAP (76-654)	**5'-aacctgtacttccaatcaagtccggttgca-3'**
	5'-tatccacctttactgttatcatgctgcaacggttgccggtg-3'
R451A	**5'-catacccggaacaaaagctacctgcagatccggc-3'**
	5'-gccggatctgcaggtagcttttgttccgggtatg-3'
R451K	**5'-gtgccatacccggaacaaactttacctgcagatccggcagt-3'**
	5'-actgccggatctgcaggtaaagtttgttccgggtatggcac-3'
Y466F	**5'-ttttgcaaaacgaacaaaggtgctaacaccatccgg-3'**
	5'-ccggatggtgttagcacctttgttcgttttgcaaaa-3'

Table S4: list of sequences of FAPs and other GMC oxidoreductases used for protein alignment and sequence logo.

Accession numbers are indicated between parentheses.

Putative FAPs	Glucose methanol choline oxidoreductases (other than FAP)
Aureococcus anophagefferens (F0YAB1)	*Aspergillus niger* (J05242)
Chlamydomonas reinhardtii (XP_001703004)	*Brevibacterium sterolicum* (P22637)
Chlorella variabilis NC64A (KY511411)	*Caenorhabditis elegans* (Q18429)
Chondrus crispus (XP_005714951)	*Candida boidinii* (Q00922)
Chrysochromulina (KOO25289)	*Caulobacter crescentus*(AAK22929)
Coccomyxa subellipsoidea C-169 (XP_005642926)	*Drosophila melanogaster* (NM_058155)
Cyanidioschyzon merolae (XP_005537774)	*Escherichia coli* (NP414845)
Dunaliella salina (Dusal.0308s00018.1)	*Gluconobacter oxydans* (BAA13145)
Ectocarpus siliculosus (CBJ25560)	*Halococcus sediminicola* (WP_049996878)
Fragilariopsis cylindrus CCMP1102 (A0A1E7FBP9)	*Phanerochaete chrysosporium* (U46081)
Galdieria sulphuraria (XP_005706847)	*Phytophthora parasitica* (W2PSU1)
Nannochloropsis gaditana (EWM27492)	*Pleurotus pulmonarius* (AAF31169)
Phaeodactylum tricornutum CCAP 1055/1 (B7FSU6)	*Prunus dulcis* (O24243)
Volvox carteri f. nagariensis (XP_002948047)	*Pseudomonas fluorescens* (ZP_00084192)
	Pseudomonas oleovorans (Q00593)
	Sphingopyxis terrae (BAB61732)

Table S5: R-/U-B3LYP energies and energy gradient of the optimized geometries modelling alkane production by the FAP enzyme.

The active site model is presented in fig. S16. CS and DR(CT) stands for closed-shell and diradical (charge-transfer).

Geometry and electronic configuration	dark state/ intermediate/ product	Energy, au (energy relative to (1), kcal/mol)	Max energy grad, au	RMS energy grad, au
(1) CS	dark state	-6524.996965 (0.0)	0.0002	0.0001
(2) CS	Unstable structure with rearranged Wat1	-6524.962562 (21.6)	0.006	0.0007
(3) DR(CT)	Intermediate $FAD^{\bullet-}$- and alkyl radicals, CO_2	-6524.914696 (51.6)	0.0003	0.0001
(4) DR(CT)	Intermediate $FAD^{\bullet-}$- and C432 radicals, CO_2	-6524.938438 (36.7)	0.0003	0.0001
(5) CS	Intermediate; alkane, C432 anion, CO_2	-6524.943038 (33.8)	0.0003	0.0001
(5a) CS	Intermediate; alkane neutral R541, CO_2	-6524.942524 (34.2)	0.0005	0.0001
(5b) CS	Intermediate; alkane deprot R451, CO_2	-6524.953052 (27.6)	0.0003	0.0001
(6) CS	Product state; bicarbonate derived from Wat1	-6524.986142 (6.8)	0.0004	0.0001
(6a) CS	Product state; bicarbonate derived from Wat2	-6524.968644 (17.1)	0.0011	0.0001

Table S6: Excitation energy calculations for geometries (1) and (2).

Excitation energy, eV/ transition dipole moment, au/ state assignment are indicated for each state. The details of the XMCQDPT2-CASSCF calculations are given for each geometry.

State	(1) sa8(14,8)	(1)-wo-Wat2 sa10(18,10)	(2) sa8(14,8)
1	2.36/ 0.515/ Fl nπ*[a)]	2.36/ 0.578/ Fl nπ*	1.87/ 0.438/ CT FA
2	2.70/ 2.302/ Fl ππ*[b)]	2.71/ 2.294/ Fl ππ*	2.33/ 0.316/ Fl nπ*
3	3.41/ 0.373/ CT A171-T172 [c)]	2.81/ 0.279/ CT FA [c)]	2.54/ 2.244/ Fl ππ*
4	3.54/ 1.889/ Fl ππ*[b)]	3.48/ 0.908/ CT A171-T172	3.01/ 0.472/ CT FA
5	4.01/ 0.004/ CT Y466 [c)]	3.53/ 1.149/ CT FA [c)]	3.25/ 2.136/ Fl ππ*
6	4.64/ 0.143/ CT C432 [c)]	3.60/ 1.212 / Fl ππ*	3.37/ 0.010/ CT Y466
7	5.12/ 0.004/ CT Y466 [c)]	4.14/ 0.001/ CT Y466	4.46/ 0.002/ CT Y466
8		4.83/ 0.014/ CT C432	
9		5.25/ 0.007/ CT Y466	

a) nπ* state of flavin involving the lone pair of N5 with a low osc. strength;

b) ππ* state flavin with a high osc. strength corresponding to an absorption band;

c) ππ* charge-transfer (CT) state from the protein (involved residues indicated) and fatty acid (FA) to flavin with a low oscillator strength.

Table S7: Electronic couplings for states involved in fET and bET.

For a pair of states i and j, we indicate the energy gap (ΔE_{ij}), transition dipole moment (tdm_{ij}), and dipole moment change (Δd_{ij}). These quantities determine the electronic coupling (V_{ij}) The geometry for which excited states were computed, details of the XMCQDPT2-CASSCF calculations and shortest distance between the donor and acceptor (DA distance) are given. fET and bET stand for forward and back electron transfer, respectively.

Transition between states i and j	ΔE_{ij}, au	tdm_{ij}, au	Δd_{ij}, au	V_{ij}, meV
Coupling between flavin and protein (A171-T172)				
Geometry (1); sa, distance 2.00 Å				
states 3 and 4	0.020848	0.616	8.5	40
C432S geometry ($1^{C/S}$)-wo-W3; sa8(14,8); DA distance 2.07 Å				
states 3 and 5	0.027289	0.264	8.7	22
Couplings for fET				
Geometry (1)-wo-Wat2; sa10(18,10); DA distance 3.06 Å				
states 2 and 3	0.003863	1.385	8.3	17
Geometry (2); sa8(14,8); DA distance 2.81 Å				
states 1 and 3	0.024880	0.599	8.5	47
C432S geometry ($1^{C/S}$)-wo-Wat2; sa8(14,8); DA distance 4.77 Å				
states 2 and 3	0.009329	0.599	11.4	13
C432S geometry ($2^{C/S}$); sa7(12,12); DA distance 4.84 Å				
states 3and 4	0.004058	0.799	11.4	8
alkyl and Y466 coupling				
Geometry (3), sa5(8,5); DA distance 3.69 Å				
states 1 and 5	0.166660	0.223	7.1	142
Couplings for bET				
Geometry (3), sa5(8,5); distance 6.57 Å				
states 0 and 3	0.115436	0.029	14.8	6
Geometry (4); sa7(12,7); distance 6.93 Å				
states 0 and 2	0.030510	0.053408	15.7	3
states 1and 2	0.023301	0.088748	15.7	4

Table S8: Excitation energy calculations for suggested oxidized flavin red-shifted intermediates (5), (5b), (6) and (6a).

Excitation energy, eV/ transition dipole moment, au/ state assignment are indicated for each state. The XMCQDPT2-CASSCF sa7(12,7) calculations for all geometries except (5).

States	(1)	(5); sa8(14,8)	(5b)	(6)	(6a)
1	2.31/ 0.590/ Fl nπ*	0.91/0.054/CT C432	2.23/ 0.436/ Fl nπ*	2.30/ 0.516/ Fl nπ*	2.29/ 0.617/ Fl nπ*
2	2.70/ 2.253/ Fl ππ*	1.21/0.107/CT C432	2.56/ 2.275/ Fl ππ*	2.64/ 2.260/ Fl ππ*	2.65/ 2.250/ Fl ππ*
3	3.57/ 1.959/ Fl ππ*	2.62/2.377/Fl ππ*	2.63/ 0.012/ CT R541	3.47/ 2.011/ Fl ππ*	3.53/ 1.980/ Fl ππ*
4	4.11/ 0.004/ CT Y466	3.08/0.001/CT Y466	3.33/ 0.000/ CT Y466	3.90/ 0.001/ CT Y466	4.07/ 0.001/ CT Y466
5	4.64/ 0.143/ CT C432	3.24/0.003/CT C432	3.47/ 2.003/ Fl ππ*	4.64/ 0.008/ CT C432	4.67/ 0.006/ CT C432
6	5.12/ 0.004/ CT Y466	3.66/1.877/ Fl ππ*	3.82/ 0.004/ CT C432	5.01/ 0.002/ CT Y466	5.19/ 0.008/ CT Y466
7		4.26/0.016/CT C432			

Table S9: Effect of butterfly bending on flavin redox and excitation energies.

At the indicated geometries, energies of the flavin oxidized and radical-anion states were computed. The oxidized flavin was also computed in the excited state (energies given in brackets). In addition to isoalloxazine, a FAP active site model (AS) was considered (the model is presented in **fig. S16**). To facilitate comparison, relative energies were computed. To discuss the effect of flavin bending (see fig. S21), we compare electron affinities (VEA[a)] and AEA[b)]) and excitation energies (VE[c)]). The negative EAs indicate that oxidized flavin is higher in energy than radical anion.

Geometry	Energy, au		Relative energy, eV	
	oxidized	rad. anion	oxidized	rad. anion
Planar oxidized	-986.177790 (-986.066712)	-986.219889	0.0 VE: 3.02	VEA: -1.15
Planar rad-an	-986.170156	-986.235240	0.21	AEA[e)]: -1.57
Oxidized, 20 deg [d)]	-986.170943 (-986.064903)	-986.220929	0.0 VE: 2.89	VEA: -1.36
Rad-an, 20 deg	-986.162278	-986.230043	0.24	AEA: -1.61
Oxidized, 30 deg	-986.159248 (-986.056440)	-986.207741	0.0 VE: 2.80	VEA: -1.32
Rad-an, 30 deg	-986.151201	-986.222770	0.22	AEA: -1.73
Oxidized in AS, 15 deg [e)]	-4378.641248 (-4378.541981)	-4378.788512	0.0 VE: 2.70	VEA: -4.00
Radical anion in AS, 20 deg [f)]	-4378.645995	-4378.841320	-0.13	AEA: -5.44

a) Vertical electron affinity (VEA), the energy change due to adding one electron to the oxidized flavin at the oxidized-flavin optimized geometry;

b) adiabatic electron affinity (AEA), the energy change due to adding one electron to the oxidized flavin taking into account geometry relaxation;

c) vertical excitation (VE), the energy of the first flavin ππ* computed with TD-B3LYP at the oxidized-flavin optimized geometry;

d) the constraint butterfly bending angle;

e) the butterfly bending angle after geometry optimization of the dark state (1);

f) the butterfly bending angle after geometry optimization of the radical intermediate (3).

Table S10: Excitation energy calculations for C432S model: effect of Wat3.

Excitation energy, eV/ transition dipole moment, au/ state assignment are indicated for each state. Details of the XMCQDPT2-CASSCF calculations are given for each model.

Exc. state	($1^{C/S}$) sa6(10,6)	($1^{C/S}$)-wo-Wat2; sa8(14,8)	($1^{C/S}$)-wo-Wat3 sa8(14,8)	($2^{C/S}$) sa7(12,7)
1	2.28/0.528/Fl nπ*	2.24/0.516/Fl nπ*	2.28/0.530/ Fl nπ*	2.27/0.644/ Fl nπ*
2	2.71/2.234/Fl ππ*	2.73/2.360/Fl ππ*	2.71/2.347/ Fl ππ*	2.55/0.212/CT FA [d)]
3	3.71/1.915/Fl ππ*	2.99/0.124/CT FA [a),b)]	2.98/0.181/CT FA [b)]	2.66/2.303/Fl ππ*
4	4.02/0.001/CT Y466	3.74/1.853/Fl ππ*	3.45/0.201/CT A171-T172 [c)]	3.55/0.014/CT Y466
5	5.16/0.009/CT Y466	3.89/0.207/CT FA	3.72/1.858/ Fl ππ*	3.56/0.197/CT FA
6		4.18/0.001/CT Y466	4.05/0.001/CT Y466	3.66/1.937/ Fl ππ*
7		5.32/0.003 CT Y466	5.16/0.004/CT Y466	

a) this energy in comparison to a similar energy of the dark state (1)-wo-Wat2 (2.81 eVm Table S6) indicates an increase of the CT-fatty acid (FA) energy by interactions of the substrate with Wat3;

b) removing of Wat3 and Wat2 both reduce the energy of electron abstraction by flavin from the fatty acid carboxylate to the same energy level, about 3 eV above the ground-state energy;

c) removing Wat3 reduces the energy of electron transfer from A171-T172 donor to the flavin. This energy is comparable to the respective energy in the WT active site model (1)

d) In the wt model (2), the CT-fatty acid energy is 1.87 eV (table S6). Hence, interactions with Wat 3 stabilise the fatty acid COO- group also after Wat1 rearrangement, yet the CT-fatty acid energy is lower than the flavin $\pi\pi^*$ energy.

Table S11: Excitation energy calculations for diradical intermediates (3) and (4).

Excitation energy, eV/ transition dipole moment, au/ state assignment are indicated for each state. The details of the XMCQDPT2-CASSCF calculations are given for each geometry.

Ext. state	(3) sa5(8,5)	(4) sa7(12,7)
1	2.44/ 1.886/ Fl rad-an	0.20/ 0.025/ C432 rad
2	2.97/ 2.220/ Fl rad-an	0.83/ 0.053/bET
3	3.14/ 0.029/ bET	2.67/ 2.184/Fl rad-an
4	4.64/ 0.131/ CT Y466	2.87/ 0.131/Fl&C432
5		3.21/1.945/Fl rad-an
6		3.41/0.004/Fl&C432